THE UNIVERSITY OF SHEFFIELD

A Probabilistic Framework for Statistical Shape Models and Atlas Construction: Application to Neuroimaging

Author:
Nishant Ravikumar
Main supervisor:
Dr. Zeike A. Taylor
Co-supervisor:
Prof. Alejandro F. Frangi

A thesis submitted in fulfilment of the requirements for the degree of Doctor of Philosophy in the

Department of Mechanical Engineering
The University of Sheffield

September 28, 2017

Declaration of Authorship

I, Nishant Ravikumar, declare that this thesis titled, "A Probabilistic Framework for Statistical Shape Models and Atlas Construction: Application to Neuroimaging" and the work presented in it are my own. I confirm that:

- This work was done wholly or mainly while in candidature for a research degree at this University.
- Where any part of this thesis has previously been submitted for a degree or any other qualification at this University or any other institution, this has been clearly stated.
- Where I have consulted the published work of others, this is always clearly attributed.
- Where I have quoted from the work of others, the source is always given. With the exception of such quotations, this thesis is entirely my own work.
- I have acknowledged all main sources of help.
- Where the thesis is based on work done by myself jointly with others, I have made clear exactly what was done by others and what I have contributed myself.

Signed: 

Date: September 28, 2017

Abstract

Accurate and reliable registration of shapes and multi-dimensional point sets describing the morphology/physiology of anatomical structures is a pre-requisite for constructing statistical shape models (SSMs) and atlases. Such statistical descriptions of variability across populations (regarding shape or other morphological/physiological quantities) are based on homologous correspondences across the multiple samples that comprise the training data. The notion of exact correspondence can be ambiguous when these data contain noise and outliers, missing data, or significant and abnormal variations due to pathology. But, these phenomena are common in medical image-derived data, due, for example, to inconsistencies in image quality and acquisition protocols, presence of motion artefacts, differences in pre-processing steps, and inherent variability across patient populations and demographics. This thesis therefore focuses on formulating a unified probabilistic framework for the registration of shapes and so-called *generalised point sets*, which is robust to the anomalies and variations described.

Statistical analysis of shapes across large cohorts demands automatic generation of training sets (image segmentations delineating the structure of interest), as manual and semi-supervised approaches can be prohibitively time consuming. However, automated segmentation and landmarking of images often result in shapes with high levels of outliers and missing data. Consequently, a robust method for registration and correspondence estimation is required. A probabilistic group-wise registration framework for point-based representations of shapes, based on Student's t-mixture model (TMM) and a multi-resolution extension to the same (mrTMM), are formulated to this end. The frameworks exploit the inherent robustness of Student's t-distributions to outliers, which is lacking in existing Gaussian mixture model (GMM)-based approaches. The registration accuracy of the proposed approaches was quantitatively evaluated and shown to outperform the state-of-the-art, using synthetic and clinical data. A corresponding improvement in the quality of SSMs generated subsequently was also shown, particularly for data sets containing high levels of noise. In general, the proposed approach requires fewer user specified parameters than existing methods, whilst affording much improved robustness to outliers.

Registration of generalised point sets, which combine disparate features such as spatial positions, directional/axial data, and scalar-valued quantities, was studied next. A hybrid mixture model (HMM), combining different types of probability distributions, was formulated to facilitate the joint registration and

clustering of multi-dimensional point sets of this nature. Two variants of the HMM were developed for modelling: (1) axial data; and (2) directional data. The former, based on a combination of Student's t, Watson and Gaussian distributions, was used to register hybrid point sets comprising magnetic resonance diffusion tensor image (DTI)-derived quantities, such as voxel spatial positions (defining a region/structure of interest), associated fibre orientations, and scalar measures reflecting tissue anisotropy. The latter meanwhile, formulated using a combination of Student's t and Von-Mises-Fisher distributions, is used for the registration of shapes represented as hybrid point sets comprising spatial positions and associated surface normal vectors. The Watson-variant of the HMM facilitates statistical analysis and group-wise comparisons of DTI data across patient populations, presented as an exemplar application of the proposed approach. The Fisher-variant of the HMM on the other hand, was used to register hybrid representations of shapes, providing substantial improvements over point-based registration approaches in terms of anatomical validity in the estimated correspondences.

Acknowledgements

The work presented in this thesis would not have been possible without the support and guidance of a number of people, to whom I am greatly indebted.

To begin with, I would like to thank my supervisor Dr. Zeike Taylor, for providing me with this opportunity, and guiding me through these deep waters. His patience, and trust in my abilities gave me confidence and helped me develop independence as a researcher. I am very grateful for his constructive advice, which has always helped improve the quality of my work, and, for sharing his experience and knowledge, to help me overcome obstacles along the way. I would like to thank my co-supervisor Prof. Alejandro Frangi for providing me with an excellent work environment and opportunities to collaborate with numerous researchers within the community. His guidance and advice helped me appreciate the broader perspectives of research. My deep gratitude also goes to Dr. Ali Gooya, for introducing me to the fascinating world of machine learning, providing me with inspiration when needed, and for the many hours spent together, conceiving the work presented herein.

Working at CISTIB was a pleasure and privilege, and my deepest thanks go to all my colleagues, for their enduring support these past few years. I thank the software development team at CISTIB for their conscientious approach in assisting me with various aspects of software development, and helping me hone my skills as a programmer. Special thanks go to Christopher Noble, Edward Cramphorn, Matthias Lange and Serkan Çimen, whose friendship made the past few years all the more enjoyable, and for the numerous engaging conversations, which were welcome distractions from academic matters.

Finally I would like to thank my family, for always being my home, and for their unwavering faith in me, which gave me the strength and stability needed to pursue my dreams.

This work was partially supported by the European Unions Seventh Framework Programme (FP7/2007 2013) as part of the project VPH-DARE@IT (grant agreement no. 601055) and by the Department of Mechanical Engineering, University of Sheffield.

List of Publications

The work presented in this thesis was partially adapted from publications [1], [3], [4], [5] and [6] listed below, with all permissions acquired.

1. Ravikumar, N., Castro-Mateos, I., Pozo, J.M., Frangi, A.F. and Taylor, Z.A., 2015, March. 3D active shape models of human brain structures: application to patient-specific mesh generation. In SPIE Medical Imaging (pp. 94142D-94142D). International Society for Optics and Photonics.

2. Ravikumar, N., Noble, C., Cramphorn, E. and Taylor, Z.A., 2015. A constitutive model for ballistic gelatin at surgical strain rates. Journal of the mechanical behavior of biomedical materials, 47, pp.87-94.

3. Ravikumar, N., Gooya, A., Frangi, A.F. and Taylor, Z.A., 2016, March. Robust group-wise rigid registration of point sets using t-mixture model. In SPIE Medical Imaging (pp. 97840S-97840S). International Society for Optics and Photonics.

4. Ravikumar, N., Gooya, A., Çimen, S., Frangi, A.F. and Taylor, Z.A., 2016, October. A multi-resolution t-mixture model approach to robust group-wise alignment of shapes. In International Conference on Medical Image Computing and Computer-Assisted Intervention (pp. 142-149). Springer International Publishing.

5. Ravikumar, N., Gooya, A., Frangi, A.F. and Taylor, Z.A., 2017, September. Generalised coherent point drift for group-wise registration of multi-dimensional point sets. In International Conference on Medical Image Computing and Computer-Assisted Intervention (In press). Springer International Publishing.

6. Ravikumar, N., Gooya, A., Frangi, A.F. and Taylor, Z.A., 2017, Group-wise registration of point sets using Student's t-mixture model for statistical shape models. Medical Image Analysis (Under review).

7. Ravikumar, N., Gooya, A., Beltrachini, L., Frangi, A.F. and Taylor, Z.A., 2017, Generalised coherent point drift for group-wise multi-dimensional analysis of diffusion brain MRI data. Medical Image Analysis (Under review).

8. McGrath, D.M., Ravikumar, N., Wilkinson, I.D., Frangi, A.F. and Taylor, Z.A., 2015. Magnetic resonance elastography of the brain: An in silico study to determine the influence of cranial anatomy. Magnetic resonance in medicine.

9. McGrath, D.M., Ravikumar, N., Beltrachini, L., Wilkinson, I.D., Frangi, A.F. and Taylor, Z.A., 2016. Evaluation of wave delivery methodology for brain MRE: Insights from computational simulations. Magnetic Resonance in Medicine.

10. Çimen, S., Gooya, A., Ravikumar, N., Taylor, Z.A. and Frangi, A.F., 2016, October. Reconstruction of Coronary Artery Centrelines from X-Ray Angiography Using a Mixture of Student's t-Distributions. In International Conference on Medical Image Computing and Computer-Assisted Intervention (pp. 291-299). Springer International Publishing.

Contents

List of Figures

List of Tables

List of Abbreviations

AD	Alzheimer's Disease
MCI	Mild Cognitive Impairment
HC	Healthy Control
CSF	Cerebro-spinal Fluid
WM	White Matter
GM	Grey Matter
MRI	Magnetic Resonance Imaging
DTI	Diffusion Tensor Imaging
SSM	Statistical Shape Model
PCA	Principal Component Analysis
PDM	Point Distribution Model
GMM	Gaussian Mixture Model
TMM	Student's t-Mixture Model
mrTMM	Multi-Resolution Student's t-Mixture Model
FA	Fractional Anisotropy
ICP	Iterative Closest Point
CPD	Coherent Point Drift
gCPD	Group-wise Coherent Point Drift
EM	Expectation-Maximisation
SpSSM	Sparse Statistical Shape Model
JRMPC	Joint Registration of Multiple Point Clouds
ML	Maximum Likelihood
TMM-NR	Student's t-Mixture Model Non-Rigid
HD	Hausdorff Distance
MSD	Mean Surface Distance
PH	Pulmonary Hypertension
HCM	Hypertrophic Cardiomyopathy
HMM	Hybrid Mixture Model
ROI	Region of Interest
TBSS	Tract-based Spatial Statistics
VBM	Voxel-based Morphometry

PDF	Probability Density Function
WMM	Watson Mixture Model
FMM	Von-Mises-Fisher Mixture Model
RMSE	Root Mean Squared Error
RSE	Root Squared Error
IQR	Inter-Quartile Range
FDR	False Discovery Rate

List of Symbols

$\mathcal{N}$	Gaussian distribution
$\mathcal{W}$	Watson distribution
$\mathcal{F}$	Von-Mises-Fisher distribution
$\mathcal{S}$	Student's t-distribution
$\{\mathbf{x}_{ki}\} = \mathbf{X}_k$	Position vector of i^{th} point in k^{th} set
$\{\mathbf{X}_k\} = \mathbb{X}$	Group of K point sets
$\{\boldsymbol{\mu}_j\} = \mathbf{M}$	Position vector of j^{th} mixture model component in $\mathbf{M}$
$\mathbf{M}$	Mixture centroids
$P^{\star}_{kij}$	Posterior probability of j^{th} Student's t-distribution
P_{kij}	Posterior probability of j^{th} mixture model component
$\{\mathbf{T}_k\} = \mathbb{T}$	Group of K transformations
$\{\nu_j\} = \Upsilon$	Group of all degrees of freedom in TMM
ν_j	Degrees of freedom of j^{th} TMM component
$\{\pi_j\} = \Pi$	Set of all mixture coefficients
π_j	Mixture coefficient of j^{th} mixture model component
σ^2	Variance
K	Number of samples in a group
M	Number of mixture model components
N_k	Number of data points in k^{th} set
D	Dimension of the data
$\{\mathbf{M}, \sigma^2, \Upsilon, \Pi\} = \Theta$	Set of unknown TMM parameters
$\{\Theta, \mathbb{T}\} = \Psi$	All unknown parameters
$\{\mathbf{d}_{ki}\} = \mathbf{D}_k$	Feature vector of i^{th} hybrid point in k^{th} set
$\{\mathbf{D}_k\} = \mathbb{D}$	Group of K hybrid point sets
$\mathbf{m}^p_j$	Mean position vectors of j^{th} component HMM
$\mathbf{m}^d_j$	Mean orientations of j^{th} component HMM
κ_j	Concentration parameter of j^{th} component of HMM
m^f_j	Mean scalar values of j^{th} component HMM
σ^2_p	Variance of Student's t-distributions in HMM
$\{\mathbf{m}^p_j, \sigma^2_p, \nu_j\} = \Theta_p$	All unknown parameters of Student's t-distributions in HMM

$\{\mathbf{m}_j^d, \kappa_j\} = \Theta_n$	All unknown parameters of Watson/Fisher distributions in HMM
σ_f^2	Variance of Gaussian distributions in HMM
$\{m_j^f, \sigma_f^2\} = \Theta_f$	All unknown parameters of Gaussian distributions in HMM
$\{\mathbf{n}_{ki}\} = \mathbf{N}_k$	Direction vector of i^{th} hybrid point in k^{th} set
$\{\mathbf{N}_k\} = \mathbb{N}$	Group of K samples comprising direction vectors
$\{f_{ki}\} = \mathbf{F}_k$	Scalar value of i^{th} hybrid point in k^{th} set
$\{\mathbf{F}_k\} = \mathbb{F}$	Group of K samples comprising scalar values

Chapter 1

Introduction

Medical image analysis has evolved rapidly in the past few decades, with the advent of sophisticated imaging techniques that provide non-invasive and minimally invasive mechanisms for visualising internal organs, monitoring growth and ageing, and tracking the progression of pathologies over time. The large number of recent and ongoing multi-disciplinary healthcare research projects, such as, the Alzheimer's Disease Neuroimaging Initiative (adni-info.org), International Consortium for Brain Mapping (ICBM, loni.usc.edu/ICBM/), UK-Biobank (ukbiobank.ac.uk) and VPH-DARE@IT (vph-dare.eu) projects, has led to the acquisition of a high volume of imaging and clinical data. This has further popularised the use of probabilistic and statistical techniques, to investigate variation in anatomy and physiology, across populations. Such techniques provide insight into natural and pathological variations observed across cohorts, and consequently, have become crucial tools for computer-aided-diagnosis and computer-assisted-interventions. Statistical shape models in particular, which characterise the variation in shape of an organ of interest, across a population, have found widespread use in applications involving image segmentation, classification, object detection and *in silico* virtual population studies, among others. Statistical analysis of other medical image-derived features related to; diffusion of water in soft tissue, bone mineral density and blood flow, have also shown high potential, to be of practical value in a clinical setting, in the near future.

A basic requirement for statistical analysis of shape and other medical image-derived quantities is the notion of establishing correspondences, across the data set to be analysed (i.e. data can be cross-sectional, comprising multiple subjects, or longitudinal in nature for a single subject/across multiple subjects). This involves identifying corresponding spatial positions across a group of shapes/images, such that appropriate statistical analyses may be conducted

on comparable data. This is achieved by 'registration', which involves estimating suitable affine or non-rigid transformations, warping the shapes/images to a common reference frame, and subsequently, identifying distinct correspondences that represent the same anatomical features, across all samples in the group.

Statistical shape models require segmentations of the organ(s) of interest from medical images. These segmentations can subsequently be used to represent shapes in various ways, prior to analysing the statistics of their variation across a group. The most common of these, relies on point-based descriptions of shape boundaries and this is employed throughout this thesis, due to its simplicity and flexibility. While significant efforts have been made previously, to automatically register shapes (represented as point sets) and establish correspondences, existing approaches have typically required some degree of user intervention, to ensure robustness in the process. Sensitivity to outliers in the data, and the corresponding need to ensure the fidelity of input segmentations, is a key issue in this respect. Such user intervention requirements, however, can be prohibitive when large data sets are involved, such as those acquired within the aforementioned imaging initiatives. The first main contribution of this thesis, therefore, is a probabilistic framework for point set registration which is robust to data outliers, and correspondingly amenable to automated shape analysis.

Statistical analyses of more complex medical image-derived features, such as, measures characterising local water diffusion properties within soft tissues, for example, also require registration of the associated structures/images, to identify correspondences across the population of interest. While a large body of literature exists on the use of image registration techniques for conducting such group-wise analysis, few have approached this problem from the context of generalised point set registration. The term *generalised point sets* is used to refer to data comprising different types of information, obtained from different sources; for example, point sets comprising voxel spatial positions, associated fibre orientations, and a scalar measure reflecting tissue anisotropy. A probabilistic framework that enables automatic and robust registration of generalised point sets, to facilitate group-wise statistical analysis of diffusion image-derived data in particular, forms the second major contribution of this thesis.

The methods proposed herein are general and flexible with regard to their applicability in a variety of medical image analysis and computer vision problems, and shapes and images of various anatomical structures are employed during

development and testing. The focus throughout this thesis, however, is their application in the statistical analysis of shapes and diffusion-derived quantities, obtained from neuroimages. Images from both healthy subjects and patients diagnosed with mild cognitive impairment and Alzheimer's disease are considered. These data sets exhibit significant variability across subjects and patient groups and serve to highlight the efficacy of the proposed techniques.

Chapter 2

Background

2.1 The Human Brain

The human central nervous system (CNS) and, at its core, the brain, is the most sophisticated and complex in nature, responsible for controlling all functions of the body. The brain is partitioned into highly specialized regions, each with unique structural and functional organisation. The significant variability in its structural and functional attributes across populations, necessitates the construction of statistical models and atlases. Models such as these, incorporate region-specific features from multi-modal data and describe the observed variability, in order to improve our understanding of the complex relationship between brain structure and function.

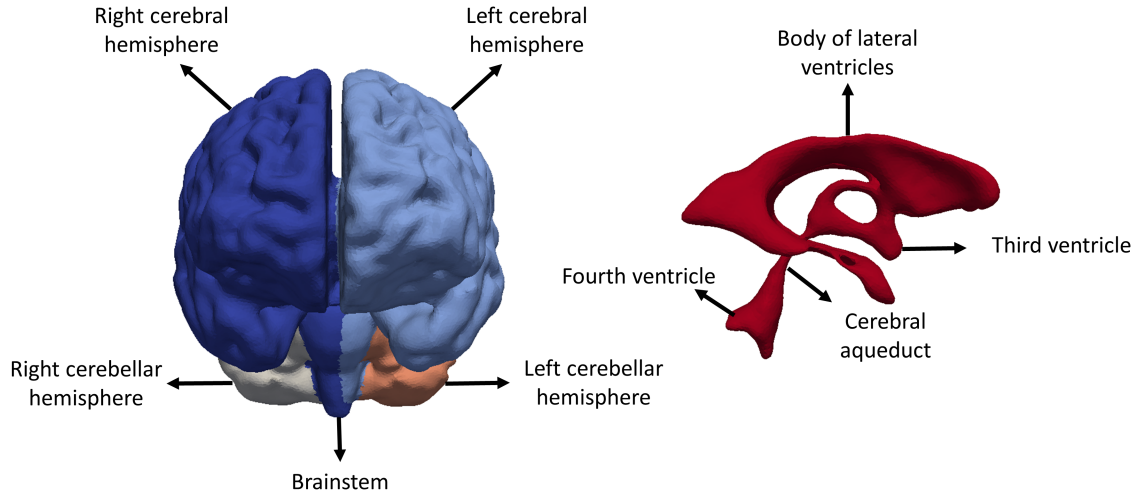

FIGURE 2.1: Major brain regions and the CSF-filled ventricular system.

The brain volume is broadly classified into three regions, namely: the cerebrum, cerebellum and brainstem. It is immersed in cerebro-spinal fluid (CSF),

and encased within the skull for protection. CSF acts as a shock-absorber, providing protection to the brain from impact-induced trauma, and is responsible for nourishing the latter's constituent neuronal cells (neurons). This fluid is produced continuously at the choroid plexus, within central cavities known as the lateral ventricles located inside the cerebrum. From here the fluid is circulated through the third and fourth ventricles, out through the cerebral aqueduct, into the space in between the brain and the skull, referred to as the sub-arachnoid space. Here it is finally re-absorbed at the superior sagittal sinus (Nolte, 2002). The images presented in Fig. 2.1 depict these major brain regions and constituent structures of the ventricular system. The cerebrum comprises two hemispheres connected by the corpus callosum, and is responsible for regulating both, higher order functions such as speech and interpretation, and basic ones such as perception and movement. It can be further categorized into the inner and outer cortex. The latter is characterised by numerous folds, which increase the overall surface area and allow billions of neurons to be densely packed within the brain. These folds are known as gyri and the grooves between successive folds are called sulci. The outer cortex is primarily composed of neuron cell bodies, collectively referred to as grey matter (GM), and is connected to the inner cortex through long myelinated axons called white matter (WM). GM and WM represent the two constituent tissue types of the brain.

Located deep within the cerebrum in the inner cortex are the sub-cortical structures, composed of grey matter. These include — the basal ganglia (comprising structures such as: caudate nuclei, putamen and globus pallidus) and the limbic system (comprising structures such as: amygdali, hypothalamus and hippocampi). Among these, the hippocampi, which are associated with memory, are of particular interest in the study of neurodegenerative disorders like Alzheimer's disease (AD).

2.2 Dementia and Alzheimer's Disease

Dementia is a broad term used to classify a variety of neurodegenerative disorders that result in impaired cognitive functions such as memory, speech and reasoning, among others. AD is a neurodegenerative disease that is the most common cause of dementia. Approximately 35 million people worldwide suffer from various types of dementia, with high mortality rates due to a lack of effective

treatment methods. According to the report published by the Alzheimer's Association (Alzheimer's Association, 2016), approximately 5.4 million people have been diagnosed with AD as of 2016, in America alone. Mild cognitive impairment (MCI), refers to a minor-to-moderate loss in cognitive function, and MCI patients are generally at a higher of developing AD. The role of neuroimaging and specifically, magnetic resonance imaging (MRI), in early diagnosis of MCI and AD is of increasing relevance, with revised diagnostic criteria for the latter, published by the National Institute of Ageing and Alzheimer's Association, in 2011. These now recommend assessment of brain images and the use of image-based biomarkers in clinical practice, to aid in the early diagnosis. MRI modalities offer a non-invasive mechanism for detecting early signs of neurodegeneration, and consequently, are central to identifying descriptive and discriminative biomarkers.

A widely accepted imaging biomarker for AD is the quantitative evaluation of brain tissue atrophy, typically in terms of loss in volume. This is particularly true for brain structures such as the hippocampus, which has been proposed in numerous studies (Frisoni et al., 2002), (Barnes et al., 2004), (Morra et al., 2009), (Leung et al., 2010), as a potential biomarker. In addition to loss in volume, statistical shape analysis has found use in identifying discriminative features to distinguish AD patients from healthy subjects. For example, in (Shen et al., 2012) the authors used SSMs to assess global volume and local shape changes in hippocampi, and derived from these predictors to discriminate between AD patients and healthy subjects. (Zhou et al., 2009) used a combination of statistical shape analysis and permutation testing, to identify significant differences in hippocampal morphology between AD patients and normal controls. In other studies, such as (Ferrarini et al., 2006), SSMs have been employed to characterise localised shape changes in the lateral ventricles, for the same purpose.

In addition to AD-induced pathological changes in GM structures, numerous diffusion tensor imaging (DTI) studies have also reported significant abnormalities in brain WM regions. WM abnormalities have been quantified based on localised changes to diffusion properties such as fractional anisotropy (FA), observed across AD and MCI cohorts, relative to age-matched healthy subjects, (Stricker et al., 2009), (Medina et al., 2006). In (Medina et al., 2006) the authors report substantial overlap in regions with reduced FA between MCI and mild-AD groups, and consequently infer that WM changes occur in MCI prior to the development of AD. Regions affected by impaired WM integrity, were found to be concentrated in the corpus callosum and cingulum, among others. Similarly,

(Stricker et al., 2009) reported greater diminution of microstructural integrity in late myelinating WM tracts (such as the cingulum and corpus callosum) than in early myelinating tracts (like the corona radiata and cerebral peduncles) in AD patients relative to healthy subjects. Statistical analysis of diffusion-derived quantities across multiple subjects, and comparisons between patient groups are potentially further pathways to identification of MCI and AD biomarkers. Such analyses have also found use in longitudinal studies, investigating the onset and progression of AD and other types of dementia.

2.3 Statistical Shape Models and Atlases

Statistical shape models (SSMs) and analysis of shape variations across a population are important tools for a variety of medical image analysis applications. SSMs describe the variation in shape of an object/anatomical structure of interest, about a mean shape representative of the training population. The variation about the mean is described by a reduced set of parameters referred to as the modes of variation. Describing shape variability in this manner first requires registration of the shapes of interest, to identify correspondences and normalize them with respect to rotation, translation and scale. The latter is necessary to exclude any global differences in pose from being incorporated into the SSM. Suitable dimensionality reduction techniques such as Principal Component Analysis (PCA) are subsequently employed to describe the overall variation in shape observed across the training population, with a reduced set of parameters. PCA is a linear dimensionality reduction technique which constructs a low-dimensional representation of the data, in a manner that maximally captures the variation observed across the data set (Jolliffe, 2002). This amounts to identifying a set of uncorrelated, mutually orthogonal basis vectors (or principal eigenvectors) by eigen-decomposition of the covariance matrix, estimated from centred data. Subsequently, the training data can be approximated using a linear combination of the estimated basis vectors.

Structured (triangulated meshes) and unstructured point-based representations of shape are the most popular for constructing SSMs, due to their simplicity and flexibility. The type of shape representation also influences the subsequent choice of method for registering shapes and modelling shape variability. SSMs trained by PCA using point-based representations are often referred to as point distribution models (PDM), coined by (Cootes et al., 1995). Other forms of shape

representation often employed for shape analysis include: Fourier shape descriptors (Staib and Duncan, 1996), spherical harmonics (Gerig et al., 2001a), implicit descriptions using signed distance maps (Leventon, Grimson, and Faugeras, 2000), and medial models (Styner et al., 2004). While early work in training PDMs relied on manually specified landmarks delineating the shapes of interest, such an approach is prohibitively expensive for large data sets, comprising 3D anatomical structures.

(Hufnagel et al., 2007) proposed an automatic probabilistic approach to jointly establish correspondences and align shapes of interest, by considering each shape to be transformed observations of a Gaussian mixture model (GMM). Consequently, a probabilistic view of correspondences (or soft correspondences) was proposed rather than an exact on-to-one mapping (hard correspondences) between shapes, as with previous approaches. These soft correspondences were subsequently used to train SSMs by PCA, as in previous approaches relying on hard correspondences. In another study (Hufnagel et al., 2009) extended their approach to directly estimate the modes of variation from the GMM (removing the need for performing PCA separately) in a unified fashion, within a maximum-a-posteriori (MAP) framework. Such a generative approach helps address a limitation of standard PCA-based SSM construction, allowing it to model missing data, and provides a sound mathematical framework for modelling variation in shape. Although employing PCA for SSM construction is an approximation, which assumes the group of shapes to be normally distributed, it has been used successfully in a variety of applications and is of considerable practical value. In a recent study (Gooya et al., 2015), a more sophisticated generative model based on mixtures of probabilistic PCA models was proposed, to automatically estimate the modes of variation, within a Bayesian clustering framework. Such a formulation is well-suited to modelling multi-modal shape distributions, and enables automatic model selection, i.e. the optimal number of mixture components and modes of variation are directly estimated during the clustering process. Additionally, this approach enabled un-supervised classification of shapes, based on their geometry. Consequently, such an approach can be used to automatically identify the optimal number of sub-groups for any given population of shapes and thereby distinguish between natural anatomical variations in shape and those induced by pathology.

Definition of a standardized reference co-ordinate system is essential for analysing medical images across multiple subjects. For 3D brain images, one such widely employed reference frame is the Talairach space, used to spatially

normalize brain structures from multiple subjects' images. It provides a mechanism for constructing population-atlases describing morphological and physiological variations of the brain, across large cohorts. Such atlases provide a systematic framework for identifying relationships between ageing and disease progression, and the observed inter-subject variations. Construction of such atlases thus involves definition of a reference co-ordinate space and choice of a suitable spatial transformation mapping each subjects' image, from its native space to the chosen reference space. Choice of the former and latter are typically tailored to each application, which has resulted in a plethora of structural and functional brain atlases in recent years. Various medical image analysis and clinical applications such as automatic segmentation of brain images, neurodegenerative disease classification, and image-guided neurosurgery, are facilitated through the construction and application of suitable brain atlases.

Construction of structural and functional atlases of the human brain began as early as 1992, when the International Consortium for Brain Mapping (ICBM) was founded (Mazziotta et al., 2001). ICBM began formulating a voxel-based 4D (three spatial and one temporal) probabilistic atlas of the brain, incorporating data from multiple sources including imaging, DNA and lifestyle information, across a large and diverse demographic of subjects. Initiatives of this ilk, have naturally led to the construction of pathology- and demographic-specific atlases, describing the progression of neurodegenerative diseases such as AD. Statistical and probabilistic atlases are in general better representations of a population than are single templates or atlases, as they account for the inherent inter-subject variability. Magnetic resonance images (MRIs) from 150 young adults were acquired within the ICBM, co-registered to a common reference frame, and used to construct the average ICBM-152 atlas (Mazziotta et al., 2001). The latter is widely used in a variety of brain mapping software tools such as SPM (http://www.fil.ion.ucl.ac.uk/spm/) and FSL (https://fsl.fmrib.ox.ac.uk/fsl/fslwiki/). Other studies of note include; (Hammers et al., 2003), who proposed a framework for constructing maximum probability atlases from T1-weighted MRIs of young adults; and (Fischl, Sereno, and Dale, 1999), (Lyttelton et al., 2007), who proposed surface-based atlases of the cortex to adequately model variations in the complex folded structure of sulci and gyri across multiple subjects. These were generated using surface-matching techniques, rather than volumetric atlases estimated using image registration. Various studies have also proposed techniques to generate region-specific (Hammers et al., 2007), disease-specific (Thompson et al., 2001), and WM atlases (Mori et al.,

2008) (of its constituent fibre tracts). In the context of the latter, (Durrleman et al., 2011) proposed a joint registration and atlas construction framework for WM fibre bundles based on diffeomorphisms and currents, enabling statistical analysis of their variation across populations. A thorough review of conventional and state-of-the-art neuroanatomical atlases and a discussion of expected future trends in the field, is presented in (Evans et al., 2012).

2.4 Thesis Aims and Objectives

The primary aim of this thesis is to formulate an automatic and robust framework for group-wise registration of generalised point sets, to enable statistical analysis of shapes and other features of interest such as diffusion-derived quantities. Two main objectives are defined to this end:

- Formulate an automated group-wise, probabilistic, shape registration framework based on mixtures of Student's t distributions, which correspondingly affords robustness to data outliers.
- Design a general framework for joint registration and clustering of multi-dimensional point sets, that comprise disparate data features such as positions, orientations and scalar quantities (such as derived from diffusion MR data).

2.4.1 Thesis Structure and Outline

The work undertaken and the methods proposed in this thesis, in line with the discussed objectives, are presented in chapters 3-5. Concluding remarks summarising major findings and a discussion of the limitations and potential improvements for the presented work are outlined in Chapter 6.

A Student's t-mixture model -TMM- based group-wise point set registration framework, for rigid and non-rigid registration, is presented in **chapter 3**. A multi-resolution extension (mrTMM) to the same is also outlined. The inherent robustness of TMM and mrTMM to outliers in the data and their consequent influence on registration accuracy is evaluated and compared with state-of-the-art GMM-based methods, using both synthetic and clinical data. Furthermore, the advantages of mrTMM over single-resolution TMM, in terms of registration accuracy and computational efficiency are also discussed.

The proposed TMM-based registration techniques are used to construct SSMs by PCA, using automated techniques to generate the requisite training segmentations. The quality of the resulting models are evaluated in terms of generalisation, specificity, and compactness, and compared with those obtained using GMM-based methods, in **chapter 4**.

A hybrid mixture model for joint registration and clustering of generalised point sets, comprising, multiple data features such as spatial positions, orientations and scalar measures, is presented in **chapter 5**. The proposed approach is employed for multi-subject analysis of diffusion-derived quantities such as white matter (WM) fibre orientation and fractional anisotropy (FA), across patients diagnosed with AD and MCI, and healthy subjects. Hypothesis tests investigating significant variations in FA between patient groups are conducted. The potential of the proposed framework to facilitate automatic region-of-interest analyses of diffusion data across multiple subjects, and to parcellate their WM volumes into homologous regions, is also discussed.

The contributions described in this thesis have been adapted from articles published in peer-reviewed conference proceedings and journals. Specifically, **chapter 3** is a combination of the work presented in (Ravikumar et al., 2015), (Ravikumar et al., 2016b), (Ravikumar et al., 2016a) and (Ravikumar et al., 2017 Under review[b]), **chapter 4** is based on (Ravikumar et al., 2017 Under review[b]) and **chapter 5** draws upon work presented in (Ravikumar et al., 2017 Under review[a]) and (Ravikumar et al., 2017).

Chapter 3

Shape Registration

3.1 Introduction

Registration of surfaces, curves or point sets and correspondence estimation is an open problem in computer vision and medical image analysis and has received significant attention over the past few decades. Early work in the field includes the well known and widely used generalized Procrustes (GP) (Gower, 1975) and iterative closest point (ICP) (Besl and McKay, 1992) algorithms and various extensions of the same, namely, soft-assign Procrustes (Rangarajan et al., 1997) and EM-ICP (Granger and Pennec, 2002),(Hufnagel et al., 2008),(Hermans et al., 2011), respectively. These techniques rely on point-based representations of shapes to align and establish correspondences across the same. The main limitations of the GP method are its requirement for correspondences to be determined prior to alignment and high sensitivity to outliers (as the Euclidean distance is minimised between shapes). The conventional ICP algorithm relies on establishing exact correspondences by identifying the closest point pairs in the shapes to be aligned. Although such an approach is computationally very efficient, it is also severely affected by the presence of outliers in the point sets being aligned as this may lead to the estimation of incorrect correspondences and consequently sub-optimal transformations. Additionally, ICP is also constrained by the need for the two shapes to be well-aligned initially, to satisfy the assumption that closest point pairs correspond to each other, a non-trivial problem in medical imaging applications.

Subsequent approaches have employed different types of features for registration and adopted a probabilistic view of estimating correspondences, to address the limitations of nearest neighbour based techniques (such as ICP). In such approaches, correspondence for each point on one shape is formulated as a weighted combination of all points on the other shape, where the

weights/probabilities are derived from a probabilistic function of the pairwise distances (typically the squared Mahalanobis distance) between the shapes. These include: the robust point matching (RPM) method, which utilises point/edge-based features, a soft-assign algorithm for establishing correspondence, and deterministic annealing optimisation for rigid (Rangarajan et al., 1997) and non-rigid (Chui and Rangarajan, 2003) point matching; deformable surface registration algorithms based on currents (Vaillant and Glaunès, 2005),(Durrleman et al., 2007); and others that employ diffeomorphic transformations in combination with local geometry descriptors such as integral volume (Gelfand et al., 2005) and surface curvatures (Wang, Peterson, and Staib, 2003).

Probabilistic approaches to point set registration are of particular interest as they are topology independent and are tailored to address the challenges of, different cadinalities (number of points), missing information and varying degrees of outliers, common to medical-image derived point sets. In recent years, various such methods have been formulated, including: coherent point drift (CPD) (Myronenko and Song, 2010), a pair-wise method for both rigid and non-rigid registration; joint registration of multiple point clouds (JRMPC) (Evangelidis et al., 2014), which is analogous to a group-wise version of strictly rigid-CPD (i.e. only rotation and translation estimated; does not estimate global scaling during alignment); robust pair-wise point set registration using Gaussian mixture models (Jian and Vemuri, 2011), where the point sets are represented as independent GMMs and are aligned by minimizing the L^2-norm between them; and a variety of GMM-based group-wise, rigid (Granger and Pennec, 2002),(Hufnagel et al., 2008), (Gooya, Davatzikos, and Frangi, 2015) and non-rigid (Rasoulian, Rohling, and Abolmaesumi, 2012), (Wang, Vemuri, and Rangarajan, 2006), (Chen et al., 2010) registration methods. In the context of training SSMs, which is of particular interest in this thesis, the recent work of (Gooya, Davatzikos, and Frangi, 2015) is most relevant, as their method (sparse statistical shape models or SpSSM) was shown to produce SSMs of higher quality than a conventional GMM-based method, namely, EM-ICP, proposed by (Hufnagel et al., 2008). SpSSM employs a symmetric Dirichlet prior for the mixture coefficients to enforce sparsity (sparsity level is a user specified parameter, $s_p = [0, 1]$) and identify and prune out mixture components with low probability in explaining the observed data. Such an approach starts from a maximal mean model, with a high density of points which are subsequently removed as the registration progresses and the probability of model points drops below a threshold enforced by the specified sparsity level. The pruning process for the removal of such model points is achieved via

quadratic programming, using a generalised sequential minimal optimiser. Consequently, the number of mixture components used for a given data set is selected over a continuous rather than discrete search space.

The problem of automatic SSM construction has been tackled previously in different ways, some of which include, pair-wise template-to-training set registration, population-based techniques and group-wise shape registration methods. The third class of approaches is well-suited to automatic SSM generation as it combines the process of rigid shape alignment and correspondence estimation in a unified framework, unlike population-based methods where these two steps are often de-coupled. Furthermore, they can be imbued with inherent robustness to outliers and missing information in the data, through suitable stochastic formulations of the problem. In this chapter, we propose a Student's t-mixture model (TMM) based group-wise, rigid and non-rigid registration framework for unstructured point sets, which exploit the robustness of t-distributions to outliers and harnesses the generative property of probabilistic model-based registration, to accommodate missing data. Most existing probabilistic point set registration approaches employ conventional GMMs, as in (Hufnagel et al., 2008),(Rasoulian, Rohling, and Abolmaesumi, 2012) or mixture models that combine Gaussian components with a weighted uniform distribution component designed to model noise and outliers that may be present in the data, as in CPD (Myronenko and Song, 2010) and JRMPC (Evangelidis et al., 2014). Although the latter have been shown to outperform the former in the presence of outliers, one limitation is their need for manual tuning of the weight that controls the influence of the uniform distribution component relative to the Gaussian components. Consequently, prior knowledge of the degree of noise and outliers present in the data being registered is often necessary. As this information is typically unavailable, a framework that is inherently robust to noise and outliers is highly desirable. TMM-based methods potentially offer a solution, as demonstrated in two previous studies on pair-wise rigid (Gerogiannis, Nikou, and Likas, 2009) and non-rigid (Zhou et al., 2014) registration. We proposed two variants of TMM-based group-wise rigid registration recently, (Ravikumar et al., 2016b) and (Ravikumar et al., 2016a), (Ravikumar et al., 2017 Under review[b]), respectively. In the former, a numerical approach (gradient-ascent optimisation) was adopted to estimate the desired transformation parameters, while in the latter two studies these were estimated analytically by deriving closed-form expressions for the same. Furthermore, in (Ravikumar et al., 2016a) (Ravikumar et al., 2017 Under review[b]), we outlined a multi-resolution extension to the TMM algorithm

(mrTMM), which showed improvement in registration accuracy, computational efficiency, and SSM quality relative to the single-resolution approach.

The first part of this chapter focuses on probabilistic rigid registration methods (i.e. transformation parametrised by 7 degrees of freedom in 3D: rotation, scaling, and translation) for point sets using TMMs, as the main application of interest is the automatic construction of SSMs from medical images. The latter requires: independence to topology, ability to handle shapes with different cardinalities (varying point counts), robustness to outliers, ability to accommodate missing information, and recover large rigid transformations in the presence of significant variations in shape. Additionally, group-wise registration approaches are of particular interest as they are able to estimate the desired similarity transformations and establish correspondences in an unbiased manner — a limitation of pair-wise approaches (such as conventional CPD) employed in a one-to-many registration strategy. The latter class of techniques often do not account for any outliers or missing data that may be present in the template shape, which can affect the registration and correspondence estimation process and ultimately result in SSMs of lower quality. The second part of the chapter outlines a group-wise non-rigid registration framework based on TMMs, to enable accurate estimation of correspondences for complex geometries showing significant, non-linear shape variations across a group, and where rigid registration alone is inadequate.

3.2 Probabilistic Mixture Models for Shape Registration

Mixture models are a weighted linear combination of probabilistic components, often used to approximate complex data distributions under the assumption that the data are independent and identically distributed (i.i.d). By formulating a joint distribution over both the observed and hidden latent variables, the distribution of the former can be approximated by marginalizing out the latent variables (Bishop, 2006). They are often employed to cluster data using a frequentist approach such as maximum likelihood (ML) estimation, to identify the parameters of the mixture model. ML estimation is achieved by expectation-maximisation (EM) (Dempster, Laird, and Rubin, 1977) which alternates between two steps: the E-step where the posterior probabilities (expectation of the latent variables), which describe the responsibility of a mixture model component in explaining

the observed data, are computed; and the M-step, in which the computed posteriors are employed to estimate the parameters of the mixture model components. Together, mixture models and the EM algorithm form a powerful framework widely employed in medical image analysis. Here they are used to formulate a probabilistic, group-wise rigid registration framework capable of aligning shapes (represented as point sets) to a common reference frame and establishing correspondences in a manner independent of their topologies and discretisation (i.e. number of points used to represent each shape), while being robust to outliers. Group-wise point set registration using mixture models is analogous to clustering data, except the data, i.e. points representing each shape in the group, are considered to be transformed observations sampled from the model. Consequently, transformations that align the shapes are treated as model parameters.

3.2.1 Probability Distributions: Gaussian vs. Student's t

The Student's t-distribution $\mathcal{S}$, a generalization of the Gaussian distribution, can be expressed as an infinite mixture of (scaled) Gaussians, with identical means $\boldsymbol{\mu}$ but different covariances. t-distributions have heavier tails than Gaussians and thus are inherently more robust when fitting to data containing outliers (Bishop, 2006). For the multivariate case (equation 3.1b), a t-distribution is derived by imposing a Gamma distribution $\mathcal{G}$ as a prior on the covariance $\boldsymbol{\Sigma}$ [1] of a multivariate Gaussian distribution $\mathcal{N}$ and marginalising out the scaling weights u drawn from $\mathcal{G}$. This is achieved by evaluating the integral shown in equation 3.1a.

$$\mathcal{S}(\mathbf{x}|\boldsymbol{\mu}, \boldsymbol{\Sigma}, \nu) = \int_0^\infty \mathcal{N}(\mathbf{x}|\boldsymbol{\mu}, \boldsymbol{\Sigma}/u)\mathcal{G}(u|\nu/2, \nu/2)du \tag{3.1a}$$

$$\mathcal{S}(\mathbf{x}|\boldsymbol{\mu}, \sigma^2, \nu) = \frac{\Gamma(\frac{\nu+D}{2})}{\Gamma(\nu/2)(\pi\nu\sigma^2)^{D/2}[1 + \frac{\Delta^2}{\nu}]^{\frac{\nu+D}{2}}} \tag{3.1b}$$

$$\Delta^2 = \frac{(\mathbf{x} - \boldsymbol{\mu})^T(\mathbf{x} - \boldsymbol{\mu})}{\sigma^2} \tag{3.1c}$$

where Δ^2 represents the squared Mahalanobis distance evaluated between the observed data $\mathbf{x}$ and a t-distribution centred at $\boldsymbol{\mu}$ with variance σ^2, Γ represents the gamma function and D the dimensionality of the data.

[1] Here and throughout this thesis we assume isotropic covariance i.e. $\boldsymbol{\Sigma} = \sigma^2\mathbf{I}$

We assume isotropic covariance for the mixture model throughout our work as there is no closed-form solution for the registration parameters, using a general anisotropic covariance model (Horaud et al., 2011). Consequently, although numerical optimization techniques may be adopted for the same, this leads to a substantial decrease in computational efficiency. However, based on the results reported in (Horaud et al., 2011), an anisotropic covariance model may improve registration accuracy, particularly when the data is corrupted by anisotropic Gaussian noise.

The t-distribution is parametrised by ν, which represent the degrees of freedom that control the shape of the distribution and its heavy-tails. In the limit $\nu \rightarrow \infty$ the t-distribution tends towards Gaussian behaviour and the effect of varying ν, for the univariate case, is further illustrated in Fig. 3.1 a. To demonstrate the robust nature of t-distributions, univariate data sampled from a normal distribution and subsequently corrupted by the inclusion of random outliers, were fitted with a Gaussian and Student's t-distribution. The resulting probability density function (pdf) estimates for both distributions are very similar for data without outliers (Fig. 3.1 b). However, as illustrated by Fig. 3.1 c, the response of the Gaussian distribution is heavily distorted for data containing outliers while the t-distribution remains relatively unchanged and centred on the original, true mean value.

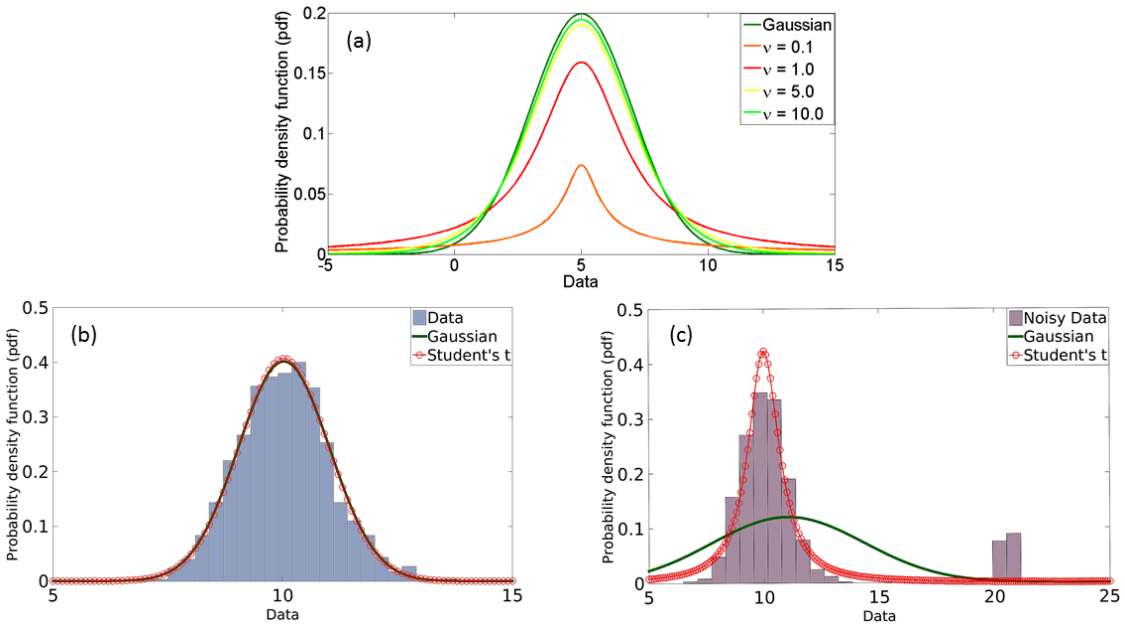

FIGURE 3.1: (a) Plot depicting the influence of ν on the shape of t-distributions, showing increasing similarity to overlaid Gaussian distribution with increase in its magnitude. Maximum likelihood fits of univariate Gaussian and Student's t-distribution to uncorrupted data (b) and data corrupted by random noise (c) overlaid on their respective histogram distributions.

3.2.2 Pair-wise Registration

Coherent point drift (CPD) proposed by (Myronenko and Song, 2010) is a widely used pair-wise point set registration technique, capable of recovering rigid, affine and non-rigid transformations. CPD employs Gaussian radial basis functions to parametrise non-linear transformations and the associated basis function weights are estimated as parameters of the mixture model, by maximising the likelihood function using EM. Rigid, similarity and affine transformations may also be estimated in a similar manner. As with other probabilistic registration methods, CPD considers the problem of non-rigid point-set registration, one of probability density estimation. Here the 'moving' point-set (i.e. the shape to be deformably registered to the fixed or reference shape), is considered to represent the centroids of a Gaussian mixture model (GMM) and is fit to the second point-set (considered as data points) by likelihood maximisation, using the expectation-maximisation (EM) algorithm.

$$p(\mathbf{x}|\mathbf{y}_j, \theta) = \frac{1}{(2\pi\sigma^2)^{D/2}} \exp^{-\frac{\left\|\mathbf{x}-\mathbf{T}\mathbf{y}_j\right\|^2}{2\sigma^2}} \tag{3.2a}$$

$$p(\mathbf{x}_n|\mathbf{Y},\theta) = \frac{w}{N} + (1-w)\sum_{j=1}^{M}\frac{p(\mathbf{x}_n|\mathbf{y}_j,\theta)}{M}, 0 \leq w \leq 1; \tag{3.2b}$$

The key assumptions in such an EM-based probabilistic pair-wise registration method are, each data points $\{\mathbf{x}_{n=1\ldots N}\} = \mathbf{X}$ defining the 'fixed' point set, are considered to be independent and identically distributed (i.i.d), and a noisy observation generated from a Gaussian distribution centred at a point belonging to the moving point-set. Equation 3.2a describes the likelihood of a point $\mathbf{x}$ (in the fixed point-set), being sampled from a GMM-component centred at $\mathbf{T}\mathbf{y}_j$. $\mathbf{T}$ represents the desired spatial transformation (which may be rigid, similarity, affine or non-rigid) and D, the dimensionality of the point-sets. θ denotes the set of all model parameters comprising centroid positions $\mathbf{y}_j$, variance σ^2 and transformations $\mathbf{T}$. Equation 3.2b describes the conditional probability of $\mathbf{x}$, assuming equally weighted Gaussian components in the mixture model, with an additional uniform distribution component (specified by the first term in the equation), where — N denotes the number of points in the 'fixed' point-set $\{\mathbf{x}_{n=1\ldots N}\} = \mathbf{X}$; M the number of GMM components or points in the 'moving' point-set $\{\mathbf{y}_{j=1\ldots M}\} = \mathbf{Y}$; w balances the influence of the Gaussian and uniform distributions in the mixture model, to accommodate noise/outliers; and $\{\sigma^2, \mathbf{T}\} = \theta$ denotes the set of model and registration parameters to be estimated.

The i.i.d assumption for the data, allows the joint log-likelihood across all data points to be expressed as a product of the individual conditional probabilities $p(\mathbf{x}|\mathbf{Y},\theta)$, resulting in the log-likelihood function shown in equation 3.3a. The desired transformations and model parameters, θ, can be estimated by maximising the log-likelihood function directly, using gradient-based optimisation techniques. Or alternatively, using the EM algorithm θ may be estimated iteratively, by minimising the expected complete data negative log- likelihood function $Q(\theta^t|\theta^{t-1})$, as described by equation 3.3c. In this case, analytical solutions exist for updating estimates of the model and transformation parameters, at each EM-iteration. Q is also an upper bound of the negative log-likelihood function, which is minimised instead of the latter as its solution is intractable. Here and throughout this chapter superscript t denotes the current EM-iteration of the algorithm.

$$p(\mathbb{X}|\mathbf{Y},\theta) = \sum_{n=1}^{N}\ln p(\mathbf{x}_n|\mathbf{Y},\theta) \tag{3.3a}$$

$$\theta^t = \arg\max_{\theta} p(\mathbb{X}|\mathbf{Y}, \theta) \equiv \arg\min_{\theta} Q(\theta^t|\theta^{t-1}) \tag{3.3b}$$

$$Q(\theta^t|\theta^{t-1}) = -\sum_{n=1}^{N}\sum_{j=1}^{M} p(\mathbf{y}_j|\mathbf{x}_n, \theta^{t-1}) \ln(p(\mathbf{x}_n|\mathbf{y}_j, \theta)) \tag{3.3c}$$

EM-based minimisation of $Q(\theta^t|\theta^{t-1})$ is achieved by iteratively alternating between two steps: the expectation (E)-step, where the previous iteration's estimate for the models parameters θ^{t-1}, are used to compute the posterior probabilities of GMM components $p^{(t)}(\mathbf{y}_j|\mathbf{x}_n)$; and the maximisation (M)-step, which uses the estimated posterior probabilities to minimise $Q(\theta^t|\theta^{t-1})$ (refer to equation 3.3c) with respect to each unknown parameter, obtaining revised estimates for $\mathbf{T}^t, \sigma_t^2$. The posterior probabilities estimated in the E-step represent the probability of correspondence between a GMM centred at $\mathbf{T}\mathbf{y}_j$ and an observed data point $\mathbf{x}_n$. They give rise to the notion of soft-correspondences, characteristic of probabilistic registration/clustering approaches. These posterior probabilities are computed using Bayes' theorem as:

$$\begin{aligned} E-step: p(\mathbf{y}_j|\mathbf{x}_n) &= \frac{p(\mathbf{y}_j)p(\mathbf{x}_n|\mathbf{y}_j)}{p(\mathbf{x})} \\ &= \frac{\exp^{-\frac{1}{2}\left\|\frac{\mathbf{x}_n - \mathbf{T}\mathbf{y}_j}{\sigma^2}\right\|^2}}{\sum_{j=1}^{M}\exp^{-\frac{1}{2}\left\|\frac{\mathbf{x}_n - \mathbf{T}\mathbf{y}_j}{\sigma^2}\right\|^2} + (2\pi\sigma^2)^{D/2}\frac{wM}{(1-w)N}} \end{aligned} \tag{3.4}$$

In equation 3.4, $p(\mathbf{y}_j)$ represents the mixture coefficients, which can be explicitly estimated at each M-step of the algorithm. CPD however, assumes equal mixing probabilities for all Gaussian components in the mixture model. $p(\mathbf{x})$ represents the marginal distribution of the data, obtained by summing the joint distribution over all $j = 1...M$ mixture components. For the specific case of non-rigid registration using CPD, revised estimates for the unknown model parameters θ^t at the t^{th} EM-iteration are obtained by minimising the form Q shown in equation 3.5.

$$
\begin{aligned}
M-step : Q(\theta^t|\theta^{t-1}) \\
&= \arg\min_{\theta} \frac{1}{2\sigma^2} \sum_{n=1}^{N} \sum_{j=1}^{M} p(\mathbf{y}_j|\mathbf{x}_n, \theta^{t-1}) ||\mathbf{x}_n - (\mathbf{y}_j + v(\mathbf{y}_j))||^2 \\
&\quad + \frac{D}{2} \ln(\sigma^2) \sum_{n=1}^{N} \sum_{j=1}^{M} p(\mathbf{y}_j|\mathbf{x}_n, \theta^{t-1}) + \frac{\lambda}{2} \phi(v)
\end{aligned} \tag{3.5}
$$

The non-rigid transformation in CPD, is defined as some initial position (given by the moving point set), plus a displacement function $v(\mathbf{y}_j)$, as shown in equation 3.5. In (Myronenko and Song, 2010) the authors show that by regularizing the norm of v, a spatially smooth displacement field may be estimated. Regularization of this nature is akin to employing a prior on the displacement field of the form $p(v) = \exp^{-\frac{\lambda}{2}\phi(v)}$, where $\phi(v)$ represents the regularization term and λ controls the trade-off between registration accuracy and smoothness of the deformation field. The last term in equation 3.5 represents such a regularisation once incorporated into Q. A 'coherence' constraint (equivalent to the regularisation used in motion coherence theory) is enforced on the estimated deformation field in this manner, which forces points in close proximity to move together. By expressing $\phi(v)$ in a Reproducing Kernel Hilbert Space (RKHS) using a Gaussian kernel, the authors in (Myronenko and Song, 2010) showed that the function $v(\mathbf{y}_j)$ which minimizes the upper bound Q (refer to equation 3.5), can be expressed as a linear combination of Gaussian radial basis functions. Correspondingly, the non-rigid registration process involves iterative estimation of the basis function coefficients as parameters of the mixture model, by minimising Q. In summary, the E-step computes the posterior probabilities of the GMM components, the M-step updates estimates for the model and transformation parameters, based on the computed posterior probabilities. The algorithm iteratively alternates between these two steps until a convergence criterion is reached.

3.2.3 Group-wise Rigid Registration using Student's t-Mixture Model

Group-wise point set registration using mixture models is analogous to clustering data, except the data i.e. points representing each shape in the group, are considered to be transformed observations sampled from a central mixture model.

Consequently, transformations that align the data are treated as model parameters (similar to the mean, variance of Gaussian components in a GMM, for example). As highlighted previously, Student's t-distributions (or t-distributions) are a robust alternative to Gaussian distributions when modelling data with outliers. A variety of algorithms using GMMs for both pair-wise and group-wise point set registration, have been proposed in recent years. There are however relatively few studies that investigate the use of a mixture of t-distributions for the same. TMMs have been used previously for clustering noisy data and shown to outperform GMMs due to their robust nature (Peel and McLachlan, 2000) (Svensén and Bishop, 2005). Consequently, by formulating a t-mixture model (TMM) based group-wise registration framework to approximate the joint probability density of a group of point sets (representing shapes) and align them to a common reference frame, estimation of the desired transformations and soft-correspondences (across the group of shapes) is achieved with correspondingly greater degree of robustness to outliers. Such a group-wise framework allows for the unbiased estimation of a mean shape/mean model which is iteratively refined and aligned to each sample shape in a group. The estimated transformations aligning the mean model to each sample shape are subsequently used to robustly align all sample shapes in the group and establish soft-correspondences.

For a training set of K shapes $(k = 1...K)$, where $\{\mathbf{x}_{ki}\} = \mathbf{X}_k$ represents the i^{th} point $(i = 1...N_k)$ on the k^{th} shape, we assume there exists a t-distribution centred at $\mathbf{T}_k\boldsymbol{\mu}_j$, from which it is sampled. Additionally, all points $\mathbf{x}_{ki}$ on all K shapes in the group are assumed to be i.i.d. Henceforth subscript $(j = 1...M)$ is used to represent mixture components, $\{\boldsymbol{\mu}_j\} = \mathbf{M}$ represents the centroids of the model $\mathbf{M}$ and $\{\mathbf{T}_k\} = \mathbb{T}$ represents the similarity transformation, parametrised by rotation $\mathbf{R}_k$, scaling s_k and translation $\mathbf{t}_k$, that aligns the mean model $\mathbf{M}$ to the k^{th} shape in the training set and $\mathbf{X}_k$ represents the set of all points on the k^{th} shape in the training set. The conditional probability of a data point being sampled from a mixture component can thus be expressed as in equation 3.6a.

$$p(\mathbf{x}_{ki}|\mathbf{T}_k, \boldsymbol{\mu}_j, \sigma^2, \nu_j) = \mathcal{S}(\mathbf{x}_{ki}|\mathbf{T}_k\boldsymbol{\mu}_j, \sigma^2, \nu_j) \tag{3.6a}$$

$$p(\mathbf{x}_{ki}|\mathbf{T}_k, \mathbf{M}, \sigma^2, \Upsilon, \Pi) = \sum_{j=1}^{M} \pi_j \mathcal{S}(\mathbf{x}_{ki}|\mathbf{T}_k\boldsymbol{\mu}_j, \sigma^2, \nu_j) \tag{3.6b}$$

The conditional probability density for any data point $\mathbf{x}_{ki}$ on a training shape

being sampled from the M-component mixture of t-distributions can subsequently be formulated using the sum rule of probability, as shown in equation 3.6b. Here $\{\nu_j\} = \Upsilon$ represents the set of all degrees of freedom parameters in the mixture and $\pi_j = \Pi$ represents the set of all mixture coefficients. Next, assuming that all data points on a training shape are independent and identically distributed (i.i.d) the joint probability density for all N_k points on the k^{th} shape can be expressed as the product of the individual conditional densities, as described in equation 3.7a. Here $\{\mathbf{M}, \sigma^2, \Upsilon, \Pi\} = \Theta$ represents the set of all model parameters.

$$p(\mathbf{X}_k|\mathbf{T}_k, \Theta) = \prod_{i=1}^{N_k} p(\mathbf{x}_{ki}|\mathbf{T}_k, \Theta) \tag{3.7a}$$

$$\ln(p(\mathbb{X}|\mathbb{T}, \Theta)) = \sum_{k=1}^{K} \ln(p(\mathbf{X}_k|\mathbf{T}_k, \Theta)) \tag{3.7b}$$

$$\mathbb{T}, \Theta = \arg\max_{\mathbb{T},\Theta} \ln[p(\mathbb{T}, \Theta|\mathbb{X})] \tag{3.7c}$$

Finally the log likelihood function of the complete training set $\{\mathbf{X}_k\} = \mathbb{X}$ can be expressed in similar fashion assuming the K training shapes are i.i.d (equation 3.7b). The optimal set of unknown parameters denoted $\Psi = \{\Theta, \mathbb{T}\}$ can be interpreted as those that maximise the posterior probability given by equation 3.7c or conversely the log-likelihood in equation 3.7b. There is however, no closed-form solution to maximising equation 3.7c and consequently, the conditional expectation of the complete data log-likelihood Q (refer to equation 3.8b) is maximised iteratively with respect to each of the unknown parameters Ψ using the expectation-maximisation (EM) framework, based on Bayes' theorem. Q is derived (similar to (Peel and McLachlan, 2000)) by computing the conditional expectation of the complete data log-likelihood L (refer to equation 3.8a) and treating the membership of data points $\mathbf{x}_{ki}$ to mixture components, and the covariance scaling weights of the latter, as latent variables $\{z_{kij}\} = \mathbb{Z}$ and $\{u_{kij}\} = \mathbb{U}$ respectively. The likelihood function is derived as a product of the marginal density of $\mathbb{Z}$, the conditional density of $\mathbb{U}$ given $\mathbb{Z}$, and the observed data $\mathbb{X}$ given $\mathbb{Z}$ and $\mathbb{U}$.

$$\begin{aligned} L(\Psi) &= \ln(p(\mathbb{X}, \mathbb{U}, \mathbb{Z}|\Psi)) \\ &= \ln(p(\mathbb{Z}|\Psi)) + \ln(p(\mathbb{U}|\mathbb{Z}, \Psi)) + \ln(p(\mathbb{X}|\mathbb{U}, \mathbb{Z}, \Psi)) \end{aligned} \tag{3.8a}$$

At the $(t+1)^{\text{th}}$ EM-iteration the current conditional expectation of the complete data log-likelihood, given the previous iteration's estimate for the model

parameters Ψ^t, is expressed as:

$$Q(\Psi^{t+1}|\Psi^t) = \sum_{k=1}^{K}\sum_{i=1}^{N}\sum_{j=1}^{M}\Bigg[P_{kij}^t\Bigg[\ln(\pi_j) - \ln(\Gamma(\frac{\nu_j}{2})) + \frac{\nu_j}{2}\ln(\frac{\nu_j}{2}) + \frac{\nu_j}{2}[(\ln(U_{kij}^t) - U_{kij}^t) + \psi(\frac{\nu_j^t + D}{2}) - log(\frac{\nu_j^t + D}{2})] - \frac{D}{2}\ln(2\pi) - \frac{1}{2}\ln(\sigma^6) + \frac{D}{2}\ln(U_{kij}^t) - \frac{U_{kij}^t}{2}[1 + \frac{(\mathbf{x}_{ki} - \mathbf{T}_k\boldsymbol{\mu}_j)^T(\mathbf{x}_{ki} - \mathbf{T}_k\boldsymbol{\mu}_j)}{\sigma^2}]\Bigg]\Bigg], \tag{3.8b}$$

where, Γ is the Gamma function, P_{kij} represents the posterior probability of an observed data point $\mathbf{x}_{ki}$ being drawn from a mixture component centred at $\boldsymbol{\mu}_j$ with ν_j degrees of freedom and U_{kij} represents the scaling weights of the equivalent Gaussian distribution (i.e. these are derived from the expression of multi-variate t-distributions as an infinite mixture of scaled Gaussians as discussed in section 3.2.1). The EM algorithm iteratively alternates between two steps:

(1) In the expectation (E)-step, the product of the conditional expectations of the two latent variables $\mathbb{Z} = \{z_{kij}\}$ and $\mathbb{U} = \{u_{kij}\}$, are computed given an estimate of the unknown parameters Ψ. This results in a corrected set of posterior probabilities $P_{kij}^{\star}$ (as shown in equation 3.9b), which represent robust correspondence probabilities between points on each shape and the mixture centroids. These are subsequently employed in the M-step to update estimates for the unknown parameters Ψ. On the $(t+1)^{\text{th}}$ EM-iteration, the expectations of the latent variables are computed as follows:

$$E_{\Psi^{(t)}}(z_{kij}|\mathbf{x}_{ki}) = P_{kij}^{(t)} = \frac{\pi_j\mathcal{S}(\mathbf{x}_{ki}|\mathbf{T}_k\boldsymbol{\mu}_j, \sigma^2, \nu_j)}{\sum_{j=1}^{M}\pi_j\mathcal{S}(\mathbf{x}_{ki}|\mathbf{T}_k\boldsymbol{\mu}_j, \sigma^2, \nu_j)} \tag{3.9a}$$

$$E_{\Psi^{(t)}}(u_{kij}|\mathbf{x}_{ki}, z_{kij} = 1) = U_{kij}^{(t)} = \frac{\nu_j + D}{\nu_j + \Delta_{kij}^2} \tag{3.9b}$$

$$E_{\Psi^{(t)}}(z_{kij}|\mathbf{x}_{ki})E_{\Psi^{(t)}}(u_{kij}|\mathbf{x}_{ki}, z_{kij} = 1) = P_{kij}^{\star(t)} = P_{kij}^{(t)}U_{kij}^{(t)} \tag{3.9c}$$

Δ_{kij}^2 is the squared Mahalanobis distance, defined previously in equation 3.1c.

(2) The maximisation (M)-step involves estimation of the model and transformation parameters by maximising Q (refer to equation 3.8b) with respect to each

unknown parameter, sequentially. Expressions for updating all parameters except ν_j are derived analytically (shown in equations 3.10 - 3.16). Differentiating Q with respect to ν_j results in a non-linear equation that is solved using an iterative root finding technique such as Newton's method, for each component in the mixture.

$$\boldsymbol{\mu}_j^{(t+1)} = \frac{\sum_{k=1}^{K}\sum_{i=1}^{N_k} P_{kij}^{\star(t)}(s_k^{-1(t+1)}\mathbf{R}_k^{T(t+1)}(\mathbf{x}_k - \mathbf{t}_k^{(t+1)}))}{\sum_{k=1}^{K}\sum_{i=1}^{N_k} P_{kij}^{\star}} \tag{3.10}$$

$$\sigma_{(t+1)}^2 = \frac{1}{ND}\sum_{k=1}^{K}\sum_{i=1}^{N_k}\sum_{j=1}^{M} P_{kij}^{\star(t)}\|\mathbf{x}_{ki} - s_k^{(t+1)}\mathbf{R}_k^{(t+1)}\boldsymbol{\mu}_j - \mathbf{t}_k^{(t+1)}\|^2 \tag{3.11}$$

In equations (3.11,3.13), $N = \sum_{k=1}^{K}\sum_{i=1}^{N_k}\sum_{j=1}^{M} P_{kij}$ is the total number of data points in the training set. From an implementation point of view it is important to note, in equations (3.10,3.11), $\boldsymbol{\mu}_j^{(t+1)}$ and $\sigma_{(t+1)}^2$ are updated using current estimates for the transformation parameters, i.e. $\mathbf{T}_k^{t+1}$, which are updated prior to the mixture model parameters Θ, at each EM-iteration. As there exists no closed-form expression to estimate $\nu_{j=1..M} = \Upsilon$, they are computed by solving equation 3.12 using Newton's method:

$$-\psi(\frac{\nu_j}{2}) + \ln(\frac{\nu_j}{2}) + 1 + \frac{\sum_{k=1}^{K}\sum_{i=1}^{N_k} P_{kij}^{(t)}(\ln(U_{kij}^{(t)}) - U_{kij}^{(t)})}{\sum_{k=1}^{K}\sum_{i=1}^{N_k} P_{kij}^{(t)}} + \psi(\frac{\nu_j^{(t)} + D}{2}) - \ln(\frac{\nu_j^{(t)} + D}{2}) = 0 \tag{3.12}$$

The maximum likelihood estimate for mixture coefficients π_j is given by:

$$\pi_j^{(t+1)} = \frac{\sum_{k=1}^{K}\sum_{i=1}^{N_k} P_{kij}^{(t)}}{N} \tag{3.13}$$

The transformation parameters for each shape in the training set are estimated as follows:

$$\texttt{Rotation} : \mathbf{R}_k^{(t+1)} = \mathbf{U}\mathbf{S}\mathbf{V}^T \tag{3.14}$$

$$\texttt{Scaling}: s_k^{(t+1)} = \frac{\text{tr}\{\sum_{i=1}^{N_k}\sum_{j=1}^{M} P_{kij}^{\star(t)}(\boldsymbol{\mu}_j - \mathbf{m}_k^{(t+1)})(\mathbf{x}_{ki} - \mathbf{d}_k^{(t+1)})^T\mathbf{R}_k\}}{\text{tr}\{\sum_{i=1}^{N_k}\sum_{j=1}^{M} P_{kij}^{\star(t)}(\boldsymbol{\mu}_j - \mathbf{m}_k^{(t+1)})(\boldsymbol{\mu}_j - \mathbf{m}_k^{(t+1)})^T\}} \tag{3.15}$$

$$\texttt{Translation}: \mathbf{t}_k^{(t+1)} = \mathbf{d}_k^{(t+1)} - s_k\mathbf{R}_k\mathbf{m}_k^{(t+1)} \tag{3.16}$$

In equation 3.14 **U**,**V** are unitary matrices estimated by singular value decomposition of matrix $\mathbf{C}_k$, computed as:

$$\mathbf{C}_k^{(t+1)} = \sum_{i=1}^{N_k}\sum_{j=1}^{M} P_{kij}^{\star(t)}(\mathbf{x}_{ki} - \mathbf{d}_k^{(t+1)})(\boldsymbol{\mu}_j - \mathbf{m}_k^{(t+1)})^T, \tag{3.17}$$

and **S** is a diagonal matrix given by, $\mathbf{S} = diag(1, 1, det(\mathbf{U}\mathbf{V}^T))$, used to enforce estimation of strictly orthogonal rotation matrices $\mathbf{R}_k$, whilst avoiding reflections (similar to (Gooya, Davatzikos, and Frangi, 2015)). In equations (3.15 - 3.17), $\mathbf{d}_k^{(t+1)}$ and $\mathbf{m}_k^{(t+1)}$ represent weighted centroids/barycenters expressed as shown in equations (3.18 - 3.19).

$$\mathbf{d}_k^{(t+1)} = \frac{\sum_{i=1}^{N_k}\sum_{j=1}^{M} P_{kij}^{\star(t)}\mathbf{x}_{ki}}{\sum_{i=1}^{N_k}\sum_{j=1}^{M} P_{kij}^{\star(t)}} \tag{3.18}$$

$$\mathbf{m}_k^{(t+1)} = \frac{\sum_{i=1}^{N_k}\sum_{j=1}^{M} P_{kij}^{\star(t)}\boldsymbol{\mu}_j}{\sum_{i=1}^{N_k}\sum_{j=1}^{M} P_{kij}^{\star(t)}} \tag{3.19}$$

Derivations for all parameters presented in equations (3.10 - 3.16) are included in Appendix A. The EM algorithm is summarised by the pseudo-code presented in Algorithm 1.

3.2.3.1 Multi-Resolution Group-wise Rigid Registration

Registration algorithms in general, often suffer from convergence to local minima, resulting in sub-optimal solutions. In image registration, this has been addressed previously by adopting a hierarchical multi-resolution registration approach that operates in a coarse-to-fine fashion and thereby reduces the chances of local minima entrapment (Rueckert et al., 1999). (Frangi et al., 2002) proposed

Algorithm 1 TMM

Inputs: Group of shapes $\mathbf{X}_{k=1..K}$, number of mixture components M, max.iterations
Outputs: Set of similarity transformations $\mathbf{T}_k$, aligned soft-correspondences, mean shape $\mathbf{M}$

INITIALIZATION
Initialize $\mathbf{M}, \sigma^2$ using K-means clustering, π_j = 1/M and $\nu_j = 3.0$
All π_j = 1/M and $\nu_j = 3.0$
procedure EM($\mathbf{X}_k, \mathbf{M}, \sigma^2, \Upsilon, \Pi, \mathbf{T}_k$) ▷ EM initialized
  while Iteration < max.iterations **do**
    Compute $P^{\star}_{kij} = P_{kij} U_{kij}$ ▷ E-step
    Update $\mathbf{R}_k, s_k, \mathbf{t}_k$ ▷ M-step
    Update $\mathbf{M}$, σ^2, Π and Υ ▷ M-step
  end while
  return $\mathbf{M}, \sigma^2, \Upsilon, \Pi, \mathbf{T}_k$
end procedure

a multi-resolution non-rigid B-spline registration framework for automatic landmarking (and correspondence estimation) of multi-object shape ensembles via an atlas-to-training-set registration strategy, for the purpose of training SSMs. Such an approach however, can be computationally expensive in the case of large data sets and requires construction of an unbiased atlas. A group-wise multi-resolution approach is novel in the context of point set registration and was proposed in our recent work (Ravikumar et al., 2016a), although, a similar approach (multi-scale EM-ICP) was proposed previously by (Granger and Pennec, 2002). The main differences between multi-scale EM-ICP and our method are — (a) the former is a pair-wise registration approach while mrTMM is group-wise. The latter consequently enables estimation of a mean shape, correspondences and transformations, in an unbiased manner; (b) multi-scale EM-ICP assumes uniform priors on the matches while mrTMM revises estimates for the mixture coefficients at each iteration; (c) in order to reject outliers, multi-scale EM-ICP chooses an ad-hoc threshold on the Mahalanobis distance and assigns a null weight for model points farther away, while no such threshold needs to be defined for mrTMM as it is inherently robust to outliers, due to its constituent heavy-tailed t-distributions; and (d) in multi-scale EM-ICP the 'scene' point set is decimated at each scale (or variance) and the latter is reduced with each iteration using an annealing scheme. With mrTMM the 'scene' point sets are left untouched and the mean model's density is increased adaptively at each successive resolution. While the former may be suitable for pair-wise registration applications, it could lead to over-fitting of

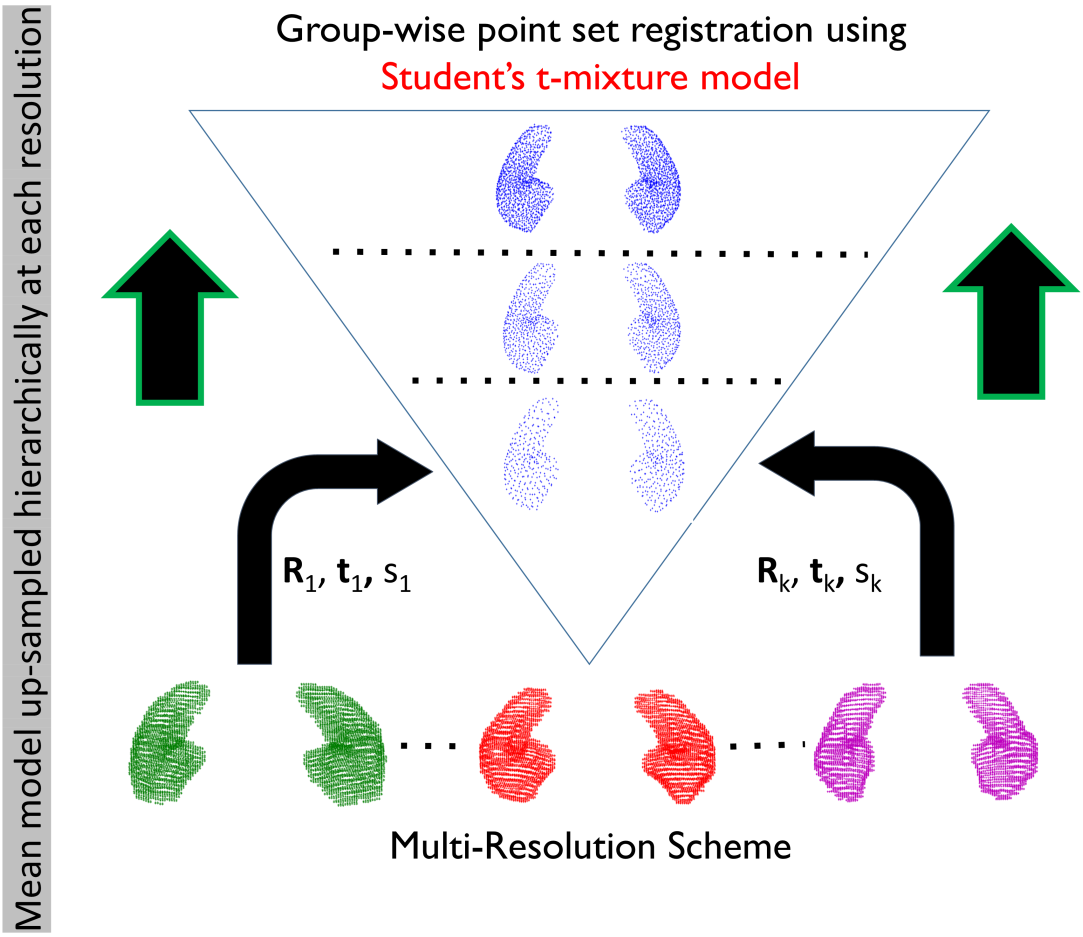

FIGURE 3.2: Schematic describes the registration process using mrTMM. The inverted triangle represents the hierarchical coarse-to-fine procedure used to up-sample the mean model (black points) at each resolution level. The mean model is iteratively aligned to the group of shapes (set of coloured points at the bottom), at each successive resolution.

the model in the context of group-wise registration, as the main benefit of the approach arises from starting at a high scale, leading to substantial decimation of the 'scene' point set. Additionally, such an approach would reduce the degree of shape variability captured by the SSMs trained following registration (the main application of interest in this study). Consequently, mrTMM is more suitable for our application.

By embedding the TMM-based registration framework within a multi-resolution scheme (abbreviated as mrTMM), the influence of local minima during registration is reduced. mrTMM begins with a low density mean model (i.e. few

mixture components) which is iteratively refined and upsampled at each successive resolution, through a process of 'adaptive sampling' from the mixture components. The transformations computed at each level are used to initialize the subsequent resolution and the overall model variance is decreased at each successive level by populating the mean model with new points. This reduction in model variance at each successive resolution refines the estimated transformations and improves registration accuracy. 'Adaptive sampling' to increase mean model density is achieved by imposing a multinomial distribution over the estimated mixture coefficients π_j and generating random samples S from those t-components in the mixture model that have a high probability in explaining the observed data, i.e. s^n new model points are sampled from the j^{th} mixture component, subject to the constraints $\sum_{j=1}^{M} s_j^n = S$ and $\sum_{j=1}^{M} \pi_j = 1$. S is a user-specified parameter and in this study we fixed $S^r = M^{r-1}$, where r represents the current resolution level, for all experiments (i.e. M is doubled at each successive resolution). The number of new model points sampled from each mixture component is described by equation 3.20a. Random samples are drawn from a zero-centered Gaussian distribution and an inverse χ^2-distribution with ν_j degrees of freedom, to generate new model points. This is because t-distributed random variables can conveniently be expressed as shown in equation 3.20b, where $\boldsymbol{\mu}_j^n$ represents the n^{th} model point sampled from $\boldsymbol{\mu}_j$, the centroid of the j^{th} mixture component.

$$p(s_j^n|\pi_j, S) = \frac{S!}{\prod_{n=1}^{S} s_j^n!} \prod_{j=1}^{M} \pi_j \tag{3.20a}$$

$$\boldsymbol{\mu}_j^n = \boldsymbol{\mu}_j + \mathcal{N}(0, \sigma^2)\sqrt{\frac{\nu_j}{\chi^2(\nu_j)}} \tag{3.20b}$$

Such a multi-resolution approach reduces the influence of local minima on the registration process, which may be introduced during model initialisation by k-means clustering (or similar processes) or during estimation of the model parameters. The mrTMM framework is further described by Algorithm 2. The schematic shown in Fig. 3.2 helps illustrate the up-sampling process, used to increase the density of the mean model at each resolution level.

Algorithm 2 mrTMM

`Inputs:` Group of shapes $\mathbf{X}_{k=1..K}$, number of mixture components M, max.resolutions, max.iterations
`Outputs:` Set of similarity transformations $\mathbf{T}_k$, aligned soft-correspondences, mean shape $\mathbf{M}$

INITIALIZATION
Initialize $\mathbf{M}, \sigma^2$ using K-means clustering, $\pi_j = 1/\mathrm{M}$ and $\nu_j = 3.0$
procedure EM($\mathbf{X}_k, \mathbf{M}, \sigma^2, \Upsilon, \Pi, \mathbf{T}_k$) ▷ EM initialized
  while Resolution < max.resolutions **do**
    while Iteration < max.iterations **do**
      Compute $P^{\star}_{kij} = P_{kij} U_{kij}$ ▷ E-step
      Update $\mathbf{R}_k, s_k, \mathbf{t}_k$ ▷ M-step
      Update $\mathbf{M}$, σ^2, Π and Υ ▷ M-step
    end while
    Compute s^n_j to be sampled from each μ_j
    Adaptively sample M new model points
    Re-initialize all $\pi^{new}_j = 1/M_{new}$ and $\nu^{new}_j = 3.0$, ν^{old}_j retained
    return $\mathbf{M}^{new}, \sigma^2_{old}, \Upsilon^{new}, \Pi^{new}, \mathbf{T}^{old}_k$
  end while
end procedure

3.2.4 Group-wise Non-Rigid Registration using Student's t-Mixture Model

The proposed TMM-based group-wise rigid registration framework (refer to section 3.2.3), is extended to group-wise non-rigid registration, referred to as TMM-NR. The non-rigid transformation is parametrised by Gaussian radial basis functions, and formulated similarly to CPD, based on Motion Coherence Theory (as discussed in section 3.2.2). As with group-wise rigid registration, the primary difference between pair-wise CPD and the proposed approach lies in the assumption that each shape in a group, is a transformed observation of the central mixture model. With CPD and pair-wise approaches in general, the target shape is typically considered to be a transformed observation of the 'moving' shape, i.e. the shape to be registered is considered to represent the centroids of a mixture model. A similar approach for pair-wise registration of shapes using TMMs was proposed previously, by (Zhou et al., 2014).

In the proposed approach the desired non-rigid transformations are defined with respect to the mean model $\mathbf{M}$ as: $\mathbf{M} + v^k(\mathbf{M})$, where v is a displacement function mapping the template to the k^{th} sample in the group. Here the mean model is defined by the centroids of the central TMM, as with its group-wise rigid counterpart. Consequently, to ensure the mean model is unbiased and representative of the group of shapes of interest, group-wise non-rigid registration using TMMs is always initialised by its group-wise rigid counterpart. This aids in recovering global differences in pose across shapes and also serves to initialise the centroids $\mu_j = \mathbf{M}$ and degrees of freedom ν_j of the TMM. This also helps minimise the chances of local minima entrapment, during non-rigid registration. As highlighted previously, in (Myronenko and Song, 2010) the authors show that by regularizing the norm of v, a smoothness constraint is enforced on the displacement field, which forces points in close proximity, to move together. Regularization of this nature is akin to employing a prior on the displacement field of the form $p(v) = \exp^{-\frac{\lambda}{2}\phi(v)}$, where $\phi(v)$ represents the regularization term and λ controls the trade-off between registration accuracy and smoothness of the deformation field. The prior on the displacement field is incorporated into the TMM, resulting in a log-likelihood function expressed as equation 3.21a. Using variational calculus, (Myronenko and Song, 2010) show that the function v, which maximises the data likelihood, can be expressed as a linear combination of radial basis functions (refer to equation 3.21b). Consequently, to register the template to the k^{th} sample in each group, the likelihood function to be maximised with respect to the basis function weights $w_{kj} = \mathbf{W}_k$, is expressed as shown in equation 3.21c, $\mathbf{G}$ represents the Gaussian kernel/Gram matrix. The gram matrix is $M \times M$ in size, with elements: $G(\boldsymbol{\mu}_l, \boldsymbol{\mu}_m) = \exp^{-||\frac{\boldsymbol{\mu_l} - \boldsymbol{\mu_m}}{2\beta}||^2}$. Here β represents the width of the Gaussian kernel, which regulates the frequencies filtered out when fitting to data (as the Gaussian kernel acts as a low-pass filter) and consequently, controls the smoothness of the resulting deformation field. As defined previously in section 3.2.3, Θ represents the set of all mixture model parameters. The basis function weights to register the mean template to each sample in a patient group, are estimated similarly to (Myronenko and Song, 2010).

$$\ln p(\mathbb{X}|\Theta) = \sum_{k=1}^{K}\sum_{i=1}^{N_k} \ln \sum_{j=1}^{M} \pi_j \mathcal{S}(\mathbf{x}_{ki}|v^k(\boldsymbol{\mu}_j), \sigma^2, \nu_j) + \frac{\lambda}{2}\phi(v^k) \tag{3.21a}$$

$$v^k(\mathbf{q}) = \sum_{j=1}^{M} w_{kj} G(\mathbf{q} - \boldsymbol{\mu}_j) \tag{3.21b}$$

$$Q(\Theta^{t+1}, \mathbf{W}_k^{t+1}|\Theta^t, \mathbf{W}_k^t) = -\frac{1}{2\sigma_p^2}\sum_i^{N_k}\sum_j^{M} P_{kij}^{\star t}\|\mathbf{x}_{ki} - (\boldsymbol{\mu}_j + v^k(\boldsymbol{\mu}_j))\|^2 + \frac{\lambda}{2}\mathbf{W}_k^T\mathbf{G}\mathbf{W}_k \tag{3.21c}$$

3.3 Results and Discussion

The methods proposed in this chapter, namely, rigid and non-rigid variants of TMM and mrTMM, are validated using both synthetic and clinical data. The rigid versions are compared with four state-of-the-art rigid point set registration methods: rigid-CPD, SpSSM, JRMPC and a group-wise GMM-based method (denoted GMM) similar to EM-ICP proposed by (Hufnagel et al., 2008). Our implementation of GMM, however, explicitly estimates the variance of the mixture model at each iteration as the registration progresses, while EM-ICP heuristically decreases the same with each successive iteration. The difference between GMM and SpSSM lies in the estimation of the mixture coefficients. The former employs classical maximum likelihood estimation, while the latter, uses a conjugate prior and opts for Bayesian estimation. The original pair-wise, rigid CPD algorithm (Myronenko and Song, 2010) is used for comparison with the synthetic data as instances in the group are transformed and modified versions of the raw Stanford bunny point set. For the clinical data however, we opt for a group-wise version of CPD to enable direct comparison with the other methods. The non-rigid TMM and mrTMM algorithms are compared with non-rigid CPD alone, as it was shown to outperform various other point set registration techniques in (Myronenko and Song, 2010) and has been widely employed in a variety of medical image analysis applications.

The synthetic data set was generated using the 3D Stanford bunny point set [2]. It comprises of the original point set and three modified and transformed copies, generated as follows: (1) original bunny point set was cropped along the xy-, yz- and xz-planes to generate three distinct samples with missing information at different spatial locations (depicted in Fig. 3.3(b-d)), (2) rigid transformations (i.e. only translation and rotation) were subsequently applied to the cropped samples and (3) all four point sets were finally corrupted by the addition of uniformly distributed outliers and Gaussian noise to varying degrees. Table 1 describes the degree of noise and outliers applied to each sample in both synthetic data sets

[2]The Stanford 3D scanning repository.
Available at: http://graphics.stanford.edu/data/3Dscanrep/

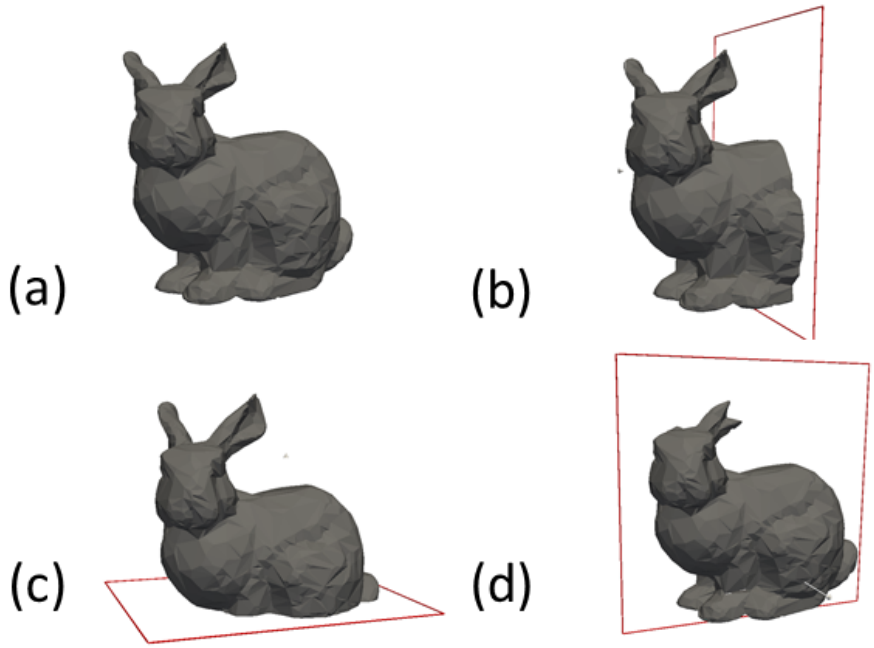

FIGURE 3.3: 3D bunny data set: (a) decimated original surface mesh; sample (a) cropped along: (b) yz-plane, (c) xz-plane and (d) xy-plane.

and their corresponding ground truth transformations. The resulting data sets are depicted in Fig. 3.4. The synthetic data were generated in this manner to evaluate the ability of the proposed methods to accurately align shapes in the presence of: (1) large rotational offsets with minimal overlap between samples, (2) missing information and (3) varying degrees of outliers.

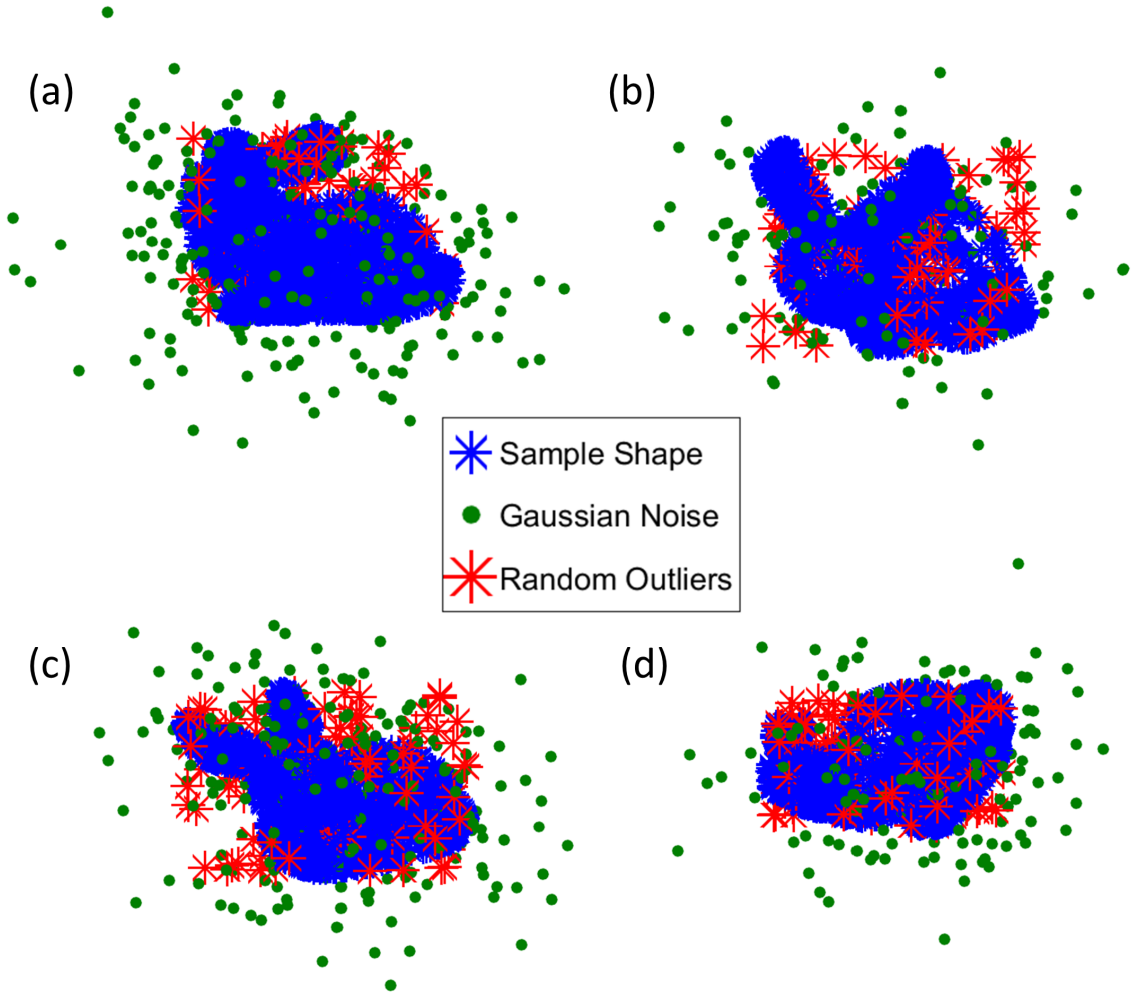

FIGURE 3.4: Transformed bunny data set comprising four samples (black). Samples (b-d) generated by rigidly transforming sample (a). All samples corrupted by varying proportions of Gaussian noise (green) and uniformly-distributed outliers (red).

TABLE 3.1: Rigid transformations and degree of outliers used to generate bunny data set.

Sample	N_k	$\mathbf{R}_k^g$	$\mathbf{t}_k^g$ (cm)	**Gaussian noise**(%)	**Random outliers**(%)
1	2420	-	-	13	2.50
2	1883	x: 64°, y: 22.50°	x: 0.20, y: -0.30, z: 0.50	9	4
3	1889	y: 50°, z: 20°	x: -0.25, y: 0.35, z: -0.15	14	6
4	1658	z: 60°, x: 18°	x: -0.10, y: -0.50, z: 0.40	11	5

Four clinical data sets were also used to validate the proposed rigid registration methods: (a) `Femur`: 2D set of (K =1000) femoral heads segmented automatically from dual energy X-ray absorptiometry (DXA) images (depicted in Fig. 3.5), using Hologic Apex 3.2, a software frequently employed in the clinic. DXA images and their segmentations were acquired in a previous study (McCloskey et al., 2007); (b) `Hippocampus_Ctrl`: 3D set of hippocampi segmented automatically from T1-weighted magnetic resonance (MR) images of healthy subjects (K =50); (c) `Hippocampus_MCI`: 3D set as for (b), but acquired from patients diagnosed with MCI (K =28) (examples shown in Fig. 3.6). For (b) and (c), MR images were acquired as part of the VPH-DARE@IT project[3] and the automatic segmentation tool based on shape-constrained deformable models, was provided by Philips Research Laboratories, Hamburg, Germany (Zagorchev et al., 2016); and (d) `Heart`: 3D set of hearts comprising the epicardium and endocardium for both left and right ventricles (K =30). Training segmentations for the heart were generated from short-axis MR images of healthy subjects (K =10), patients diagnosed with pulmonary hypertension (PH, K =10) and patients diagnosed with hypertrophic cardiomyopathy (HCM, K =10), as part of a previous study (Albà et al., 2014). With (d), samples from all three diagnostic groups were pooled into a single data set and used to validate the proposed methods. This strategy is adopted for the heart data set to assess the ability of the proposed methods

[3]http://www.vph-dare.eu/

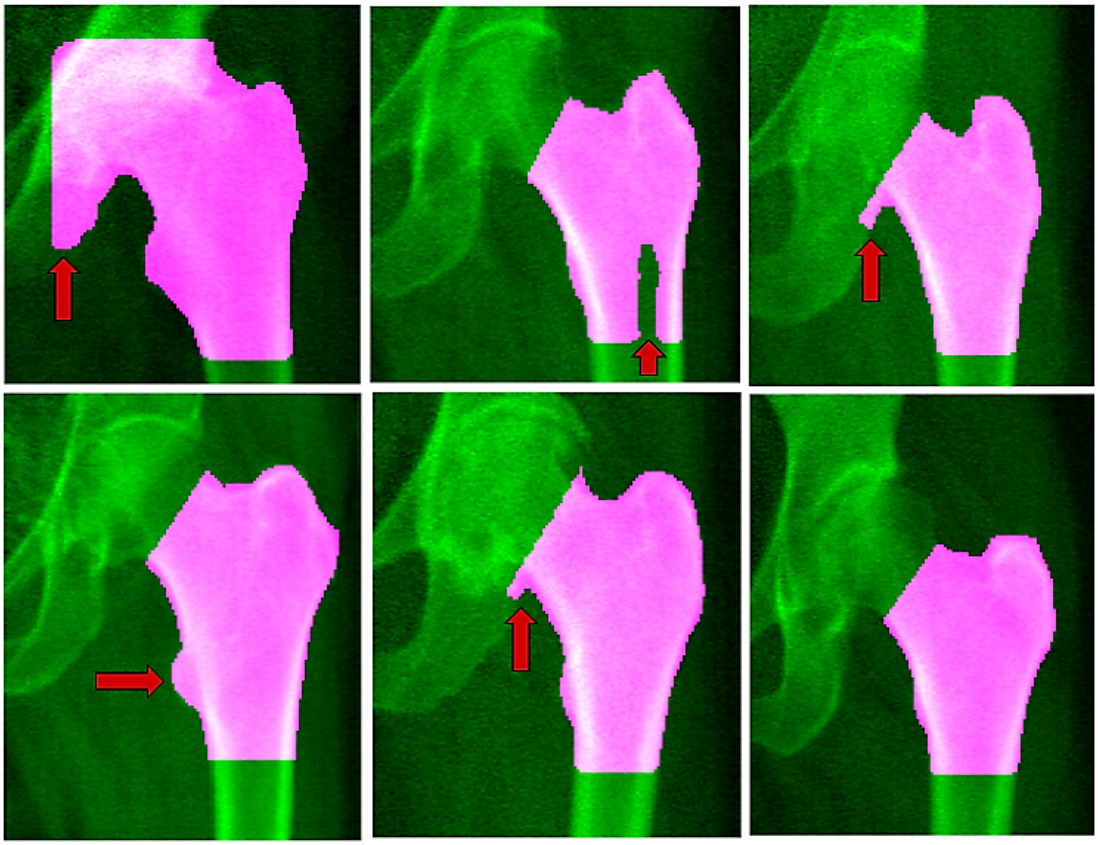

FIGURE 3.5: Raw DXA images from the femur data set overlaid with their respective boundary masks. Red arrows indicate regions with over- or under-segmented boundaries, which result in point sets with varying degrees of outliers.

to accurately align and generate high quality SSMs in the presence of significant pathology-induced variations in geometry across training shapes. Additionally, the heart comprising both ventricles and the endo-/epi-cardium is used for validation due to its topological complexity (i.e. not homeomorphic to a sphere), to illustrate the independence of the proposed framework to topology. Shapes derived from various clinical domains are used to validate the proposed methods, to highlight the general and flexible nature of the probabilistic framework. Comparisons are made with the state-of-the-art in terms of rigid registration accuracy for both synthetic and clinical data.

The publicly available synthetic 3D face data set (provided as part of the CPD package, available at: https://sites.google.com/site/myronenko/research/cpd), devoid of any synthetic outliers, is employed initially to assess non-rigid registration accuracy of the proposed TMM-based method. This data set comprises a ground truth face point set and 50 deformed versions of the

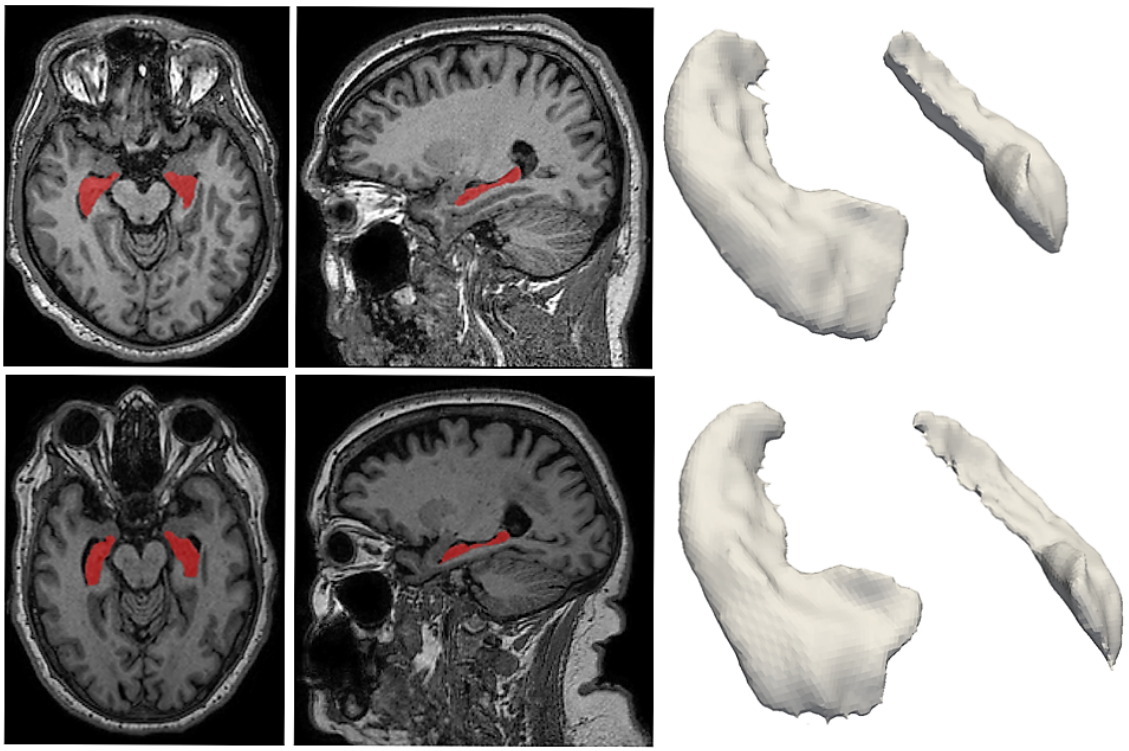

FIGURE 3.6: Hippocampi automatically segmented from MR images of a healthy subject (top row) and MCI patient (bottom row). Axial and saggital view of segmentations overlaid on their respective raw images are shown in the left and centre columns respectively and the surfaces generated from these are depicted in the column on the right.

same. The former is non-rigidly registered to each deformed instance using the proposed approach, the original pair-wise non-rigid CPD algorithm and a group-wise variant of the CPD algorithm (gCPD). Hausdorff distance (HD) and mean surface distance (MSD) measures are evaluated following registration, between the registered and the original deformed face point sets, and used to compare the proposed approach with the two variants of the non-rigid CPD algorithm.

One clinical data set, comprising complex geometries is also used to compare the registration accuracy of TMM-NR, with non-rigid gCPD. 27 brain ventricular geometries containing — lateral ventricles, third ventricle, cerebral aqueduct and fourth ventricle; segmented from T1-weighted MRIs of 9 `AD`, 9 `MCI` and 9 healthy `Control` subjects constitute the clinical data set employed. The body of the lateral ventricles and the third ventricle were segmented similarly to the hippocampi data sets (discussed previously), using the approach proposed in (Zagorchev et al., 2016). The cerebral aqueduct and fourth ventricle meanwhile, were segmented using a multi-atlas label propagation approach. Segmentations

resulting from each approach was combined and point sets were automatically extracted from these, using a marching cubes-based algorithm. Accurate group-wise registration of the ventricles data set is very challenging as the samples exhibit a very high degree of variability in geometry across samples. This is in part due to significant enlargement of the lateral ventricles in `AD` and `MCI` patients, relative to `Control` subjects, as a consequence of tissue atrophy in the surrounding grey and white matter. It is important to note that, the clinical data sets were co-registered using group-wise (non-rigid) CPD and compared with TMM-NR, rather than its pair-wise counterpart. This is because, the high degree of variability in the clinical data sets, makes it difficult to choose one of the constituent samples as the template (or 'moving' point set), without significantly biasing the results of subsequent registrations. Initial group-wise rigid registration offers a solution to this issue, by first estimating a mean template, representative of the shapes in each data set, whilst jointly correcting any differences in pose between the samples. The estimated mean template is subsequently employed for group-wise non-rigid registration, and deformed to match each sample in a group, whilst simultaneously being revised itself (as done in the rigid registration step). This process is followed using both methods, namely, group-wise CPD and TMM-NR. The registration accuracy of these are subsequently compared using the HD and MSD metrics, evaluated between the deformed templates and the ground truth shapes.

3.3.1 Rigid Registration Accuracy

As ground truth transformations were available for the synthetic data set, registration accuracy was assessed by evaluating the root-mean-squared-error (RMSE) (similar to (Evangelidis et al., 2014)) of the estimated rotation matrices, relative to the ground truth rotations. RMSE was computed as described by equation 3.22a, where $||\cdot||_F$ denotes the Frobenius norm and $\mathbf{R}_k^g$ and $\mathbf{R}_k$ represent the ground truth rotation applied to the k^{th} sample in the group and the corresponding rotation matrix estimated for the sample, respectively. As the synthetic data set is generated by rigidly transforming the bunny point set (denoted sample 1, refer to Table 1), the estimated rotations for the remaining samples (relative to the mean) are transformed to the coordinate frame of sample 1 to enable direct comparison with their corresponding ground truths. This is achieved by computing the product of $\mathbf{R}_{k=2,3,4}$ and the inverse of the rotation estimated for sample 1,

denoted $\mathbf{R}_1^T$ in equation 3.22a. Additionally, the intrinsic distance between the estimated and ground truth rotations (Huynh, 2009) were also evaluated as shown in equation 3.22b, for easier interpretation of the rotation errors (θ_{err}), in terms radians/degrees.

$$RMSE = ||\mathbf{R}_k^g - \mathbf{R}_k\mathbf{R}_1^T||_F \tag{3.22a}$$

$$\theta_{err} = \arccos\left[\frac{\mathrm{tr}((\mathbf{R}_k^g(\mathbf{R}_k\mathbf{R}_1^T)^T) - 1}{2}\right] \tag{3.22b}$$

Registration accuracy was also evaluated for all four clinical data sets, using the HD and MSD metrics. These measures were evaluated as shown in equations 3.23a - 3.23b, where $\mathbf{d_{min}}(A, B)$ denotes the minimum distance for each point in shape A to shape B. HD and MSD measures were computed between the aligned soft-correspondences estimated for each sample in the group and the corresponding mean shape estimated for the group. Alignment accuracy was evaluated in this manner because — (a) registration errors evaluated between the estimated soft correspondences and the original point sets would be difficult to interpret for data containing substantial outliers (as in the case of the femur data set), as the proposed methods would be robust to such outliers, thereby resulting in high HD and MSD values, which would not reflect the improvement in registration quality achieved (relative to the state-of-the-art); (b) the aim of these experiments was to assess the ability of the proposed methods to rigidly align a group of shapes, in a manner robust to the presence of noise and outliers. Consequently, HD and MSD measures evaluated between the soft correspondences (established for each shape) and the mean shape estimated for each group, reflect the ability of the proposed methods to accurately align a group of shapes to a common reference frame; (c) these experiments were designed to complement subsequent ones evaluating SSM quality (refer to **chapter** 4), for SSMs trained using the estimated soft correspondences, i.e. both sets of experiments evaluating rigid alignment accuracy and SSM quality, together reflect the quality of registration achieved using the proposed approaches. For the data set of hippocampi, alignments were performed independently for the healthy and MCI samples and consequently, registration accuracy was evaluated separately for the two hippocampi groups.

$$HD = max(max(\mathbf{d_{min}}(A, B)), max(\mathbf{d_{min}}(B, A))) \tag{3.23a}$$

$$MSD = mean(mean(\mathbf{d_{min}}(A, B)), mean(\mathbf{d_{min}}(B, A))) \tag{3.23b}$$

3.3.1.1 Synthetic data

Table 3.2 summarizes the alignment accuracy of each method investigated, for the synthetic data. The RMSE values for each transformed sample (i.e. samples (b-d) in Fig. 3.4) indicate that the proposed methods, TMM and mrTMM, achieve significantly lower registration errors than CPD, SpSSM and GMM across all three samples. Although JRMPC shows good robustness and achieves marginally lower errors for samples 3 and 4 (relative to TMM and mrTMM), it is unable to recover the rotation for sample 2 and results in significantly higher errors. The number of model points (user-specified parameter) was set to 940, which is 50% of the median cardinality of the synthetic data set, for each group-wise registration method investigated. In the case of CPD, a pair-wise approach, this is determined by the number of points used to represent the 'moving' point set. As outlined previously in section 3.1, JRMPC and CPD require a user-specified parameter that controls the weight of the uniform distribution component in the mixture model and consequently the degree of robustness of the model to noise and outliers. Values in the range of $(0.1 - 0.9)$ were tested and the value returning the lowest registration errors (reported in Table 3.2) was considered optimal for the data set. Mean RMSE errors are computed across samples and used to compare each registration method (using a paired sampled t-test, considering a significance level of 5%). TMM and mrTMM achieve significantly lower errors, highlighted in bold in Table 3.2.

TABLE 3.2: RMSE values computed between estimated and ground truth rotations for 3D bunny data set.

Method	Sample 2	Sample 3	Sample 4	Mean RMSE
CPD	0.1781	0.1021	0.1841	0.1548 ± 0.05
SpSSM	1.5133	0.0944	0.0700	0.5592 ± 0.83
GMM	1.2156	0.8260	1.2786	1.1067 ± 0.24
JRMPC	1.8541	0.0022	0.0011	0.6191 ± 1.07
TMM	0.0232	0.0260	0.0287	$\mathbf{0.026 \pm 0.003}$
mrTMM	0.0012	0.0031	0.0016	$\mathbf{0.002 \pm 0.001}$

The RMSE values presented in Table 3.2 and the intrinsic rotation errors in Table 3.3 indicate that SpSSM and JRMPC are able to recover the applied rotations to

TABLE 3.3: Intrinsic rotation errors evaluated in terms of radians (Rad.) and degrees (Deg.) between estimated and ground truth rotations.

Method	**Sample 2**		**Sample 3**		**Sample 4**		**Mean Error**	
	Rad.	Deg.	Rad.	Deg.	Rad.	Deg.	Rad.	Deg.
CPD	0.128	7.327	0.072	4.139	0.155	8.886	0.118 ± 0.04	6.784 ± 2.42
SpSSM	1.129	64.69	0.067	3.824	0.049	2.838	0.415 ± 0.62	23.78 ± 35.43
GMM	0.903	51.74	0.623	35.70	0.943	54.05	0.823 ± 0.17	47.16 ± 9.99
JRMPC	1.5103	86.53	5×10^{-4}	0.029	0.002	0.134	0.50 ± 0.87	28.90 ± 49.91
TMM	0.015	0.838	0.015	0.887	0.019	1.107	**0.016 ± 0.002**	**0.944 ± 0.14**
mrTMM	0.001	0.06	0.0024	0.139	0.001	0.066	**0.001 ± 5.8×10^{-4}**	**0.09 ± 0.04**

a high degree of accuracy for samples 3 and 4, but fail to do so for sample 2. This may be attributed to the smaller capture range of group-wise GMM-based methods for this synthetic data set, in comparison to CPD and the proposed TMM-based methods. Additionally, the failure of group-wise GMM-based methods to recover the rotation applied to sample 2 may be due to the high degree of rotation ($> 60°$) applied about the x-axis. CPD is able to recover synthetic rotations to a moderate degree of accuracy and shows good robustness to noise and outliers. It is interesting to note that JRMPC was shown to outperform CPD in (Evangelidis et al., 2014) when the applied synthetic rotations were of lower magnitude (maximum of $30°$). This supports our observation that although JRMPC shows good robustness to noise and outliers, it lacks the ability to recover large rotational offsets. This hypothesis was further validated by conducting an additional experiment using the bunny data set where the cropped samples (refer to Fig. 3.3(b-d)) were rotated to larger degrees, without the inclusion of synthetic noise and outliers. The proposed methods were able to recover rotations in the range

of $[-60°, 60°]$, applied along multiple axes, while CPD and JRMPC failed to do so. This is visually described and verified by the images shown in Fig. 3.7.

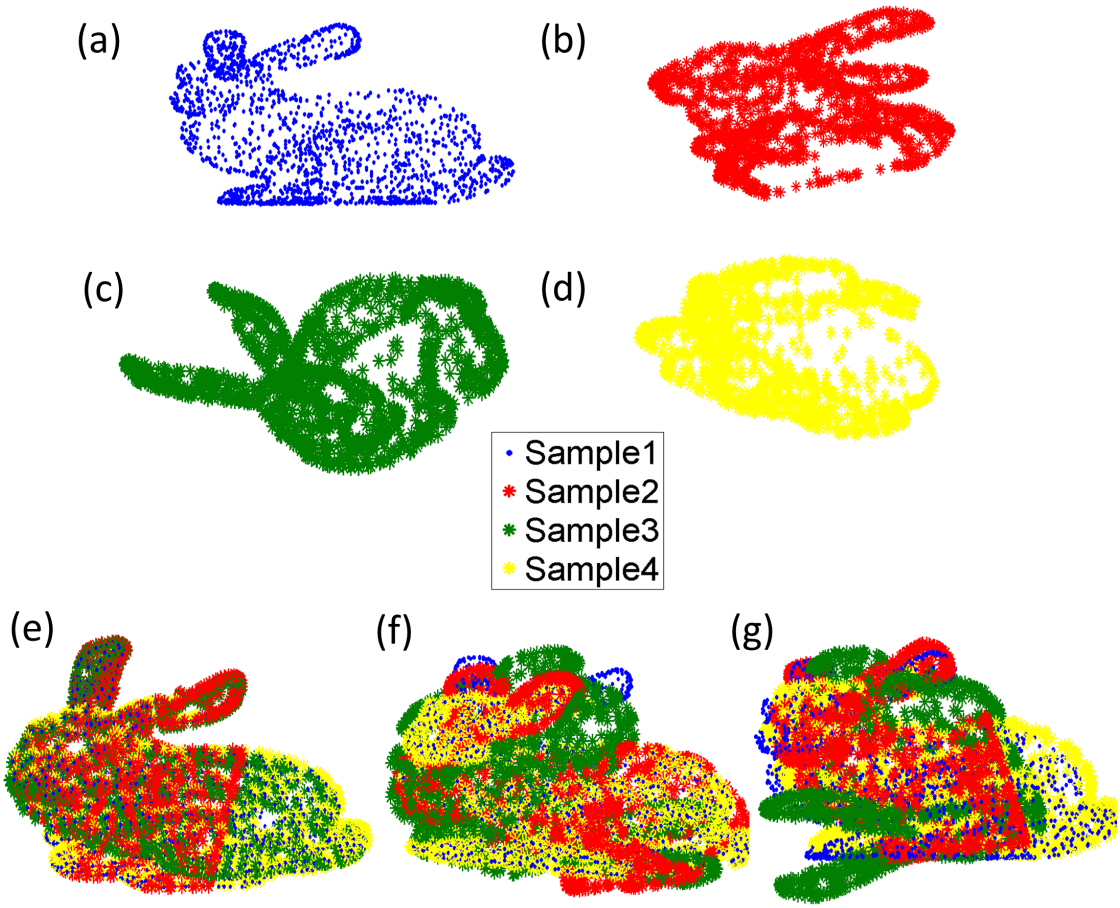

FIGURE 3.7: Experiment investigating capture range of registration methods. Sample (a) original bunny point set, (b) point set in (a) rotated by $60°$ about x-axis and $-60°$ about y-axis, (c)point set in (a) rotated by $60°$ about y- and z-axes and (d) point set in (a), rotated by $-60°$ about z-axis and $60°$ about x-axis. (e) point sets aligned using mrTMM, (f) point sets after alignment using JRMPC and (g) point sets aligned using pair-wise CPD.

The proposed TMM-based methods offered substantial improvements over GMM-based approaches in the synthetic data experiments, as they are more robust to noise and outliers, have a wider capture range for recovering rotational offsets, do not require any prior knowledge of the degree of outliers present in the data and correspondingly, require fewer user-specified parameters than CPD and JRMPC. Rotation errors evaluated in terms of radians and degrees (Table 3.3) complement and are consistent with the RMSE values reported in Table 3.2.

The proposed methods achieved significantly lower angular errors, evaluated between the estimated and ground truth rotations, relative to the state of the art. Additionally, in the presence of significant outliers and large rotational offsets, mrTMM offers substantial improvement over TMM in this regard.

3.3.1.2 Clinical data

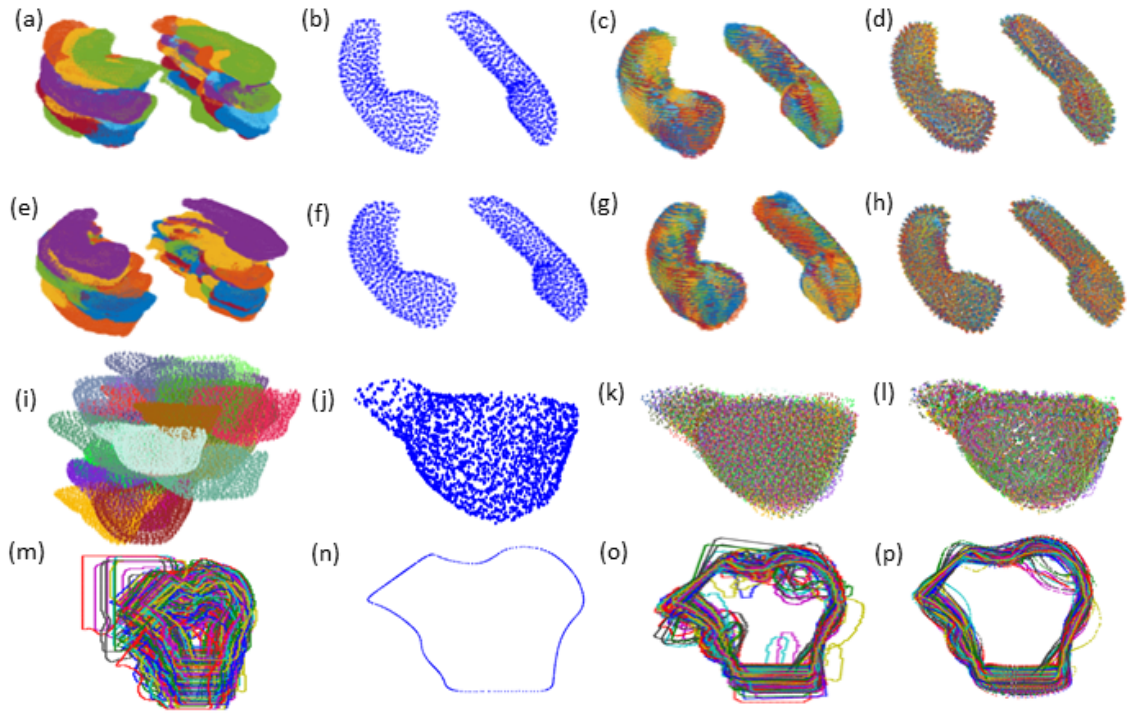

FIGURE 3.8: MCI-hippocampi (first row), healthy-hippocampi (second row), heart data set (third row) and femur data set (fourth row). First column: Raw point sets prior to alignment; second column: estimated mean shapes; third column: aligned shapes; and fourth column: aligned soft-correspondences (using mrTMM)

Registration accuracy of the proposed methods was also compared with the state of the art using clinical data. The raw point sets from each data set are shown in Fig. 3.8 (a,e,i,m). Fig. 3.8 (b,f,j,n) depict the mean shapes estimated for each group using mrTMM and Fig. 3.8 (c,g,k,o) and Fig. 3.8 (d,h,l,p) represent the corresponding aligned shapes and soft-correspondences, respectively, for each clinical data set. The significant level of outliers present in the femur data set is evident in Fig. 3.8 (m), while Fig. 3.8 (n) demonstrates the ability of mrTMM (similar result obtained for TMM as well) to estimate a valid mean shape in the presence of such outliers. Alignment errors were quantified using the HD and

MSD measures, presented in Table 3.4,3.5 for the hippocampi, Table 3.6 for the heart and Table 3.7 for the 2D-femur data sets (where M represents the number of mixture components used, for each method).

TABLE 3.4: Registration errors evaluated between the aligned soft correspondences and the mean shape estimated for MCI-hippocampi data set.

Method	M	`Hippocampus_MCI` ($K = 28$)	
		HD (mm)	**MSD (mm)**
gCPD	1280	**3.32 ± 1.17**	**0.61 ± 0.16**
SpSSM	1906	5.80 ± 1.11	0.80 ± 0.16
GMM	1280	5.60 ± 1.12	0.86 ± 0.20
TMM	1280	**3.39 ± 1.25**	**0.62 ± 0.17**
mrTMM	1280	**3.30 ± 1.32**	**0.58 ± 0.16**

TABLE 3.5: Registration errors evaluated between the aligned soft correspondences and the mean shape estimated for healthy-hippocampi data set.

Method	M	`Hippocampus_Ctrl` ($K = 50$)	
		HD (mm)	**MSD (mm)**
gCPD	1280	**3.38 ± 1.06**	**0.62 ± 0.13**
SpSSM	787	6.25 ± 1.32	0.94 ± 0.24
GMM	1280	7.56 ± 1.22	0.88 ± 0.22
TMM	1280	**3.26 ± 1.02**	**0.62 ± 0.14**
mrTMM	1280	**3.25 ± 1.10**	**0.61 ± 0.14**

TABLE 3.6: Registration errors evaluated between the aligned soft correspondences and the mean shape estimated for heart data set.

Method	M	`Heart` ($K = 30$)	
		HD (mm)	**MSD (mm)**
gCPD	2560	**17.51 ± 3.73**	**2.80 ± 0.66**
SpSSM	2191	32.41 ± 9.96	4.10 ± 1.09
GMM	2560	32.41 ± 10.32	4.07 ± 1.17
TMM	2560	**15.45 ± 3.96**	**2.80 ± 0.67**
mrTMM	1280	**15.74 ± 4.30**	**2.68 ± 0.62**

Statistical significance of the computed registration errors was assessed using a paired-sample t-test (considering a significance level of 5%). The proposed methods (TMM and mrTMM) and gCPD [4] were comparable in registration accuracy and outperformed SpSSM and GMM in experiments conducted using both hippocampi and heart data sets. Significant improvements in accuracy are highlighted in bold in Table 3.4 and 3.5 for the MCI and healthy groups, respectively. It should be noted however, gCPD requires an additional user-specified parameter (as with CPD), which controls the weight of the uniform distribution component in the mixture model and by extension the degree of robustness of the model to outliers. This parameter had to be tuned to identify the optimal value, based on registration accuracy. Weights of 0.7 and 0.3 were found to produce the lowest errors for MCI and healthy groups respectively, presented in Table 3.4 and 3.5. While for the heart data set, 0.5 was found to be optimal (errors presented in Table 3.6). However, for these data sets, sensitivity of the registration accuracy achieved by gCPD to the uniform distribution weights employed was modest, i.e. no significant change in registration errors were observed by varying the weights, as these data sets contained minimal noise/outliers. The proposed methods were equally robust, showing marginal improvements in some cases, required fewer user-specified parameters and consequently, are well suited for automation.

TABLE 3.7: Registration errors evaluated between the aligned soft correspondences and the mean shape estimated for femur data set.

Method	M	`Femur` ($K = 1000$)	
		HD (mm)	**MSD (mm)**
gCPD	1280	34.07 ± 2.98	2.56 ± 1.09
SpSSM	1474	77.43 ± 4.37	3.16 ± 1.07
GMM	1280	78.20 ± 4.29	3.31 ± 0.99
TMM	1280	$\mathbf{9.60 \pm 4.82}$	$\mathbf{2.23 \pm 0.90}$
mrTMM	1280	$\mathbf{10.04 \pm 5.33}$	$\mathbf{2.19 \pm 0.92}$

Although the HD values reported in Tables 3.4 and 3.5 seem large for the hippocampi, it is important to note that they were computed between the aligned correspondences estimated for each sample and the mean shape estimated for the corresponding patient group (i.e. MCI or healthy). Consequently, they reflect the natural variation in hippocampal size present across samples in both patient

[4] As mentioned previously, gCPD is employed in place of JRMPC as the latter does not recover global scaling across point sets.

groups. Furthermore, these are primarily concentrated at anterior and posterior ends of the hippocampi (and not in the central body).

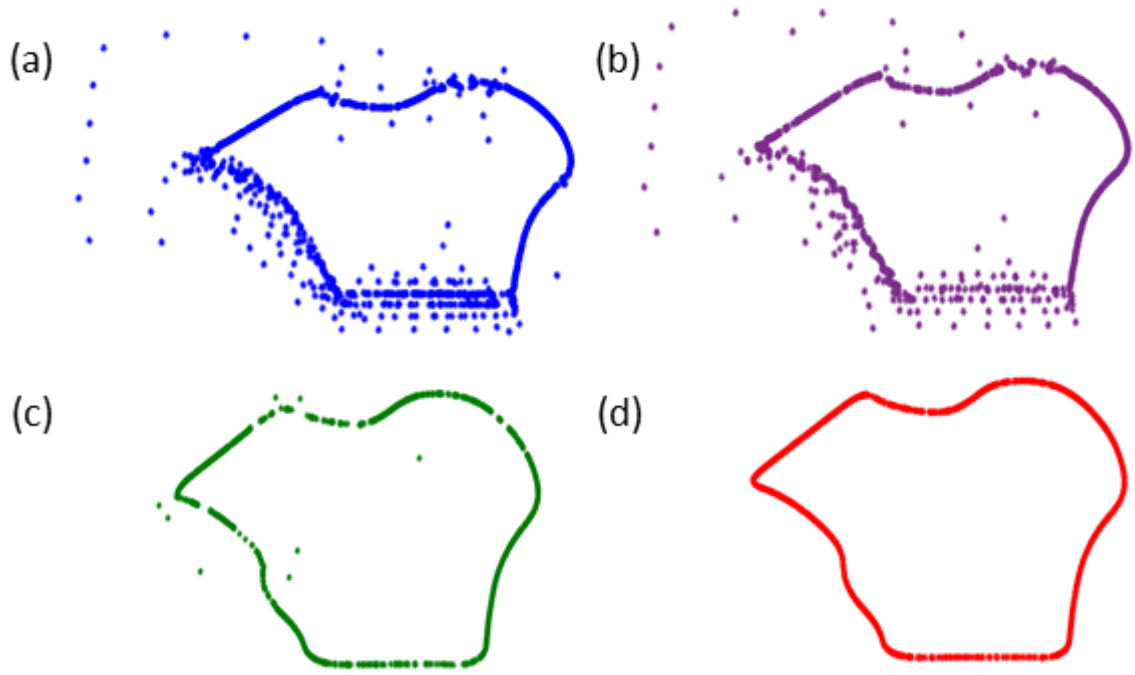

FIGURE 3.9: Mean femur shapes estimated using: (a) GMM, (b) SpSSM, (c) gCPD and (d) TMM.

However, with the femur data set, the proposed methods significantly outperformed all three GMM-based methods. This is attributed to the presence of significant levels of outliers in the femur shapes, which result in, the estimation of incorrect mean shapes (Fig. 3.9(a-c)), invalid correspondences, and consequently, the large registration errors observed. TMM and mrTMM, however, are robust to the presence of such outliers and are able to estimate valid mean shapes and correspondences (as shown in Fig. 3.9(d) and Fig. 3.8(n,p)), achieving significantly lower errors (summarized in Table 3.7), while requiring fewer user-specified parameters than gCPD. The change in registration accuracy achieved (using the femur data set) by gCPD for different values of the constituent uniform distribution weight, and thereby its sensitivity to the same, was evaluated and is summarised in Appendix C (Table C.1). These results indicate that for data sets containing a high degree of outliers, the performance of gCPD is sensitive to the weights chosen and thus requires tuning of the same for optimal results.

These experiments highlight the ability of the proposed approaches to remain robust to outliers and align groups of shapes to their respective mean shapes, more accurately than their GMM-based counterparts (namely, GMM and

SpSSM). They also complement subsequent experiments evaluating SSM quality (refer to **chapter** 4), which reflect the accuracy of the correspondences estimated for each sample within each group, using the proposed methods and the state-of-the-art, i.e. more accurate correspondences result in improved preservation of shape variation across a group and consequently more descriptive SSMs. Thus both sets of experiments (i.e. evaluation of alignment accuracy and SSM quality) together reflect the registration quality of the proposed methods, relative to the state-of-the-art.

3.3.2 Algorithm performance

3.3.2.1 Degrees of freedom

To quantitatively describe the influence of the degrees of freedom (ν) associated with TMM components on the robustness of the model to outliers, histograms depicting the range of values estimated for the synthetic and clinical data sets (following registration) are presented in Fig. 3.10 (a-d). For the synthetic data set that contains a large proportion of noise and outliers (refer to Fig. 3.4 and Table 3.1) and missing data, the values estimated are concentrated in the range $[2.1, 10]$ (as shown in Fig. 3.10 a), conferring a greater degree of robustness to the registration process. A similar result is obtained for the femur data set (Fig. 3.10 b) as it contains numerous samples with over-/under-segmented boundaries.

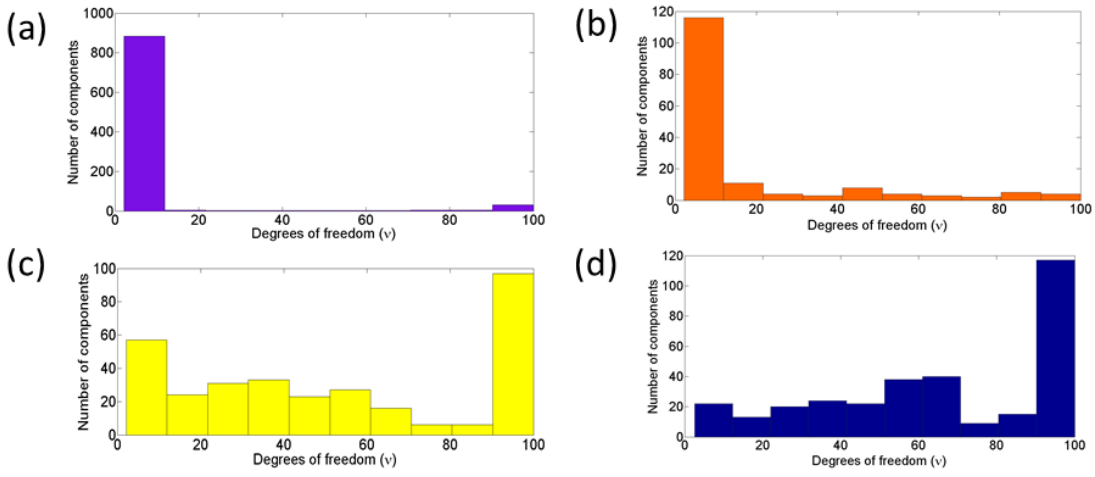

FIGURE 3.10: Histograms of the degrees of freedom estimated for; (a) the synthetic data set with noise and outliers (M=940), (b) femur data set (M=160), (c) heart data set (M=320) and (d) set of hippocampi from MCI patients (M=320), following alignment using mrTMM.

The heart and hippocampi data sets in contrast, contain few outliers and consequently, the values estimated for ν are distributed over a wider range, with high values indicating that the corresponding t-components behave similar to Gaussians (Heart: Fig. 3.10 c, MCI: Fig. 3.10 d). The flexible and robust nature of TMM-based registration is consequently attributed to the independent estimation of ν for each mixture component. Fig. 3.10 (c) indicates that although the heart data set contains few visibly apparent outliers, the significant variation in geometry across the group (as a result of pathology) results in the estimation of low ν values for a greater number of mixture components, relative to the MCI-hippocampi data set (containing few outliers and moderate variation in shape across the group). This illustrates the role of ν in accommodating large variations in shape, while ensuring robust and accurate registration.

3.3.2.2 Convergence

The convergence of the proposed algorithms (TMM and mrTMM) are assessed based on the change in the mean shape, computed as $dM = ||\mathcal{M}^{new} - \mathcal{M}^{old}||_F / ||\mathcal{M}^{old}||_F$, across EM-iterations. This is illustrated by Fig. 3.11, where dM is plotted against the number of iterations. dM was formulated in this manner in order to define a common critical threshold/tolerance (10^{-3} was used for all experiments) to assess convergence for all data sets, thereby improving automation (and removing the need for identifying a unique threshold specific to each data set). Alternative convergence criteria may also be adopted by monitoring the change in, the log-likelihood, model variance or the estimated transformations, across successive EM-iterations.

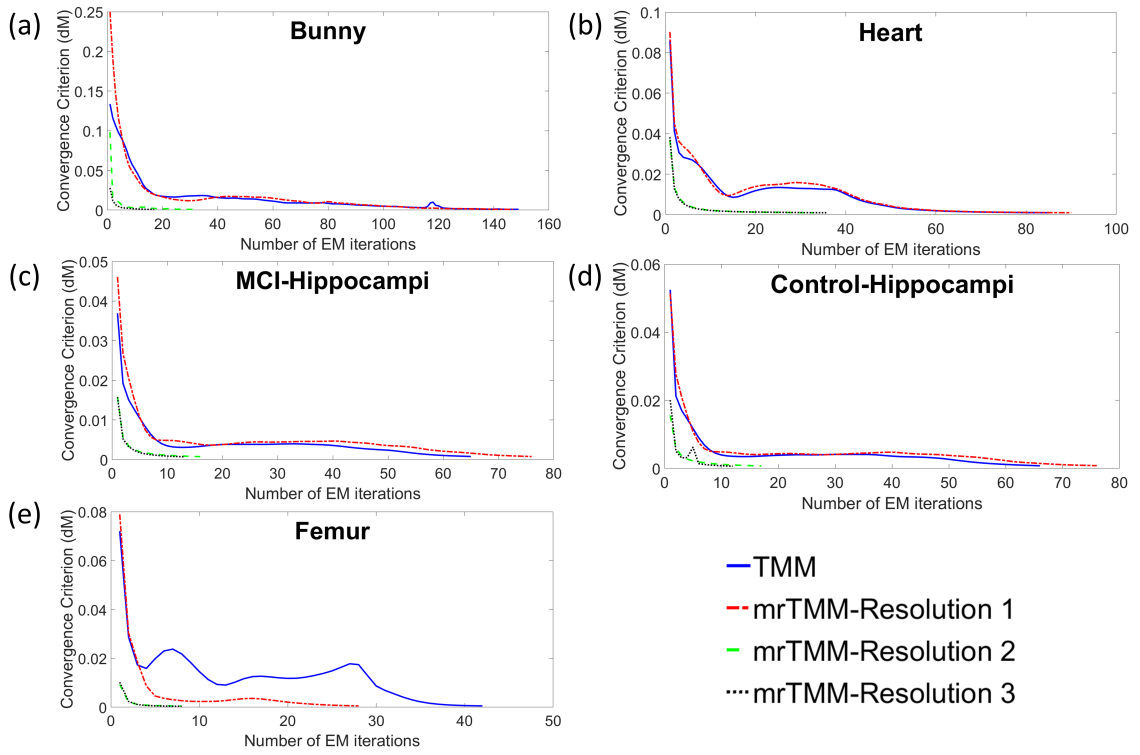

FIGURE 3.11: Convergence of TMM and mrTMM algorithms: (a) Synthetic bunny data set containing significant outliers (refer to Table 1), using $M = 940$ mixture components; (b) Heart data set, using $M = 2560$ mixture components; (c) MCI-hippocampi data set, using $M = 2560$ mixture components; (d) Control-hippocampi data set, using $M = 2560$ mixture components; and (e) Femur data set, using $M = 1280$ mixture components.

TABLE 3.8: Run-time (minutes) for each data set aligned using TMM and mrTMM with M mixture components.

Method	Bunny ($M = 940$) ($K = 4$)	Hippocampus_MCI ($M = 2560$) ($K = 28$)	Hippocampus_Ctrl ($M = 2560$) ($K = 50$)	Heart ($M = 2560$) ($K = 30$)	Femur ($M = 1280$) ($K = 1000$)
TMM	8	158	289	45	1471
mrTMM	5	95	167	30	320

In the case of mrTMM, convergence is assessed in this manner for each resolution level employed during registration. The plots depicted in Fig. 3.11 indicate that the convergence of TMM and the first resolution of mrTMM are similar to each other, for all data sets. Additionally, both TMM and mrTMM converge in fewer iterations for both hippocampi data sets (Fig. 3.11 (c,d)), relative to the remaining 3D data sets (Fig. 3.11 (a,b)). This is attributed to the presence of minimal outliers and moderate variation in shape across samples. Conversely, for the

synthetic bunny data set (Fig. 3.11 (a)), containing significant proportions of outliers and large rotational offsets, both TMM and the first resolution of mrTMM require more iterations to converge, relative to the clinical data sets. However, beyond the first resolution (with mrTMM), subsequent levels converge quicker as evidenced by Fig. 3.11, improving computational efficiency as fewer iterations are required at higher model complexities (or number of mixture components M). These results are further verified by the run-times reported in Table 3.8 for all data sets, following alignment using TMM and mrTMM. From this we infer that mrTMM consistently improves computational efficiency compared to TMM, as fewer EM-iterations are required using the same number of mixture components (M). The code was implemented in MATLAB (R2014a) and tested on an Intel Xeon CPU (1.80GHz x 8) with 32GB RAM.

3.3.3 Non-Rigid Registration Accuracy

3.3.3.1 Synthetic Data

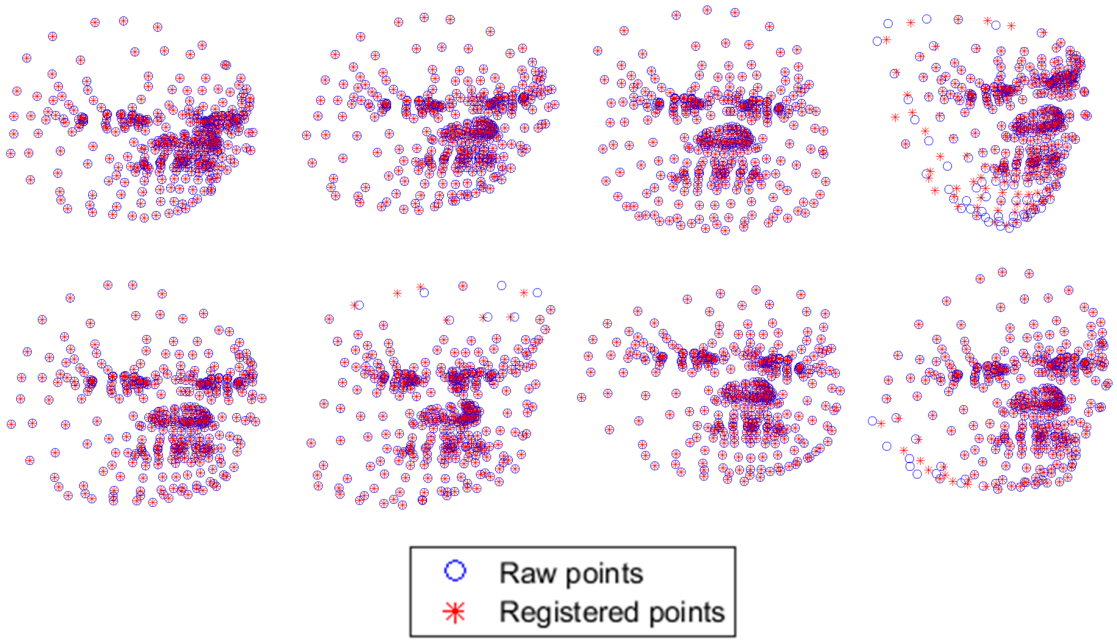

FIGURE 3.12: Synthetic 3D face data set registered using proposed TMM-NR.

Non-rigid registration accuracy of the proposed approach, TMM-NR, was compared with pair-wise non-rigid CPD and its group-wise variant (non-rigid gCPD), using the synthetic 3D face data set. Non-rigid gCPD was implemented

for the experiments conducted in this thesis (an additional contribution of the presented work), to enable direct comparison with our approach (TMM-NR), and to the best of our knowledge has not been presented in previous studies (although a similar approach based on GMMs without a uniform distribution component, was proposed in (Rasoulian, Rohling, and Abolmaesumi, 2012)). The raw point sets overlaid with the registered ground truth face point set, are shown in Fig. 3.12 (for a few cases). The mean HD and MSD measures, used to quantify registration accuracy, are presented in Table 3.9, for both methods. As discussed previously, statistical significance was assessed using a paired-sample t-test, considering a significance level of 5%. Significant improvements in registration accuracy are highlighted in bold, in Table 3.9. These results indicate that TMM-NR offers significant improvement over CPD and gCPD with regards to errors evaluated using the HD metric. On the other hand, both TMM-NR and pair-wise CPD were found to perform comparably, while outperforming gCPD, when compared using the MSD metric. The two user-specified parameters responsible for controlling the smoothness of the estimated deformation fields, were fixed for all experiments involving synthetic data as follows: $\lambda = 3$ and $\beta = 2$.

TABLE 3.9: Non-rigid registration errors evaluated for the synthetic 3D face data set.

Method	**HD (mm)**	**MSD (mm)**
CPD	0.15 ± 0.30	$\mathbf{0.002 \pm 0.004}$
gCPD (non-rigid)	0.11 ± 0.13	0.01 ± 0.007
TMM-NR	$\mathbf{0.007 \pm 0.002}$	$\mathbf{0.001 \pm 2.98} \times 10^{-4}$

3.3.3.2 Clinical Data

TABLE 3.10: Non-rigid registration errors for brain ventricles data set.

Method	**Ventricles** ($K = 27$)					
	$M = 500$		$M = 800$		$M = 1200$	
	HD (mm)	**MSD (mm)**	**HD (mm)**	**MSD (mm)**	**HD (mm)**	**MSD (mm)**
TMM	8.02 ± 2.95	2.20 ± 0.09	7.13 ± 2.48	1.91 ± 0.07	6.87 ± 2.25	1.78 ± 0.07
gCPD (non-rigid)	7.00 ± 2.06	**2.04** ± **0.11**	6.74 ± 2.13	1.72 ± 0.10	**5.54** ± **1.73**	1.24 ± 0.14
TMM-NR	7.40 ± 2.03	2.09 ± 0.12	7.04 ± 2.18	**1.68** ± **0.11**	7.20 ± 2.09	**1.20** ± **0.20**

The registration accuracy of TMM-NR was also evaluated using clinical data and compared with TMM-rigid and non-rigid gCPD. Registration errors for the ventricles data set were evaluated between the raw point sets and the deformed mean templates using the HD and MSD measures, presented in Table 3.10. The registered mean templates overlaid with their corresponding raw point sets (for a few cases) are depicted in Fig. 3.13. These images indicate that for certain samples (Fig. 3.13 (b,c,d,e)) exhibiting a high degree of localised deformations (denoted by arrows), the proposed registration approach (and similarly gCPD) are unable to accurately register the mean shape (Fig. 3.13 (a)). However, this is to be expected as the non-rigid transformation used in both methods enforces a global smoothness constraint on the deformation field, which does not permit large localised deformations. The samples presented in Fig. 3.13 (b,c,d,e), were chosen to highlight this limitation. Errors were computed for registrations performed using $M = 500, 800$ and 1200 mixture components. Non-rigid registration using both gCPD and TMM-NR were performed, keeping the associated registration parameters for all experiments as follows: $\lambda = 0.5$, $\beta = 0.5$. These were empirically determined to be suitable for this data set.

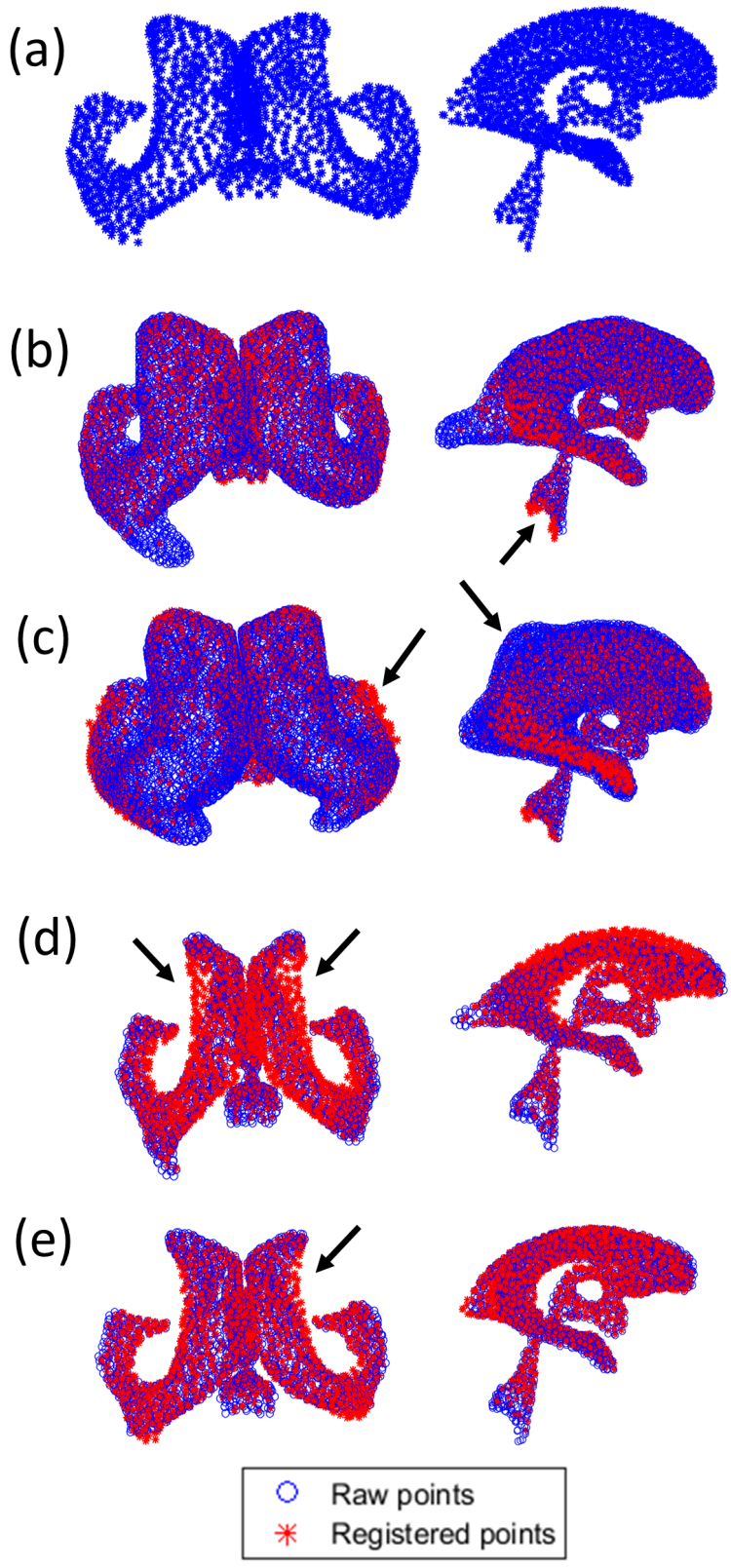

FIGURE 3.13: Ventricles data set registered using TMM-NR. (a) Estimated mean shape, (b)-(e) 4 raw point sets overlaid with registered mean shapes. Arrows indicate regions of severe localised deformations in some samples.

Statistically significant results (evaluated using paired-sample t-tests as in section 3.3.1.2) are highlighted in bold in the table. TMM-NR and gCPD consistently outperformed TMM-rigid, for errors evaluated using the MSD metric, due to the substantial non-linear variations in shape present across samples in the ventricles data set. The registration accuracy of all three methods was comparable in all experiments employing $M = 500, 800$ mixture components, based on errors evaluated using the HD metric. gCPD achieved significantly lower HD errors in comparison to both TMM-based methods, for $M = 1200$ mixture components and lower MSD errors at $M = 500$ mixture components. Conversely, for $M = 800, 1200$ mixture components, MSD errors were significantly lower for TMM-NR, relative to the others. These conflicting results are attributed to the presence of the posterior temporal horns of the lateral ventricles, in a limited number of samples in the data set (as illustrated by Fig. 3.13 (b,c)). Consequently, while gCPD attempts to establish correspondence in these regions, TMM-NR is more robust in this regard, due to its constituent t-distributions. Therefore, the correspondences established in these regions for some samples in the data set by gCPD, are not homologous to the remaining samples missing this structure, i.e. the established correspondences no longer represent the same anatomical feature. This in turn is reflected by the relatively high HD error evaluated using TMM-NR, compared to gCPD. Here, we define homologous correspondences as those that represent the same anatomical feature, based on the assumption that, samples without visible protrusions for the posterior temporal horns, are considered to lack these structures (rather than having very small posterior horns). The absence of these structures in some samples may be attributed to the pre-processing steps involved in generating the point sets (i.e. segmentation, surface generation and subsequent decimation of the surfaces). Consequently, the numerous correspondences established by gCPD in these regions are considered to be incorrect.

Although no significant differences in registration accuracy were apparent between TMM-NR and TMM-rigid methods, based on errors evaluated using the HD metric, visual inspection of the correspondences established using each method, highlight the advantage of the former over the latter. This is illustrated by the images shown in Fig. 3.14, which shows TMM-rigid is unable to establish anatomically valid correspondences, in the presence of significant non-linear variations in shape. This is particularly true for the gap present between the bodies of the left and right lateral ventricles, which exists due to the presence of thin membrane called the septum pellucidum. While TMM fails to preserve this

separation between the left and right lateral ventricles (refer to Fig. 3.14 (f,h)), TMM-NR and gCPD are marginally more successful in this regard. However, it is important to note that both TMM-NR and gCPD also incorrectly estimated a correspondences in this region. This limitation of both TMM-NR and gCPD is addressed further in **chapter** 5. Additionally, correspondences estimated in the anterior temporal horns of the left ventricle using TMM (refer to Fig. 3.14 (e,g)), are less accurate, relative to TMM-NR (refer to Fig. 3.14 (a,b)) and gCPD.

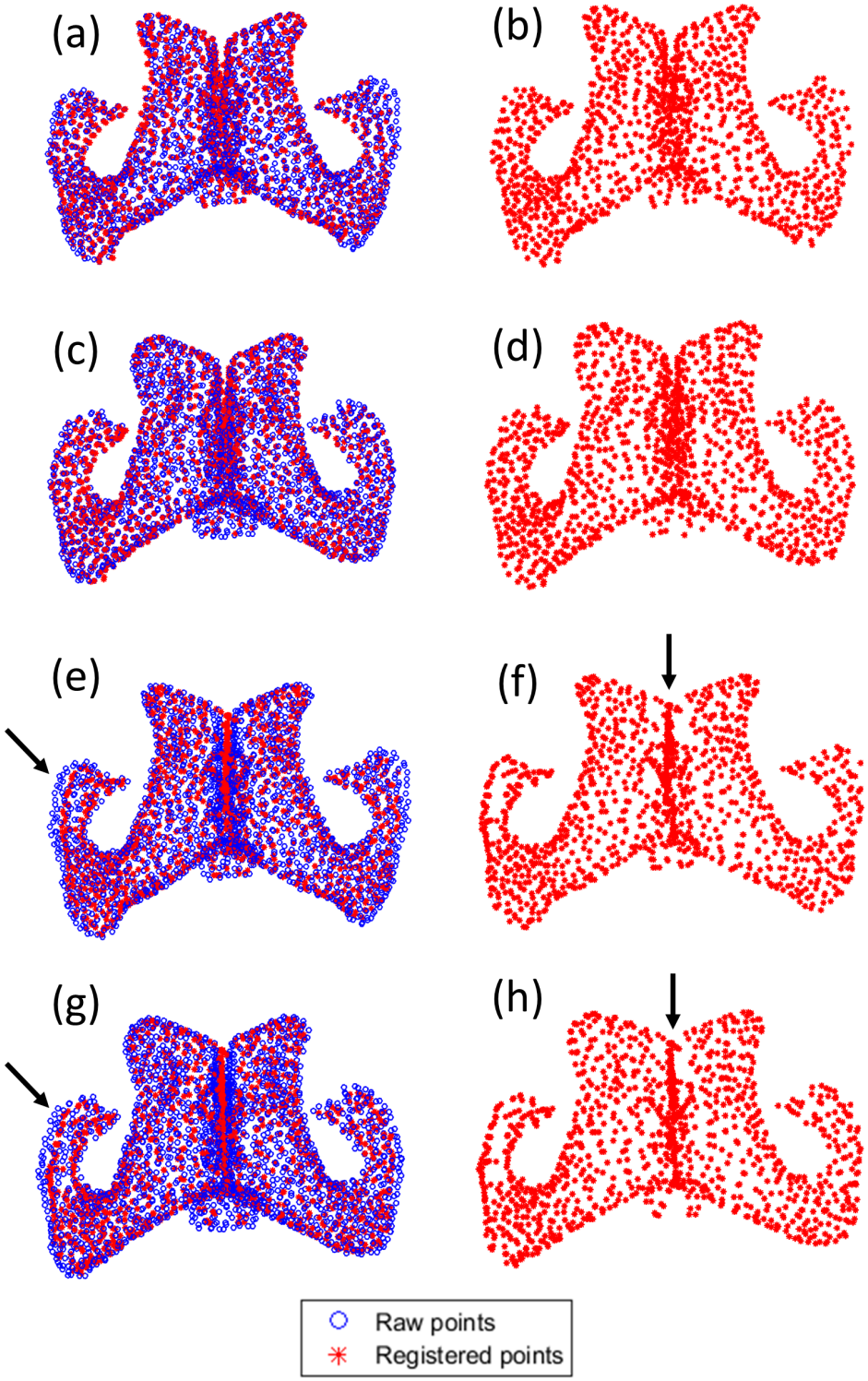

FIGURE 3.14: Correspondences estimated for two samples in ventricles data set using TMM-NR (a,b,c,d) and TMM rigid (e,f,g,h). Arrows indicate regions where the latter establishes invalid correspondences.

Although the performance of gCPD and TMM-NR was comparable in some aspects, the latter required fewer user-specified parameters (uniform distribution weight had to be tuned for the former; values ranging from 0.5 - 0.7 were found to be suitable, producing similar errors). However, as with the preceding set of registration experiments (discussed in section 3.3.1.2), the change in registration accuracy with different weights, was found to be marginal (due to the presence of minimal outliers in the ventricles data set). In light of these results, TMM-NR is inferred to be well suited to automatic registration of a group of shapes exhibiting complex and highly varied geometries. A major advantage of point set registration approaches is their flexibility, as they are independent of the topology of shapes to be registered. However, in certain scenarios this may represent a limitation of such approaches as well. For example, in the case of the femur data set, as there is no explicit constraint on the spacing of the points defining the femur boundaries or enforcing them to preserve the topology of the shape (i.e. represent a closed contour), registered point sets could have irregularly spaced points, leading to ambiguities when visualized as they may have gaps/open contours. Point set registration approaches that take into account the local structure of neighbouring points (Zheng and Doermann, 2006) or shape context (Belongie, Malik, and Puzicha, 2002), are suitable solutions to this problem of conserving the topology of shapes being matched. A similar issue is also encountered with complex 3D geometries, as with the data set of brain ventricles (refer to Fig. 3.14), where we found that both TMM-NR and gCPD failed to preserve the topology of the ventricles, by maintaining the separation between the left and right ventricular bodies. We address this issue by incorporating additional information describing the local geometry of shapes (to help preserve shape topology following registration), in the form of surface normal vectors, discussed further in **chapter** 5.

3.4 Conclusions

The rigid group-wise point set registration methods proposed in this chapter, namely, TMM and mrTMM, were shown to outperform state-of-the-art GMM-based techniques in terms of registration accuracy, using the synthetic data set. Their performance with the clinical data sets however, was comparable to gCPD. The proposed methods and gCPD consistently outperformed the other GMM-based approaches investigated, across all clinical data experiments. Although mrTMM offered significant improvement in registration accuracy over TMM on

synthetic data, their performance was comparable in most experiments involving clinical data. However, mrTMM also offered significant improvement in computational efficiency, achieving substantial reduction in execution times when registering all data sets, relative to TMM. Quicker convergence, without loss in registration accuracy is especially attractive for the analysis of large data sets.

The TMM-based non-rigid group-wise registration approach (TMM-NR) performed comparably to, or better than, a group-wise variant of non-rigid CPD, and pair-wise non-rigid CPD in terms of registration accuracy, using the synthetic 3D face data set. Using clinical data, comprising ventricular structures generated from AD, MCI and healthy cohorts, the proposed non-rigid group-wise registration approach (TMM-NR) performed comparably to non-rigid gCPD in most cases and consistently outperformed TMM-rigid, in terms of registration accuracy. Improvements in registration accuracy offered by both rigid and non-rigid formulations of the proposed framework in some cases, and their comparable performance in others, relative to the state-of-the-art, is promising for their application in a variety of computer vision and medical image analysis tasks, requiring automatic robustness to outliers.

Chapter 4

Statistical Shape Models

4.1 Introduction

'Shape' as defined by (Kendall, 1989), is the geometric information that remains once an object has been normalized with respect to rotation, scaling and translation. Various methods to represent this information and analyse the statistics of their variation across an ensemble of similar shapes have been proposed, some of which include point- or mesh-based discretisation (Cootes et al., 1995), implicit functions (signed distance maps) (Leventon, Grimson, and Faugeras, 2000), spherical harmonics (SPHARM) based parametrisation (Brechbühler, Gerig, and Kübler, 1995), (Gerig et al., 2001b) and medial shape representation (Pizer et al., 2003), (Styner et al., 2003). Among these, point-based representations of shape are the most prevalent for training SSMs using Principal Component Analysis (PCA), due to their simplicity and independence to topology. The latter property in particular is a desirable trait for anatomical structures, not afforded by some techniques such as SPHARM for example, which only permit shapes of spherical topology. Medial models are 'skeleton-like' representations which yield more compact shape descriptions than landmark-based approaches but utilise surface boundaries parametrised by SPHARM and consequently have identical topological constraints. Choice of shape representation thus plays a central role in, determining the variety of shapes that may be analysed, and in the selection of an appropriate registration technique for correcting global differences in pose and establishing correspondences.

Past approaches to automatic SSM generation have included: (1) a pair-wise, template-to-training set (or one-to-many) registration strategy where an atlas is non-rigidly registered to each training shape, thereby propagating the landmarks

used to represent the atlas shape across the training set and establishing correspondences (Lorenz and Krahnstöver, 2000), (Frangi et al., 2002); (2) population-based techniques based on minimum description length (MDL) (Davies et al., 2002), (Davies et al., 2010) or entropy (equivalent to MDL) (Cates et al., 2007), which automatically estimate correspondences across training shapes by optimizing an objective function dependent on model quality; and (3) group-wise point set registration methods for jointly aligning a group of shapes and establishing correspondences across them (Hufnagel et al., 2008), (Gooya, Davatzikos, and Frangi, 2015). A thorough review of various correspondence estimation approaches for training SSMs is provided in (Heimann and Meinzer, 2009). As discussed in the previous chapter, of particular interest in this thesis are the third group of techniques, due to their inherent flexibility and ability to establish correspondences in an unbiased manner. In contrast, population based techniques often perform the registration (for global pose corrections) and correspondence estimation steps, separately. While pair-wise registration approaches result in a bias towards the chosen atlas, registered to each sample in the training set.

Based on these criteria, point-based representations of shapes and the TMM-based group-wise registration framework discussed in the previous chapter are employed for training SSMs, as the objective is to design a framework independent of topology, automatic and robust to the presence of outliers. Adopting a probabilistic view of correspondences, also helps account for uncertainties in the registration process, not afforded by techniques relying on one-to-one mapping. This is particularly crucial when automatic segmentation and point set generation techniques are employed, to generate the requisite training shapes, as done in this study. Additionally, point-based representation of shapes are computationally less expensive than their implicit (signed distance functions) counterparts for example, in relation to SSM construction and application.

Statistical shape models have found widespread use in a variety of medical image analysis applications in recent years such as segmentation (Patenaude et al., 2011), (Castro-Mateos et al., 2015), shape-based prediction of tissue anisotropy (Lekadir et al., 2014), quantitative shape analysis and classification for computer-aided-diagnosis (Styner et al., 2004), (Shen et al., 2012), (Gooya et al., 2015), to name a few. Their primary challenge has persistently been the availability of training sets of sufficient size, necessary to adequately describe anatomical shape variability observed across different demographic and diagnostic populations. A training set of segmentations delineating the structure of interest in medical images, is typically generated manually or semi-automatically, which is laborious

and prohibitive when analysing 3D structures from large cohorts. In the past, various solutions have been proposed, such as merging pre-existing SSMs trained from different cohorts (Pereañez et al., 2014), generating synthetic variations in shape using deformable transformations (Koikkalainen et al., 2008) to enrich the data set with a higher degree of variability, and employing automatic techniques to generate the required training set of segmentations, which is of particular interest in this study. The major challenges with this approach are the potential inclusion of outliers and the presence of missing information in the segmentations, as a result of variable image resolution and quality, motion artefacts, pathology-induced intensity inhomogeneities, among others. Consequently, in order to facilitate large-scale statistical shape analysis of anatomical structures using automated techniques for generating training shapes, a robust framework capable of rigidly aligning such instances and establishing anatomically valid correspondences across the same, is imperative. The TMM-based methods presented in the previous chapter address these issues and are therefore used here to construct SSMs by PCA. The quality of the resulting SSMs are quantitatively evaluated and compared with the state-of-the-art, in this chapter.

4.2 Principal Component Analysis: SSM Generation and Model-fitting

Following registration of a group of shapes using any of the methods discussed in the previous chapter, the estimated posterior probabilities are employed to establish soft-correspondences, which in turn are used to train SSMs by PCA. The resulting eigenvectors $\Phi \in \mathbb{R}^{D\times M\times m}$ (where m is the number of modes of variation retained), represent the principal axes of the shape space and eigenvalues $\lambda_{n=1\ldots m}$ describe the proportion of the total variation in shape described by each corresponding mode of variation. All SSMs trained in this study retained eigenmodes that describe 95% of the total variation in shape across each corresponding group. The process of fitting the trained models to new data involves two steps: (1) mixture-fitting and (2) SSM-fitting. The former is first used to align the new shape to the trained mean model and establish correspondences. This step is analogous to pair-wise registration, where the learnt mixture model parameters, apart from the variance, (i.e. mixture centroids, coefficients, and degrees of freedom) remain fixed, as the trained mean model is iteratively aligned to the test shape. Correspondence probabilities defined by posterior probabilities, are

evaluated similarly to group-wise and pair-wise registration approaches, at each EM-iteration. From these, soft correspondences $\mathbf{v}$ are estimated as shown in equation 4.1a, where $P^{\star}_{ij}$ represents the corrected posterior probabilities (as discussed in section 3.2.3) estimated following alignment of the new shape to the mean model and $\mathbf{T}$ represents the corresponding similarity transformation. The estimated correspondences are subsequently projected to the trained SSM according to equation 4.1b, to obtain estimates of principal component coefficients $\mathbf{b}$. Here, $\bar{\mathbf{x}}$ represents the mean shape vector and $\bar{\mathbf{v}}$ represents the vector of estimated soft correspondences. Vector $\mathbf{b}$ represents the set of parameters used to generate variations in shape and are used to reconstruct the new shape $\mathbf{x}^{new}$, using equation 4.1c. To reduce the influence of noise on shape reconstruction, the estimated PCA coefficients are constrained as: $|b_n| \leq 3\sqrt{\lambda_n}$, where λ_n represents the eigenvalue of the n^{th} mode of variation.

$$\mathbf{v} = \frac{\sum_{i=1}^{N} P^{\star}_{ij} \mathbf{T}\mathbf{x}_i}{\sum_{i=1}^{N} P^{\star}_{ij}} \tag{4.1a}$$

$$\mathbf{b} = \Phi^T(\bar{\mathbf{v}} - \bar{\mathbf{x}}) \tag{4.1b}$$

$$\mathbf{x}^{new} = \bar{\mathbf{x}} + \Phi\mathbf{b} \tag{4.1c}$$

4.3 Results and Discussion

The quality of SSMs trained in this manner was assessed based on their generality, specificity and compactness. The following clinical data sets were used in the testing: `Femur` ($K = 1000$), `Hippocampus_MCI` ($K = 28$), `Hippocampus_Ctrl` ($K = 50$) and `Heart` ($K = 30$) (described in the previous chapter). Generalisation and specificity errors were evaluated using the MSD metric, computed between the ground truth test shape and the corresponding model-predicted shape. These measures were computed for models trained using: single- and multi-resolution TMM, SpSSM, a group-wise variant of CPD, and GMM. We employ our own implementation of group-wise CPD (gCPD) rather than JRMPC, as the latter estimates strictly rigid transformations, rather than the desired similarity transformations. Furthermore, gCPD is preferred to the original pair-wise approach to enable direct comparison with the other methods investigated. SpSSM

and GMM are purely Gaussian-based and differ in the manner of estimation of the mixture coefficients, while gCPD incorporates a uniform distribution component in the mixture model. Together they represent a range of GMM-based, rigid, group-wise point set registration techniques proposed in recent years, suitable for assessing the advantage of the proposed TMM-based methods.

Generalisation quantifies the ability of SSMs to reconstruct unseen shapes i.e. samples excluded from the training set. Compactness measures their ability to describe variation in shape across a group, with a minimal set of parameters — i.e. the fewest modes of variation. It can also formally be defined as the cumulative sum of eigenvalues associated with the modes of variation. It is also crucial for SSMs to generate anatomically plausible instances and, consequently, this is used as a measure of their quality known as specificity.

To avoid over- or under-fitting to data, it is necessary to balance model complexity with performance. To this end, we identified the optimal number of mixture components (M_{opt}) for each clinical data set by conducting ten-fold cross validation experiments, evaluating the quality of SSMs trained. For the generalization experiments, 10 unseen test shapes from the same cohort (as the training samples) were used for the femur data set. For the hippocampi, 10 test shapes for both healthy and MCI groups were generated automatically from a separate database of MR images (also acquired as part of the VPH-DARE@IT project vph-dare.eu), using a different state-of-the-art segmentation tool based on geodesic information flows (GIF parcellation) (Cardoso et al., 2015),(Prados Carrasco et al., 2016). This method of validation for the hippocampi was selected to evaluate the ability of the proposed framework to characterise unseen shapes generated using a different protocol, to better emulate a real clinical scenario. Finally, for the heart data set 10 unseen shapes were selected, comprising three samples each from the PH and HCM patient groups respectively, and four from the healthy cohort.

The quality of SSMs trained using the identified M_{opt} for each data set, were also assessed with respect to the number of modes of variation by leave-one-out full-fold cross validation. This second set of cross validation experiments evaluates the quality of the trained models to characterise unseen shapes from the same cohort as the training sets. It is important to note that, correspondences were estimated jointly across both training and test shapes in all experiments evaluating generalization with respect to the number of modes of variation. Specificity and compactness were also assessed in this manner by leave-one-out full-fold cross-validation. In the former case, two shapes were randomly sampled from

the trained SSMs (using progressively increasing number of eigenmodes) and their mean surface distance to each left out case from the training set was computed. Compactness was assessed by plotting the cumulative sum of the percentage of variation (computed using the estimated eigenvalues) described by each eigenmode, against the modes of variation. Table C.2 in Appendix C further describes the generalisation and specificity experiments conducted in order to assess SSM quality. Generalisation and specificity errors (with respect to the number of modes of variation) were evaluated using the MSD metric, computed between (left-out) ground truth test shape and the corresponding model-predicted shape, as stated previously, for the hippocampi and heart data sets. However, for the femur data set, as a large number of samples contained significant proportions of outliers, these measures were computed between the estimated correspondences for each test shape (rather than the ground truth point set) and the SSM-predicted shape. This was done as errors computed using the ground truth point sets would be heavily skewed due to the presence of outliers and would be difficult to interpret in order to compare the various registration methods investigated.

4.3.1 Generalisation

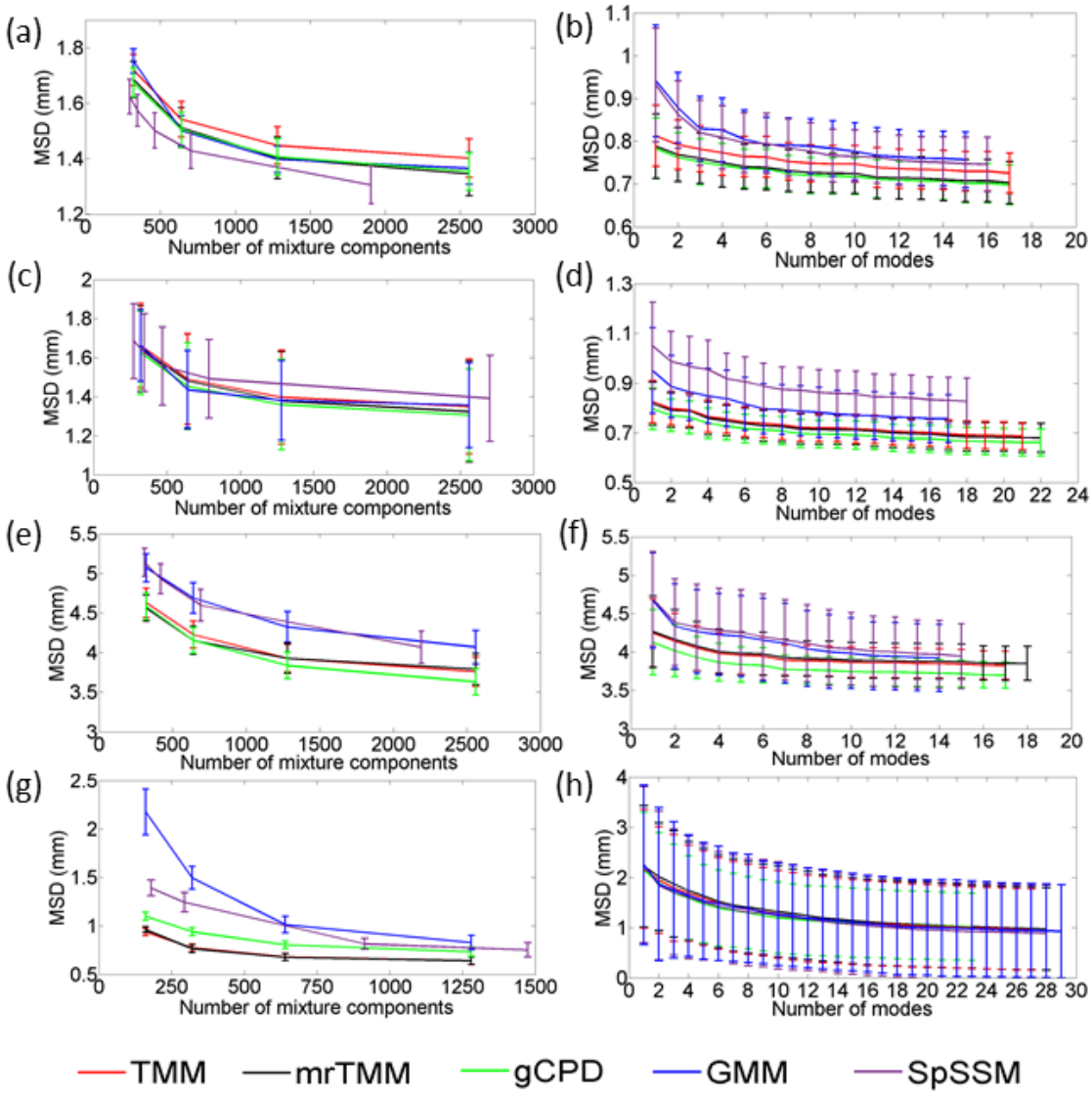

FIGURE 4.1: SSM generalization errors evaluated with respect to number of mixture components (left column) and number of modes of variation (right column). (a,b) MCI-hippocampi, (c,d) healthy-hippocampi, (e,f) heart and (g,h) 2D-femur data set. Errors reported in (a,c,e,g) were evaluated by retaining modes describing 95% of the total variation in the corresponding SSMs.

Generalisation errors were computed with respect to the number of mixture components employed and, subsequently, the modes of variation of the trained SSMs (using the identified optimal number of mixture components from the preceding experiments). Fig. 4.1 summarises these results for each clinical data set. Fig.

4.1(a) and (c) depict generalization errors evaluated with respect to the number of mixture components, for the MCI and healthy hippocampi data sets, respectively. The proposed methods perform comparably to GMM and gCPD while SpSSM achieves marginally lower errors for the MCI data. However, for the healthy-hippocampi, the proposed methods, GMM and gCPD outperform SpSSM and perform comparably to each other. While mrTMM offers some improvement over single-resolution TMM, as the training sets of hippocampi shapes contained no visibly apparent outliers, both proposed methods showed no significant difference in performance compared to GMM and gCPD. SpSSM achieves significantly lower errors than TMM for the MCI-hippocampi data set but shows no significant difference to mrTMM. As noted previously, in cases where the training data contains few outliers, the constituent t-distributions of a TMM behave similarly to Gaussians (due to estimation of large values for the associated degrees of freedom ν, as shown in Fig. 3.10(d)) and consequently SSMs trained using both classes of techniques are found to be of comparable quality.

A similar result is obtained for the heart data set, which contained few visibly apparent outliers, with gCPD, TMM and mrTMM significantly outperforming GMM and SpSSM, as illustrated by the generalization errors presented in Fig. 4.1(e). The heart data set comprised of samples with significant variations in geometry as a result of pathology (due to PH and HCM), which may be interpreted as missing information or outliers by the mixture model during registration (supported by the higher proportion of low ν values reported in Fig. 3.10(c), compared to the MCI-hippocampi data set, Fig. 3.10(d)). Correspondingly, the lower errors achieved by gCPD, TMM and mrTMM are inferred to result from their robust nature, while GMM and SpSSM, lacking this quality, result in sub-optimal registration of the samples and by extension lower quality SSMs. Based on these experiments, the optimal number of mixture components was identified to be $M_{opt} = 2560$, for both hippocampi and heart data sets, using GMM, gCPD, TMM, and mrTMM. With SpSSM a sparsity level of 0.1 was found to be optimal for the hippocampi and heart data sets, resulting in $M_{opt} = 1906$ for the MCI group, $M_{opt} = 2702$ for the healthy group, and $M_{opt} = 2191$ for the heart. Generalisation errors evaluated with respect to the modes of variation for the MCI-hippocampi (Fig.4.1(b)) show that while TMM performs comparably to GMM and SpSSM (with some marginal improvement), mrTMM and gCPD significantly outperform the same. A similar result is obtained for the healthy-hippocampi (Fig. 4.1(d)), with gCPD, TMM and mrTMM all providing substantial improvements to GMM and SpSSM. For the heart data set, (Fig. 4.1(f)) gCPD, TMM and mrTMM, once

again offer marginal improvements over GMM and SpSSM.

Generalisation errors for the femur data set are presented in Fig. 4.1 (g) and (h), evaluated with respect to the number of mixture components and the modes of variation, respectively. As highlighted previously, the femur data set contained multiple training samples with significant outliers which adversely affected the quality of SSMs trained using the GMM-based approaches. Models trained using TMM and mrTMM on the other hand were robust to the presence of these outliers, resulting in significantly lower generalization errors compared to the state-of-the-art, when evaluated with respect to the number of mixture components (Fig. 4.1(g)). Fig. 4.1(h) suggests that the quality of SSMs generated are comparable across all methods, when evaluated with respect to the number of modes of variation. These results indicate that the proposed methods are able to reconstruct new shapes to a higher degree of accuracy. However, when correspondences are jointly estimated across all training and test shapes (as done with the generalization experiments evaluated with respect to the modes of variation) and SSM quality is subsequently evaluated by leave-one-out cross validation, the generalization-ability of the models is comparable across all methods. As the former set of generalization experiments (evaluated with respect to the number of mixture components), better emulate a real scenario, the improvement in reconstruction accuracy offered by both TMM and mrTMM compared to their GMM-counterparts, is compelling. Both TMM and mrTMM performed comparably across all generalization experiments conducted, with mrTMM offering marginal improvements in some cases.

4.3.2 Specificity

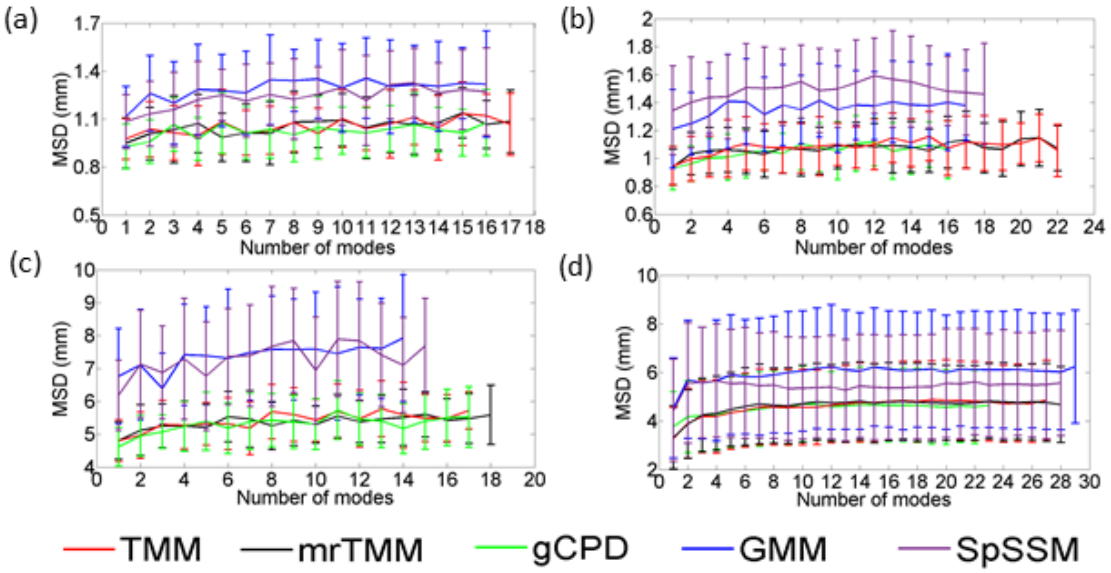

FIGURE 4.2: SSM specificity errors evaluated with respect to the modes of variation for (a) MCI-hippocampi, (b) healthy-hippocampi, (c) heart, and (d) 2D-femur data sets.

The specificity errors presented in Fig. 4.2 (a), (b) and (c) show that models trained using the proposed methods and gCPD achieve significantly lower errors than GMM and SpSSM and are inferred to generate shapes with a higher degree of anatomical plausibility, for both hippocampi, and the heart data sets. For the femur data set, as noted previously, wrong correspondences estimated using the GMM-based methods result in incorrect modes of variation. Consequently, shapes sampled randomly from the trained SSMs are implausible, resulting in the high specificity errors seen in Fig. 4.2(d). TMM, mrTMM and gCPD however, are robust to the presence of outliers in the training set and consequently achieve significantly lower specificity errors compared to the GMM and SpSSM. These results are consistent with those observed in the generalization experiments, indicating the superiority of the proposed methods when dealing with data containing outliers. As with the generalization experiments, the specificity of the models trained using TMM and mrTMM are similar. Although specificity experiments conducted using the femur data set indicate that TMM, mrTMM and gCPD are comparably robust and produce SSMs of similar quality, visual inspection of the modes of variation (and correspondingly of the model-predicted shapes) highlight the advantage of the proposed methods over gCPD, as illustrated by Fig.

4.3. The presence of large proportions of outliers in the training samples adversely affects the correspondences established using gCPD resulting in a mean shape and modes of variation that contain points offset from the true boundary of the femoral head (Fig. 4.3(a,b)). In comparison, both TMM and mrTMM are able to suppress the influence of such outliers and establish valid correspondences, resulting in plausible mean shapes and modes of variation (as shown in Fig. 4.3(c-f)).

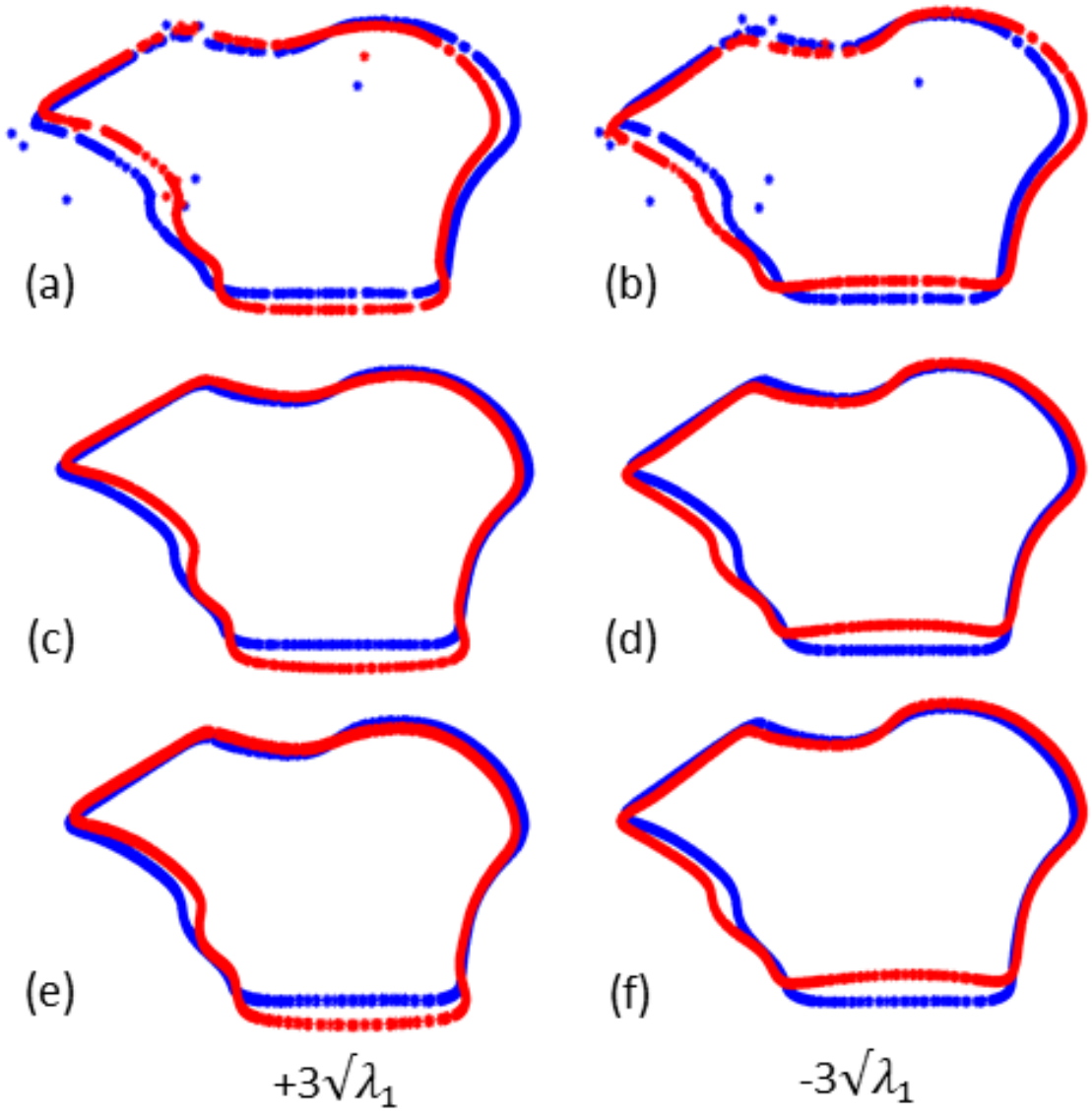

FIGURE 4.3: First mode of variation for the 2D-femur data set (red) overlaid on the estimated mean shape (black). SSMs were trained using: gCPD (a,b), TMM (c,d), and mrTMM (e,f). Here λ_1 denotes the first eigenvalue.

4.3.3 Compactness

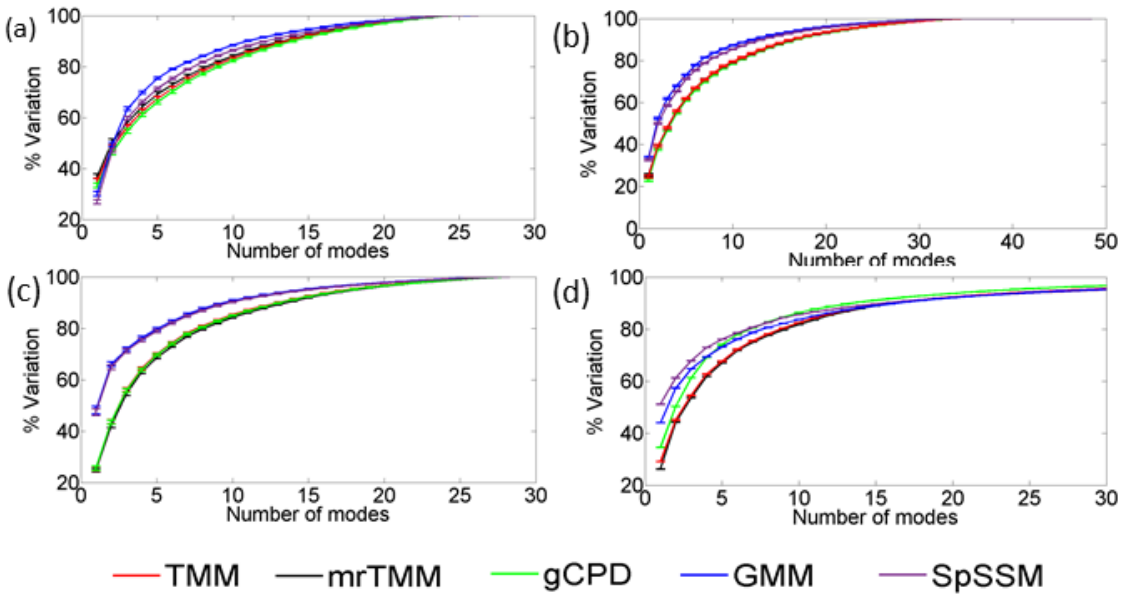

FIGURE 4.4: SSM compactness assessed by plotting the cumulative sum of the variation % (expressed by each eigenmode), against the number of modes. (a) MCI-hippocampi, (b) healthy-hippocampi, (c) heart, and (d) 2D-femur data set.

Cross-validation experiments revealed that SSMs generated using SpSSM, gCPD, and both proposed methods were equally compact, for the MCI-hippocampi (Fig. 4.4(a)), while GMM generated more compact models. However, based on the generalization errors presented in Fig. 4.1(b) we note that improved compactness of GMM is at the expense of reduced generalization ability and model specificity (Fig. 4.2(a)). With the healthy hippocampi data set, both GMM and SpSSM produced models that were significantly more compact than gCPD and the proposed methods (Fig. 4.4(b)), however, once again at cost of lower generalization ability and model specificity (as illustrated by Fig. 4.1(d) and Fig. 4.2(b)). For the MCI-hippocampi data set (containing $K = 28$ samples), up to 17 eigenmodes were found to capture 95% of the total variation in shape found in the training set, while the healthy-hippocampi set (containing $K = 50$ samples) required up to 22 modes of variation. The heart data set ($K = 30$ samples), comprising instances of healthy subjects and patients diagnosed with PH and HCM, required up to 18 eigenmodes, using the proposed methods, with GMM and SpSSM generating more compact models (Fig. 4.4(c)). As with the hippocampi, although GMM and SpSSM generated more compact models, they suffered from reduced

generalisation-ability and specificity. The variation in shape across the 2D femur data set containing $K = 1000$ samples was adequately captured by all methods, within 30 modes of variation and a similar trend is observed as with the remaining data sets, i.e. all three GMM-based methods produce more compact models than TMM and mrTMM, at the cost of higher generalisation and specificity errors.

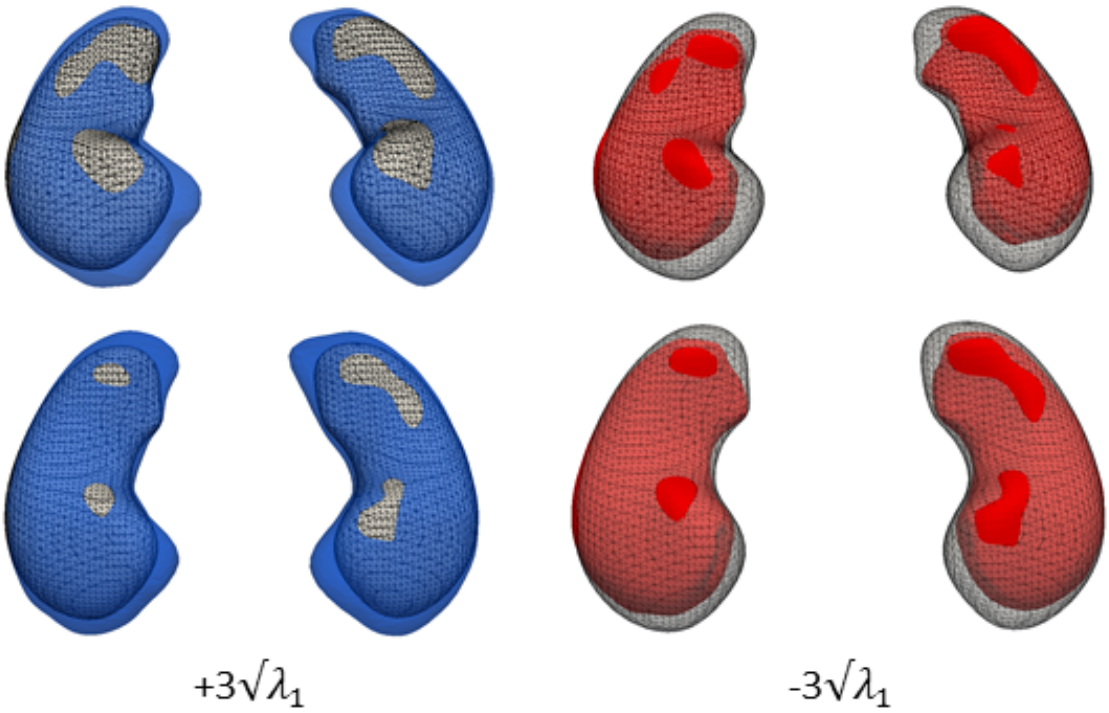

FIGURE 4.5: First mode of variation for SSMs trained using mrTMM. Top row: MCI hippocampi, bottom row: healthy hippocampi. In all cases the overlaid surface mesh with visible edges represents the mean shape.

The first mode of variation for the MCI- and healthy-hippocampi data sets are depicted in Fig. 4.5 and those for the heart are in Fig. 4.6. It is interesting to note that the first mode of variation for the presented heart-SSM describes a change in the shape and volume of the right ventricle, characteristic of pulmonary hypertension. The presented SSMs in Fig. 4.5 and 4.6 were trained using mrTMM and the optimal number of mixture components identified for each data set (refer to section 4.3.1).

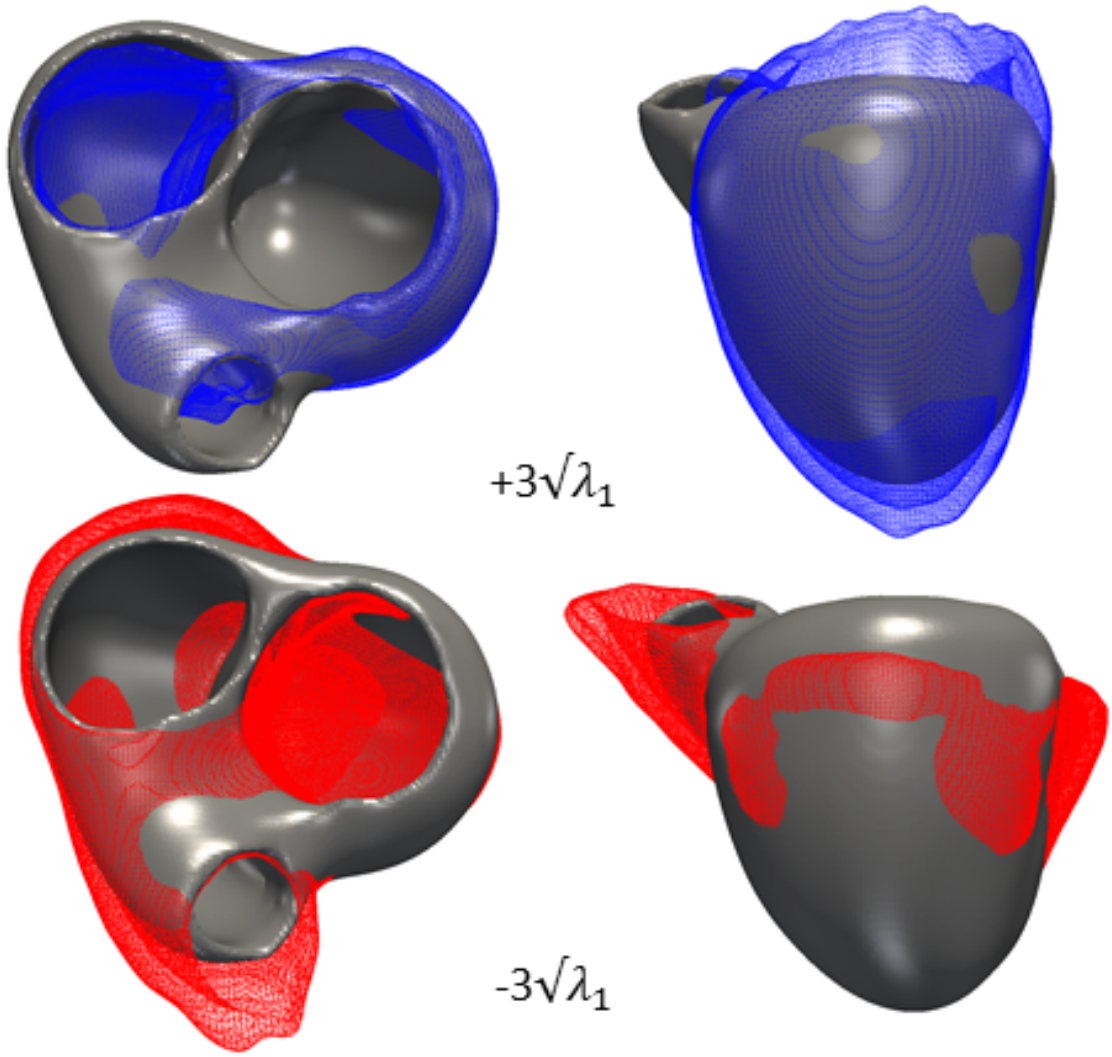

FIGURE 4.6: First mode of variation of the heart-SSM trained using mrTMM, overlaid on the estimated mean shape (dark grey surface).

The improvement in SSM quality achieved using TMM and mrTMM, when dealing with noisy data, is demonstrated by the generalization and specificity experiments conducted in this study. Their ability to automatically align shapes in a robust fashion and reconstruct unseen shapes to a high degree of accuracy, can find application in large-scale studies investigating shape and morphological changes associated with pathological processes, as seen with dementia-related hippocampal changes, pulmonary hypertension and hypertrophic cardiomyopathy induced changes to ventricular morphology in the heart, among others. Additionally, the proposed methods can find use in intra-operative guidance applications requiring robust and automatic pose correction. The proposed methods

can also be employed to initialize a subsequent deformable registration step (discussed in the previous chapter), often necessary to capture soft tissue deformations common to surgical procedures.

4.4 Conclusions

Cross-validation experiments evaluating SSM quality indicate that the proposed methods (TMM and mrTMM) are comparable to a state-of-the-art approach (gCPD) for data containing few outliers, but outperform the same in the presence of outliers (as in the femur data set). The proposed techniques outperform other GMM-based methods investigated, namely, GMM and SpSSM, with regards to generalisation and specificity, in the majority of experiments conducted. Additionally, although the performance of gCPD, TMM and mrTMM is comparable in many cases, the former required tuning of the weight parameter controlling the robustness of the model to outliers, for optimal registration and by extension SSM quality. Although the sensitivity of registration accuracy and SSM quality to different weights employed with gCPD was marginal for data sets containing few outliers (such as the hippocampi and heart data sets), it was more pronounced for data containing significant proportions of outliers (as with the femur data set). In contrast, TMM and mrTMM were automatically robust to missing data and significant proportions of outliers in all cases, making them well-suited to SSM generation, when automated techniques are used to generate the requisite training sets. Both methods are, consequently, well suited to automatic shape analysis of large cohorts.

Chapter 5

Registration of Generalised Point Sets

5.1 Introduction

Group-wise registration of multi-dimensional unstructured point sets comprising different types of data such as: vector-valued (spatial positions, axial/directional) and scalar-valued quantities, offers a unique perspective to addressing a variety of applications in computer vision and medical image analysis. This is especially true for circumstances where, spatial position alone, is inadequate as a descriptor for accurate registration. In this chapter, a probabilistic approach for group-wise registration of *generalised point sets* is proposed. This is achieved through formulation of a hybrid mixture model (HMM), combining suitable probability distributions to model disparate data features, within a cohesive framework. Two variants of the HMM are presented: (1) for modelling axial data; and (2) suited to directional data. Here axial data refers to vectors that are randomly oriented along an axis, i.e. the orientation of the axis itself is the quantity of interest, rather than any specific direction along the axis. As exemplar applications, the proposed framework is employed for the joint registration and clustering of: magnetic resonance (MR) diffusion tensor image (DTI)-derived data, acquired from multiple subjects, addressed by (1); and hybrid representations of shapes defined by spatial positions of points, with associated surface normal vectors, addressed by (2). The former is of particular interest in this chapter (henceforth referred to as **Application 1**), while the latter serves to highlight the flexibility of the presented work (referred to as **Application 2**). The generic nature of the proposed framework is well-suited to registering other types of hybrid point sets comprising discriminative features (such as principal curvatures, integral descriptors, vessel

radii/diameters, etc.). High-dimensional feature vectors are in general, more descriptive than spatial positions alone, and improve discriminative capacity when establishing correspondences, due to the low probability of matching all features.

Magnetic resonance diffusion tensor imaging (DTI) has found widespread use in studies investigating localised changes to structure and connectivity within brain white matter (WM) and their potential as biomarkers for dementia and other neurodegenerative diseases. DTIs are estimated from diffusion weighted images (DWIs), which encode diffusion of varying strengths along different gradient directions. MR DTI use a diffusion tensor model (Basser, Mattiello, and LeBihan, 1994) that, under some assumptions, can be related to local tissue microstructure. They aid in voxel-wise quantification of diffusion characteristics, which may be expressed in terms of principal eigenvectors and eigenvalues of the estimated diffusion tensors. Tissue microstructure affects local diffusion properties. For example, water diffuses preferentially, parallel to the major axis of a fibre bundle as opposed to perpendicular to it and, consequently, gives rise to the sense of tissue anisotropy commonly observed in major WM tracts. Fractional anisotropy (FA), a measure frequently employed to describe tissue anisotropy (Pierpaoli and Basser, 1996), represents the degree of directional dependence in diffusion at a specific voxel. The primary eigenvector of a diffusion tensor represents the preferred direction for the diffusion of water at any given voxel, and is often interpreted as reflecting the local fibre orientation within tissue.

Region of interest –ROI-based– analyses have been used to assess changes in local (Salat et al., 2005) and global (Cercignani et al., 2001) tissue diffusion properties. A limitation of such approaches is the need for accurately delineating ROIs across multiple patients'/subjects' images. Consequently, they are affected by low reproducibility, leading to discrepancies across studies. Tract-based spatial statistics (TBSS) (Smith et al., 2006) and voxel-based morphometric (VBM) approaches (Ashburner and Friston, 2000) are suitable alternatives that are fully automatic and enable analysis of localised changes to FA and other diffusion measures, across the entire WM volume. The quality of non-rigid registration used in VBM significantly influences the subsequent voxel-wise analysis. To overcome this issue, (Smith et al., 2006) proposed the widely used TBSS approach, which ensures that registration quality has less influence on subsequent statistical analysis of FA (and other diffusion-derived quantities). TBSS constructs an alignment invariant mean FA skeleton following registration of subjects' FA images to a template. Neighbouring voxels located perpendicular to the skeleton are identified for each subject, and the highest FA values (assumed to represent tract centres)

are assigned to each skeleton voxel. The resulting projections to the skeleton enable statistical analysis across multiple subjects.

Alternative probabilistic techniques that jointly register and cluster WM fibre trajectories (obtained from diffusion tractography), and which enable quantitative analysis of diffusion measures over fibre pathways (rather than voxel-wise quantification), have also been proposed. For example, registration of curves and fibre bundles using diffeomorphisms and currents, and a statistical framework to assess variability in geometry and fibre density across a population, was proposed by (Durrleman et al., 2009), (Durrleman et al., 2011). (Maddah et al., 2008) employ a Gamma mixture modelling framework to register fibre trajectories by establishing probabilistic correspondences, and jointly cluster them into representative fibre bundles. The authors also note therein, through use of a suitable fibre tract atlas as a prior during the clustering procedure, correspondences may be estimated across fibre trajectories obtained from multiple subjects, thereby enabling statistical analysis of FA and other diffusion quantities across populations. In (Zvitia et al., 2010), the authors propose a combined adaptive mean shift and Gaussian mixture model (GMM) formulation to jointly cluster fibre trajectories into compact fibre sets, and subsequently register fibre sets obtained from multiple subjects. The registration of two clustered fibre sets is formulated as a problem of aligning two distinct GMMs, analogous to point set registration using GMMs (Jian and Vemuri, 2005). Similar approaches to clustering fibre trajectories across a population, using spectral embedding, have also been proposed (O'Donnell and Westin, 2007), facilitating the estimation of WM atlases and enabling automatic segmentation of major WM tracts. Such techniques are however, dependent on the tractography algorithm employed to estimate fibre trajectories and typically require user intervention.

Applications of the various methods described above have included, for example, identification of relationships between mild cognitive impairment (MCI) and Alzheimer's disease (AD), and localised changes to WM diffusion characteristics. For example, in (Zhang et al., 2007), ROI-based analysis was used to identify significant reduction in FA in the cingulum for patients diagnosed with MCI and AD, relative to healthy controls (HC). In (Medina et al., 2006), VBM was used to identify significant reduction in FA, in posterior regions of the brain, for MCI and AD patient groups. While, (Liu et al., 2011) used the TBSS-approach, and found reduced FA in the cingulum, corpus callosal and inferior/superior longitudinal fasiculus tracts, among others. As the cingulum and corpus callosal regions have been of significant interest in previous studies investigating

dementia-related changes to diffusion characteristics within WM, they are considered for **Application 1**, as an exemplar study for the proposed HMM-based joint registration and clustering framework.

The proposed framework is employed to jointly register and cluster brain diffusion MRI data, to enable statistical analysis of DTI-derived measures, as an alternative to existing VBM- and TBSS-based approaches. The latter are based on non-rigid registration of subjects' FA images to a standard space to perform such analysis. Instead, our approach uses group-wise non-rigid point set registration based on a hybrid mixture modelling framework, which approximates the joint probability density of: (1) spatial positions (of voxel centroids within a region/tract of interest), (2) the primary diffusion axes/fibre orientations, and (3) fractional anisotropy, estimated at the voxels of interest. The proposed framework is flexible and can be used to model other diffusion-derived data such as mean/radial diffusivity, relative anisotropy, tensor-eigenvalues, etc. — a functionality also afforded by TBSS. However, the proposed approach also enables analysis of the variation in fibre orientations, across multiple subjects, which cannot be done using TBSS. While VBM-based approaches allow for such analyses through co-registration of DTIs acquired from multiple subjects, they are dependent on the accuracy of non-rigid registration and the exact estimation of correspondences, to ensure validity in the subsequent voxel-wise statistical analyses. On the other hand, TBSS and our approach are less restrictive in this regard. In the proposed approach, correspondence probabilities are estimated by approximating the joint probability density of position, fibre orientation and FA, which are iteratively revised as the registration progresses. Consequently, three distinct sources of information are leveraged to guide the registration of an unbiased, study-specific atlas, onto each subject's WM tract/region of interest. The evolving soft correspondences provide model-based estimates for the mean primary diffusion axis and FA value (for a given population) at each component in the mixture model and help mitigate any misalignment incurred during registration.

Additionally, VBM-based approaches employing DTI-registration are often pair-wise in nature, requiring selection of a suitable reference template, not viable in many pathological scenarios. Statistical analysis of fibre orientations across multiple subjects and comparisons between patient groups was pursued in a previous study (Schwartzman, Dougherty, and Taylor, 2005), using such an approach. DTIs from multiple subjects were spatially normalized to a reference template and subsequently, Watson distributions were fitted by maximum likelihood estimation, to the fibre orientations observed across a group, for each voxel,

independently. This provided a measure of the mean orientation and dispersion, observed across the group of subjects. A drawback of such an approach however, is the need to choose a single, appropriate template, for registration. All subsequent registrations performed and correspondences estimated are biased towards the chosen template.

In the context of **Application 1**, the proposed approach models the *PDF* of primary diffusion axes (henceforth referred to as fibre orientations for brevity), rather than the directions of the observed primary diffusion eigenvectors, which tend to be random (as diffusion tensors are antipodally symmetric). Registration of WM regions (defined by hybrid point sets comprising position, fibre orientation and FA) across subjects, is achieved using a group-wise rigid, and subsequent non-rigid point set registration approach, based on a HMM. Spatial positions (defined by voxel centroids) are modelled using a Student's t-mixture model (TMM), fibre orientations are approximated using a Watson mixture model (WMM), while a GMM approximates the FA density. We chose to model the distribution of FA using a GMM rather than a Gamma mixture model (which would intuitively be a suitable choice) as GMMs are computationally efficient to implement, since closed-form solutions exist for the associated model parameters, and it ensures that the FA values predicted at the established correspondences, are Gaussian-distributed across subjects. The latter is useful for conducting subsequent statistical analyses. Only two previous studies (Billings and Taylor, 2014), (Billings and Taylor, 2015), have attempted to model the joint density of position and orientation, within a point set registration framework. In these studies the authors proposed variants of the iterative closest point (ICP) registration algorithm for pair-wise rigid shape registration, called iterative most likely oriented point registration (IMLOP) (Billings and Taylor, 2014) and generalized-IMLOP (Billings and Taylor, 2015). Both methods model the joint *PDF* of points and their associated surface normals using a combination of Gaussian and Von-Mises-Fisher distributions, in an expectation maximisation (EM)-based mixture modelling framework. We adopt a similar approach in this study, but favour Student's t-distributions in place of Gaussians for modelling positions, due to the improved robustness to outliers of the former, re-formulate the approach for group-wise registration (rather than pair-wise), and incorporate an explicit model of FA distributions, as described. Furthermore, for **Application 1** Watson distributions are favoured over Fisher distributions as they are antipodally symmetric, unlike the latter. Conversely, for **Application 2**, Fisher distributions are employed (in place of Watsons), in combination with Student's t-distributions, to model the

joint *PDF* of points and their associated surface normals (similar to (Billings and Taylor, 2014) and (Billings and Taylor, 2015)).

The primary motivation for the Watson-distribution based HMM framework proposed herein, is to facilitate the statistical analysis of fibre orientations and FA values across multiple subjects. In the proposed framework, the constituent Watson distributions model in-plane and out-of-plane fibres for any given ROI, with equal likelihood. Consequently, while the proposed method is suitable for our application, for alternative applications that look to explicitly model individual tracts and distinguish them from their neighbours, additional anatomical constraints would be necessary. This is particularly true when modelling strictly sheet-like structures as found in the heart for example.

Registration of hybrid point sets comprising positions and directional data distributed on a unit sphere (as in **Application 2** of interest in this chapter), is useful for a variety of clinical applications. These include — computer-assisted interventions and intra-operative guidance applications involving surface data, as in hip replacement surgery (Mittelstadt, 2002), liver surgery (Clements et al., 2008), neuro-surgery (Raabe et al., 2002), (Miga et al., 2003), etc.; registration of surface data obtained from C-arm CT systems and Kinect depth-cameras (Rausch et al., 2016), for full 3D knee surface reconstruction and motion correction, useful for studies investigating the effects osteoarthritis on the weight-bearing capacity of knees; registration of blood vessel geometries represented by centreline positions with associated direction vectors oriented along centrelines, and/or vessel radii, useful for a variety of surgical planning (Selle et al., 2002) and navigation applications (Lange et al., 2009), (Hayashi et al., 2016), among others.

5.2 Methods

5.2.1 Application 1: Pre-processing

MR-DWIs were acquired for 60 subjects (20 AD, 20 MCI, 20 HC), as part of the prospective cohort, for the VPH-DARE@IT project (`vph-dare.eu`). All images used in this study were acquired using identical protocols: 2 diffusion-weighted b-values, with diffusivity gradients applied along 32 directions; image size of $(240 \times 240 \times 120)$ slices, $2.5mm$ thick in the right-left, anterior-posterior and inferior-superior directions, respectively. DTIs were estimated from these for each subject using TORTOISE v 2.5.0 (Pierpaoli et al., 2010), which employs state-of-the-art algorithms for motion and eddy current correction, correcting

B0 susceptibility induced EPI distortions and B-matrix re-orientation artefacts. Tensor-fitting was then achieved using iRESTORE (Chang, Walker, and Pierpaoli, 2012), based on non-linear iterative least-squares. TORTOISE registers each subject's DWIs to their corresponding T2-weighted structural MRI during the aforementioned pre-processing steps. As the latter were acquired at resolutions of $(1.5\times1.5\times1.5mm)$, all estimated DTIs (and correspondingly, DTI-derived images) were up-sampled relative to their raw DWIs. Finally, tensor-derived measures such as the eigenvector and fractional anisotropy images were also estimated using TORTOISE.

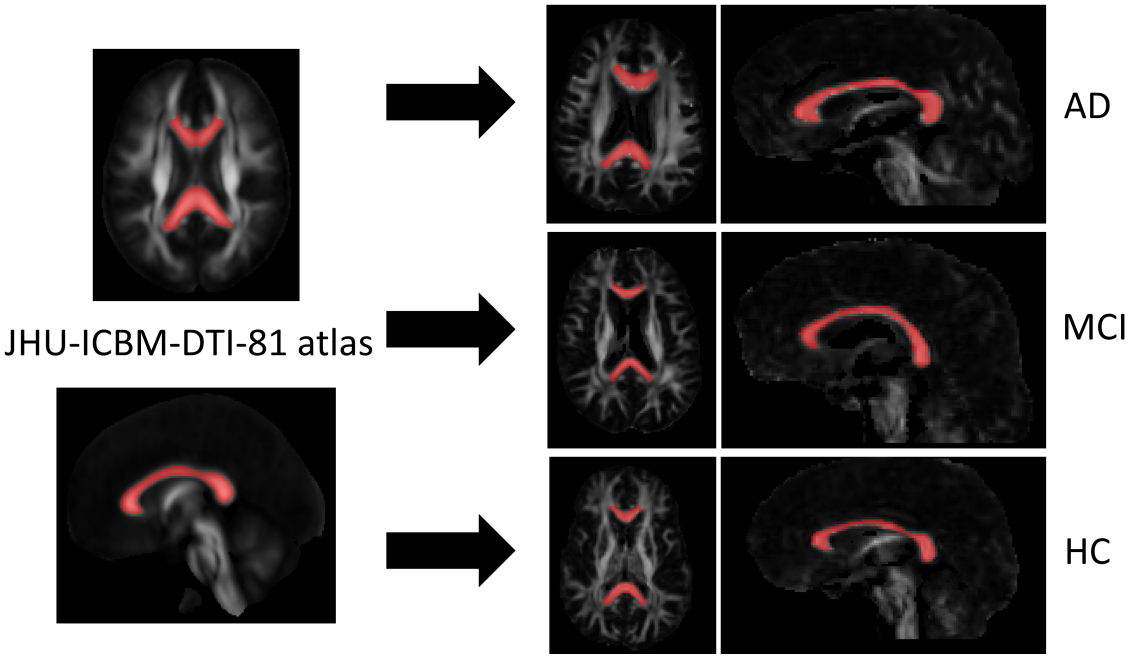

FIGURE 5.1: Nifty-Reg used to propagate labels for WM regions of interest from JHU-ICBM-DTI-81 atlas to each subject in AD, MCI and HC groups. Images depict propagation of the corpus callosum label from the atlas to subjects in AD, MCI and control groups.

The proposed framework is flexible and can consider the entire WM volume as the region of interest, though at the cost of significant computational burden. For the purpose of this study, we restrict our attention to two WM regions, namely, the cingulum and corpus callosum. An atlas-based label propagation approach was used to segment the WM ROIs from all subjects' FA images. The fractional anisotropy image of the JHU-ICBM-DTI-81 atlas [1] (Mori et al., 2008) - (Hua et al., 2008) was non-rigidly registered to each subject's FA image (following an initial affine alignment), using Nifty-Reg v 1.3.9 (Ourselin et al., 2001),

[1] Available at: http://www.loni.usc.edu/ICBM/Downloads/Downloads_DTI-81.shtml

(Modat et al., 2010), a deformable image registration algorithm based on cubic B-splines. Following FA image registration, the segmented labels for the cingulum and corpus callosum defined on the atlas (available along with the FA atlas), were resampled to the space of each subject's FA image. In this way, labels delineating the cingulum and corpus callosum in the atlas image, were propagated to each subject's image, segmenting the ROIs (as illustrated in Fig. 5.1).

5.2.2 Application 1: Algorithm Overview

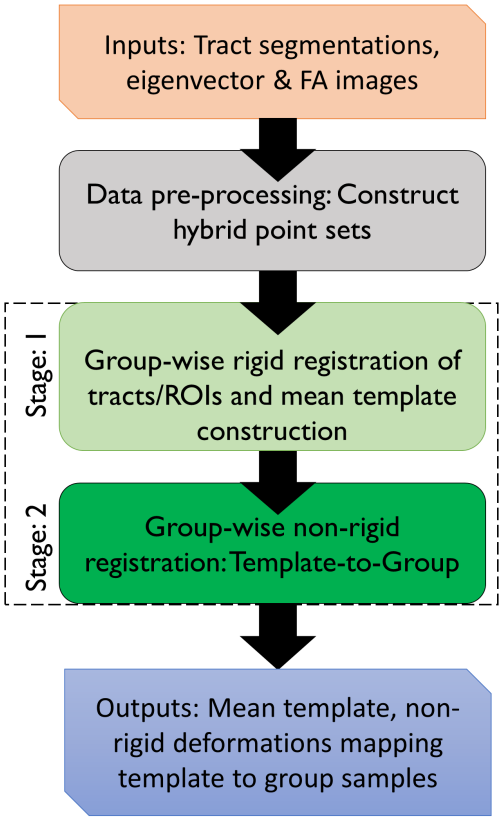

FIGURE 5.2: Summary of steps involved in the proposed framework to jointly register and cluster hybrid point sets comprising spatial positions, fibre orientations and FA values, for a WM tract/ROI. Dashed box outlines the two stages of the proposed algorithm.

The steps involved in the proposed approach are summarised by Fig. 5.2. For a group of $k = 1...K$ subjects to be analysed (e.g. comprising control, MCI and AD sub-groups), their tract segmentations, eigenvector and FA images were used to construct hybrid point sets $\mathbf{D}_k$, where each data point is a 7-dimensional vector denoted as $\mathbf{d}_{ki} = [\mathbf{x}_{ki}, \mathbf{n}_{ki}, f_{ki}]$. Here $\mathbf{x}_{ki}$ represents the spatial co-ordinate, $\mathbf{n}_{ki}$

represents the primary diffusion eigenvector and f_{ki} denotes the FA value for the i^{th} voxel, in the k^{th} subject's image. $\mathbf{x}_{ki}$ are consequently, densely distributed points within the volumes/ROIs. The resulting hybrid point sets were, subsequently, jointly registered and clustered by fitting an M-component hybrid mixture model (comprising Student's t, Watson and Gaussian distributions) to the data. This was achieved over two stages (as depicted in Fig. 5.2): (1) Group-wise rigid registration of the hybrid point sets $\mathbf{D}_k$ and mean template $\mathbf{M}$ construction; and (2) Group-wise non-rigid registration, wherein the mean template estimated in stage 1 was non-rigidly registered to each sample in a subject group. The set of similarity transformations $\mathbf{T}_k$ estimated in stage 1, aligning the hybrid point sets to the estimated mean template, initialise the subsequent non-rigid registration step (stage 2) by correcting global pose differences across the data set. Stage 2 of the algorithm estimates non-rigid transformations defined by basis function weights $\mathbf{W}_k$, mapping the mean template to each sample within a subject group. In both stages of the algorithm, estimation of the desired registration parameters was accompanied by the joint clustering of positions, orientations and FA values. The parameters to be estimated for each of the $j = 1...M$ components of the hybrid mixture model include: $\{\mathbf{m}_j^p, \sigma_p^2, \nu_j\} = \Theta_p$, which represent mean spatial positions, their variance and the degrees of freedom, respectively, for the Student's t-distributions; $\{\mathbf{m}_j^d, \kappa_j\} = \Theta_n$, which represent the mean fibre orientations and concentration around the means, respectively, for the Watson distributions; $\{m_j^f, \sigma_f^2\} = \Theta_f$, which denote the mean FA values and FA variance, respectively, for the Gaussian distributions; and π_j which denote the mixture coefficients. The estimated mean template $\mathbf{M}$ thus comprises positions, $\mathbf{m}_j^p$, orientations $\mathbf{m}_j^d$ and FA values m_j^f.

5.2.3 Joint Probabilistic Model of Position, Orientation and Anisotropy

The problem of joint registration and clustering of hybrid point sets comprising, multiple data features such as positions, orientations and scalar measures, is formulated as one of maximum likelihood estimation, using a hybrid mixture model (HMM). In the context of **Application 1**, the proposed HMM is used to approximate the joint *PDF* of spatial positions (of voxel centroids), fibre orientations, and fractional anisotropy, derived from DTIs. By assuming voxel positions, fibre orientations, and FA values to be independent and identically distributed (i.i.d), for each subject and across multiple subjects, the joint *PDF* can be approximated as a

product of the individual conditional densities (Bishop, 2006) for position, orientation and FA. Consequently, by considering all data points $\mathbf{d}_{ki} = \mathbf{D}_k$, from all K subjects, to be i.i.d. the conditional probability of an observation being sampled from an M-component hybrid mixture model is given by equation 5.1a. Θ_p represents the set of model parameters associated with the Student's t-distributions $\mathcal{S}$, used to model the distribution of voxel spatial positions; Θ_n represents the parameters of Watson distributions $\mathcal{W}$ (modelling fibre orientations); Θ_f denotes the set of parameters of the Gaussian distributions $\mathcal{N}$ (modelling FA); and $\pi_j = \Pi$ represents the set of mixture coefficients, of the hybrid mixture model. Here and throughout, subscript $j = 1...M$ denotes mixture components and the choice of distributions indicated earlier will be justified later in this Section. Using equation (5.1a) the log-likelihood function is formulated as shown in equation (5.1b), which defines the cost function to be optimised with respect to the mixture model parameters $\{\Theta_p, \Theta_n, \Theta_f, \Pi\} = \Psi$, to jointly register and cluster the hybrid point set data $\mathbf{D}_k = \mathbb{D}$.

$$p(\mathbf{d}_{ki}|\Theta_p, \Theta_n, \Theta_f) = \sum_{j=1}^{M} \pi_j \mathcal{S}(\mathbf{x}_{ki}|\Theta_p)\mathcal{W}(\mathbf{n}_{ki}|\Theta_n)\mathcal{N}(f_{ki}|\Theta_f) \tag{5.1a}$$

$$\ln p(\mathbb{D}|\Psi) = \sum_{k=1}^{K}\sum_{i}^{N_k} \ln p(\mathbf{d}_{ki}|\Theta_p, \Theta_n, \Theta_f) \tag{5.1b}$$

$$P_{kij}^t = \frac{\pi_j p(\mathbf{d}_{ki}|\Theta_p^t, \Theta_n^t, \Theta_f^t)}{\sum_{j=1}^{M} \pi_j p(\mathbf{d}_{ki}|\Theta_p^t, \Theta_n^t, \Theta_f^t)} \tag{5.1c}$$

$$Q(\Psi^{t+1}|\Psi^t) = \sum_{k=1}^{K}\sum_{i=1}^{N_k}\sum_{j=1}^{M} P_{kij}^t \Big[\ln \pi_j + Q(\Theta_{p_j}^{t+1}|\Theta_{p_j}^t) + Q(\Theta_{n_j}^{t+1}|\Theta_{n_j}^t) + Q(\Theta_{f_j}^{t+1}|\Theta_{f_j}^t) \Big] \tag{5.1d}$$

A tractable approach to maximising equation 5.1b is achieved using the expectation-maximisation (EM) framework (Dempster, Laird, and Rubin, 1977), which iteratively alternates between: the expectation (E)-step, which evaluates the mixture component membership probabilities as shown in equation 5.1c (i.e. posterior probabilities P_{kij}^t), given an estimate of the model parameters Ψ^t, at the t^{th} EM-iteration; and the maximisation (M)-step, which uses the computed posterior probabilities P_{kij}^t to maximise the conditional expectation of the complete-data-log-likelihood function Q (refer to equation 5.1d), with respect to each model

parameter, resulting in revised estimates Ψ^{t+1}. As shown in equation 5.1d, Q for the hybrid mixture model can be expressed as a sum of contributions from each distribution and corresponding data feature (i.e. position, orientation and FA), denoted: $Q(\Theta_p^{t+1}|\Theta_p^t), Q(\Theta_n^{t+1}|\Theta_n^t), Q(\Theta_f^{t+1}|\Theta_f^t)$, respectively. The complete algorithm for the proposed hybrid mixture model, to jointly register and cluster a group $\mathbb{D}$ of hybrid point sets, is summarized in Algorithm 3. Subsequent sections discuss each probability distribution and estimation of their associated parameters, within the proposed framework, in more detail.

Algorithm 3 Hybrid Mixture Model: HMM

`Inputs:` Group of hybrid point sets $\mathbf{D}_{k=1..K}$, number of mixture components M, max.iterations

`Outputs:` Set of HMM parameters $\{\Theta_p, \Theta_n, \Theta_f\} = \Psi$, soft correspondences

`INITIALIZATION`
Initialize $\mathbf{M}, \sigma_p^2, \sigma_f^2$ using K-means clustering.
All π_j = 1/M and $\nu_j = 3.0$, $\kappa_j = 1.0$
procedure STAGE 1 EM: GROUP-WISE RIGID REGISTRATION($\mathbf{D}_k, \Theta_p, \Theta_n, \Theta_f, \Pi, \mathbf{T}_k$) ▷ EM initialized
  while `Iteration` < `max.iterations` **do**
    Compute P_{kij} ▷ E-step
    Update $\mathbf{R}_k, s_k, \mathbf{t}_k$ ▷ M-step
    Update $\Theta_p, \Theta_n, \Theta_f$ ▷ M-step
  end while
  return $\mathbf{M}, \sigma^2, \Upsilon, \Pi, \mathbf{T}_k$
end procedure
Estimated mean template $\mathbf{M}$, mixture coefficients Π and similarity transformations $\{\mathbf{T}_k\}_{k=1...K}$ initialise Stage 2.
procedure STAGE 2 EM: GROUP-WISE NON-RIGID REGISTRATION($\mathbf{D}_k, \Theta_p, \Theta_n, \Theta_f, \Pi, \mathbf{T}_k, \mathbf{W}_k$) ▷ EM non-rigid initialized
  while `Iteration` < `max.iterations` **do**
    Compute P_{kij} ▷ E-step
    Update $\mathbf{W}_k$ ▷ M-step
    Update $\sigma_p^2, \nu_j, \Theta_n, \Theta_f$ ▷ M-step
    $\mathbf{m}_j^p$ remain fixed.
  end while
  Soft correpondences established using, $P_{kij}, \Theta_p, \Theta_n, \Theta_f$, estimated following convergence.
  return Soft correspondences, $\Theta_p, \Theta_n, \Theta_f, \Pi, \mathbf{W}_k$
end procedure

Algorithm 3 is described in the context of **Application 1**. It was also employed for **Application 2**, with minor modifications such as: employing Fisher distributions (in place of Watson distributions) to model surface normal vectors, and omitting the GMM component in the HMM (used to model scalar-valued quantities).

5.2.4 Mixture Model for Axial Data: Primary Diffusion Axes

In addition to modelling the spatial distribution of voxels defining ROIs, the proposed approach also deals with axial data distributed over the S^2 sphere, i.e. fibre orientations defined by primary diffusion eigenvectors. Although Von-Mises-Fisher distributions are frequently used for clustering directional data, they are unsuitable for axial data, as they lack of antipodal symmetry. Watson distributions on the other hand, are naturally suited to model diffusion data as they are antipodally symmetric (i.e. the density is the same along an axis in either direction) and as the aim is to model the *PDF* of diffusion axes at corresponding spatial locations, rather than any specific direction along the axes (Jupp and Mardia, 1989). They are fully defined by two parameters, namely, the mean/principal axis ($\pm\mathbf{m}^d$, about which the distribution is rotationally symmetric) and a scalar concentration parameter κ. The latter describes the degree of concentration about the mean axis of the distribution, with high values indicating high concentration. The *PDF* of a Watson distribution with mean direction $\mathbf{m}^d$ and concentration κ is expressed as equation 5.2a, for axially symmetric 3D unit vectors $\pm\mathbf{n}$. Here, $M(\cdot)$ represents the Kummer function. (Bijral, Breitenbach, and Grudic, 2007) proposed an efficient EM-based clustering framework for axial data, using a WMM, employed in this chapter for **Application 1**, to cluster fibre orientations.

$$p(\pm\mathbf{n}|\mathbf{m}^d,\kappa) = M(\frac{1}{2},\frac{D}{2},\kappa)^{-1}\exp^{\kappa(\mathbf{m}^{dT}\mathbf{n})^2} \tag{5.2a}$$

$$p(\mathbb{N}|\Theta_n) = \sum_{k=1}^{K}\sum_{i=1}^{N_k}\ln\sum_{j=1}^{M}\pi_j p(\pm\mathbf{n}_{ki}|\mathbf{m}_j^d,\kappa_j) \tag{5.2b}$$

The joint likelihood of the diffusion eigenvectors $\pm\mathbf{n}_{ki} = \mathbf{N}_k$ observed across all N_k points in all K shapes, given Watson distributions with mean directions and concentrations $\{\mathbf{m}_j^d,\kappa_j\}_{j=1\ldots M} = \Theta_n$, is evaluated as shown in equation 5.2b. Here, $\mathbf{N}_k = \mathbb{N}$ denotes the set of all observed diffusion vectors across the entire population. It is important to note at this point that, as the clustering of fibre orientations was initially performed jointly with rigid registration of the hybrid point sets $\mathbf{D}_k$, the estimated rotations $\mathbf{R}_k$ at each EM-iteration, were applied to the current estimate of the mean fibre orientations $\mathbf{m}_j^d$, prior to the evaluation of the posterior probabilities P_{kij}, and concentrations κ_j, in the E- and M-steps, respectively (refer to equations 5.3a - 5.3b). Additionally, for the estimation of $\mathbf{m}_j^d$ the inverse of

the estimated rotations $\mathbf{R}_k^T$ were applied to their corresponding sample's diffusion eigenvectors $\mathbf{n}_{ki}$, to align the k^{th} sample to the current estimate of the mean template (refer to equation 5.3c).

$$Q(\Theta_n^{t+1}|\Theta_n^t) = \sum_{k=1}^{K}\sum_{i=1}^{N_k}\sum_{j=1}^{M} P_{kij}^{(t)} \ln p(\pm\mathbf{n}_{ki}|\mathbf{R}_k^{(t)}\mathbf{m}_j^{d^{(t)}}, \kappa_j^{(t)}) \tag{5.3a}$$

$$Q(\Theta_n^{t+1}|\Theta_n^t) = \sum_{k=1}^{K}\sum_{i=1}^{N_k}\sum_{j=1}^{M} [P_{kij}^{(t)} \ln p(\pm\mathbf{n}_{ki}|\mathbf{R}_k^{(t)}\mathbf{m}_j^{d}, \kappa_j) + \lambda_j(1 - \mathbf{R}_k^{(t)}\mathbf{m}_j^{dT}\mathbf{R}_k^{(t)}\mathbf{m}_j^{d})] \tag{5.3b}$$

$$\mathbf{m}_j^{d^{(t)}} - \frac{\sum_{k=1}^{K}\sum_{i=1}^{N_k} P_{kij}^{(t)}(\mathbf{R}_k^{T^{(t+1)}}\mathbf{n}_{ki}^T\mathbf{m}_j^{d^{(t)}})\mathbf{R}_k^{T^{(t+1)}}\mathbf{n}_{ki}}{||\sum_{k=1}^{K}\sum_{i=1}^{N_k} P_{kij}^{(t)}(\mathbf{R}_k^{T^{(t+1)}}\mathbf{n}_{ki}^T\mathbf{m}_j^{d^{(t)}})\mathbf{R}_k^{T^{(t+1)}}\mathbf{n}_{ki}||} = 0 \tag{5.3c}$$

$$\left[\frac{M'(\kappa_j)}{M(\kappa_j)}\right]^{(t+1)} = \frac{\sum_{k=1}^{K}\sum_{i=1}^{N_k} P_{kij}^{(t)}(\mathbf{n}_{ki}^T\mathbf{m}_j^{d^{(t+1)}})^2}{\sum_{k=1}^{K}\sum_{i=1}^{N_k} P_{kij}^{(t)}} \tag{5.3d}$$

$$\kappa_j^{(t+1)} \approx \frac{1}{2}\left[\frac{1 - [\frac{M'(\kappa_j)}{M(\kappa_j)}]^{(t+1)}D}{[(\frac{M'(\kappa_j)}{M(\kappa_j)})^2]^{(t+1)} - [\frac{M'(\kappa_j)}{M(\kappa_j)}]^{(t+1)}}\right] \tag{5.3e}$$

Maximum likelihood estimates for the associated parameters are evaluated at each M-step of the algorithm by maximising the expectation of the complete data likelihood (equation 5.3a), with respect to $\mathbf{m}_j^d$ and κ_j, subject to the constraint $\mathbf{m}_j^{dT}\mathbf{m}_j^d = 1$ (Bijral, Breitenbach, and Grudic, 2007). This is achieved by maximising the Lagrangian form of Q shown in equation 5.3b. Mean directions $\mathbf{m}_j^d$ are estimated numerically, using fixed-point iteration, to solve the non-linear equation (shown in equation 5.3c) obtained from differentiating Q (5.3b) with respect to $\mathbf{m}_j^d$. κ_j on the other hand is approximated (refer to equation 5.3e) using the continued fraction representation for the ratio of, the derivative of the Kummer function and the function itself, i.e. $\frac{M'(\kappa_j)}{M(\kappa_j)}$ (equation 5.3d). In a recent study (Sra and Karp, 2013) derived two-sided bounds for approximating κ, particularly useful when dealing with high dimensional data. However, for 3D data (as in this study) the approximation presented in equation 5.3e is sufficient (as noted by (Bijral, Breitenbach, and Grudic, 2007),(Sra and Karp, 2013)). Better approximations for κ_j may be obtained using numerical techniques such as Newton's method, however, at the expense of increase in computational burden. Derivations for all WMM parameters are presented in Appendix B.

5.2.5 Mixture Model for Directional Data: Surface Normals

Application 2 is concerned with modelling the joint *PDF* of point positions with associated surface normal vectors (which are consistently oriented either outward or inward). Such an approach is particularly useful when registering shapes with complex topologies comprising, disjoint structures, holes, bifurcations (encountered with blood vessel geometries), etc. Consistently oriented surface normal vectors represent directional data distributed over the S^2 sphere. GMMs and TMMs, comprising Gaussian and Student's t-distributions, respectively, are inappropriate for clustering such data and consequently, a mixture of Von-Mises-Fisher (or Fisher) distributions, also defined over the spherical domain, is employed here. Fisher distributions are rotationally symmetric, unimodal and from the general family of Langevin distributions (Jupp and Mardia, 1989). They are fully defined by two parameters, namely, the mean direction ($\mathbf{m}^d$, about which the distribution is rotationally symmetric) and a scalar concentration parameter κ, which is analogous to the precision of a Gaussian distribution. The latter describes the degree of concentration about the mean direction of the distribution. High values for κ thus indicate high concentration along the mean direction (Fisher, Lewis, and Embleton, 1987). A 3-D unit vector $\mathbf{n}$ is considered to be an observation sampled from a Fisher distribution with mean direction $\mathbf{m}^d$ and concentration κ if its *PDF* is expressed as shown in equation 5.4a.

$$p(\mathbf{n}|\mathbf{m}^d, \kappa) = \frac{\kappa}{4\pi \sinh(\kappa)} \exp^{\kappa \mathbf{m}^{dT} \mathbf{n}} \tag{5.4a}$$

$$p(\mathbb{N}|\Theta_n) = \sum_{k=1}^{K} \sum_{i=1}^{N_k} \ln \sum_{j=1}^{M} \pi_j p(\mathbf{n}_{ki}|\mathbf{m}_j^d, \kappa_j) \tag{5.4b}$$

$$Q(\Theta_n^{t+1}|\Theta_n^t) = \sum_{k=1}^{K} \sum_{i=1}^{N_k} \sum_{j=1}^{M} P_{kij}^t \ln p(\mathbf{n}_{ki}|\mathbf{m}_j^d, \kappa_j) \tag{5.4c}$$

With GMMs and TMMs the error measure relating the observed data to cluster centroids are defined using the Mahalanobis distance. This results in less accurate estimates than the cosine similarity measure, used by Fisher mixture models (FMMs), when dealing with directional data (Banerjee et al., 2005). FMMs are well-suited to model such data and were chosen for their simplicity and computational efficiency. In the context of **Application 2**, the observed surface normal

vectors $\mathbf{n}_{ki} = \mathbf{N}_k$, across a group of K shapes, are assumed to be rotated observations sampled from Fisher distributions with mean directions $\mathbf{m}_j^d$ and concentrations κ_j. The joint *PDF* for all observed normal vectors across the group (denoted $\mathbf{N}_k = \mathbb{N}$) is evaluated as shown in equation 5.4b.

$$Q(\Theta_n^{t+1}|\Theta_n^t) = \sum_{k=1}^{K}\sum_{i=1}^{N_k}\sum_{j=1}^{M}[P_{kij}^t \ln p(\mathbf{n}_{ki}|\mathbf{m}_j^d, \kappa_j) + \lambda_j(1 - \mathbf{m}_j^{dT}\mathbf{m}_j^d)] \tag{5.5a}$$

$$\mathbf{m}_j^{d(t+1)} = \frac{\sum_{k=1}^{K}\sum_{i=1}^{N_k} P_{kij}^{(t)}\mathbf{n}_{ki}}{||\sum_{k=1}^{K}\sum_{i=1}^{N_k} P_{kij}^{(t)}\mathbf{n}_{ki}||} \tag{5.5b}$$

$$\frac{1}{\kappa_j^{t+1}} = \coth(\kappa_j^t) - \mathbf{m}_j^{dT}\frac{\sum_{k=1}^{K}\sum_{i}^{N_k} P_{kij}^{(t)}\mathbf{n}_{ki}}{\sum_{k=1}^{K}\sum_{i}^{N_k} P_{kij}^{(t)}} \tag{5.5c}$$

Maximum likelihood estimates for the associated parameters are evaluated at each M-step of the algorithm by maximising the form of Q shown in equation 5.5a, with respect to $\mathbf{m}_j^d$ and κ_j. While estimates for $\mathbf{m}_j^d$ are derived analytically, similarly to (Banerjee et al., 2005), no such solution exists for estimating concentrations κ_j. Previous approaches employing FMMs have proposed empirically determined approximations (Banerjee et al., 2005) and/or adopted numerical estimation techniques. In this study we use fixed point iteration to solve the non-linear equation (refer to equation 5.5c) resulting from differentiating $Q(\Theta_n^{t+1}|\Theta_n^t)$ with respect to κ_j and equating to zero. As with WMMs discussed in the previous section, $\mathbf{m}_j^d$ are estimated by optimising $Q(\Theta_n^{t+1}|\Theta_n^t)$ subject to the constraint that the mean directions should be of unit norm i.e. $||\mathbf{m}_j^d|| = 1$. This is achieved using a Lagrange multiplier λ_j and maximising the Langrangian form of Q presented in equation 5.5a, with respect to $\mathbf{m}_j^d$. Revised estimates for the mean directions $\mathbf{m}_j^d$ are thus evaluated at each M-step of the algorithm, as shown in equation 5.5b. Derivations for all FMM parameters are presented in Appendix B.

5.2.6 Mixture Model for Fractional Anisotropy

The distribution of voxel-wise FA in WM ROIs across a population, is modelled using a univariate GMM. GMM was chosen as the resulting model-predicted FA values at the estimated soft-correspondences, across subjects, is guaranteed to be normally distributed — a useful property for subsequent statistical analyses,

as noted in (Smith et al., 2006). Additionally, GMMs are computationally efficient, as analytical solutions exist for revising estimates of the associated model parameters (mean m_j^f and variance σ_f^2 of FA), at each EM-iteration. Assuming the observed FA values f_{ki} at voxels in ROIs, across a group of subjects $\mathbf{F}_k = \mathbb{F}$ are i.i.d, the joint log-likelihood $\ln p(\mathbb{F}|\Theta_f)$, is expressed as equations 5.6a, 5.6b. Consequently, the conditional expectation of the complete data log likelihood Q, maximised with respect to the model parameters associated with the Gaussian distributions in the mixture, is given by equation 5.6c (only terms dependent on m_j^f and σ_f^2 are retained in Q). As GMM-based clustering of FA values is performed jointly with the registration of tract shapes, and clustering of voxel positions and the associated fibre orientations, the influence of a Gaussian component in the mixture model is automatically limited to its local neighbourhood. This helps ensure that only voxels in close proximity to each other contribute significantly to the estimation of mean FA values at each mixture component. Estimates for the GMM parameters m_j^f and σ_f^2 in the M-step of the algorithm are derived analytically, as shown in (Bishop, 2006).

$$p(\mathbf{F}_k|m_j^f, \sigma_f^2) = \prod_{i=1}^{N_k} \sum_{j=1}^{M} \pi_j \mathcal{N}(f_{ki}|m_j^f, \sigma_f^2) \tag{5.6a}$$

$$\ln p(\mathbb{F}|\Theta_f) = \sum_{k=1}^{K} \ln p(\mathbf{F}_k|\Theta_f) \tag{5.6b}$$

$$Q(\Theta_f^{t+1}|\Theta_f^t) = -\frac{1}{2} \sum_{k=1}^{K} \sum_{i=1}^{N_k} \sum_{j=1}^{M} P_{kij}^t \Big[\frac{(f_{ki} - m_j^f)^2}{\sigma_f^2} \Big] \tag{5.6c}$$

5.2.7 Rigid Alignment and Template Construction

5.2.7.1 Application 1: Modelling Diffusion Data

The group-wise rigid point set registration framework based on Student's t-mixture model, proposed in **chapter** 3 is employed in the present study as an initial step, to rigidly align WM ROIs (hybrid point sets representing voxel centroid positions, fibre orientations and FA values), segmented from all subjects' images, whilst simultaneously estimating a mean model. The latter is used subsequently as a template for non-rigid registration (using TMM-NR, also discussed in **chapter** 3). Rigid group-wise registration is preferred to a pair-wise approach

as it enables estimation of a mean template and the desired similarity transformations in an unbiased manner. Rigid alignment also helps initialise the subsequent non-rigid registration by recovering global differences in pose between samples, and establishes soft correspondences across subjects.

The joint *PDF* of voxel positions $\mathbf{x}_{ki} = \mathbf{X}_k$, fibre orientations $\mathbf{n}_{ki} = \mathbf{N}_k$, and FA $\mathbf{f}_{ki} = \mathbf{F}_k$, across all K subjects in a group (denoted, $\mathbf{X}_k = \mathbb{X}$, $\mathbf{N}_k = \mathbb{N}$, $\mathbf{F}_k = \mathbb{F}$), is given by equation 5.7a (assuming they are i.i.d transformed observations of a HMM). In equation 5.7a, $\mathbf{T}_k$ represents the similarity transformation (comprising rotation $\mathbf{R}_k$, scaling s_k and translation $\mathbf{b}_k$), to align the positions $\mathbf{m}_j^p$ defining the mean template, to the k^{th} sample in the group. The form of the objective function Q to be maximised, to estimate the desired similarity transformations $\mathbf{T}_k = \mathbb{T}$ and mixture component parameters Θ_p, is given by equation 5.7b, as discussed in **chapter** 3. Fibre orientations and FA are invariant to translation $\mathbf{b}_k$ and scaling s_k, consequently, these transformation parameters are estimated identically as in **chapter** 3. Although the former are rotationally dependent, the contribution of orientation to the estimation of $\mathbf{R}_k$ is ignored, as the directions of diffusion eigenvectors tend to be random, leading to ambiguity in the estimation of $\mathbf{R}_k$. Consequently, positions alone contribute to recovering rotational offsets across samples. $\mathbf{R}_k$ is thus derived based on the spatial positions of the hybrid point sets alone (as shown in equation 5.7b). However, following estimation of the desired rotations $\mathbf{R}_k$ at each EM-iteration, the current estimate of the mean template is transformed by rotating both spatial positions $\mathbf{m}_j^p$ and their associated fibre orientations $\mathbf{m}_j^d$, to align it with the k^{th} sample in the group. Additionally, it is important to note that, while the fibre orientations and FA values are ignored in the derivation of the desired transformation parameters, they are intrinsic to the estimation of the posterior probabilities P_{kij} at each E-step of the algorithm. Consequently, they drive the estimation of soft correspondences, which in turn affect the transformations evaluated at each M-step of the algorithm.

$$\ln p(\mathbb{X}, \mathbb{N}, \mathbb{F}|\Theta_p, \Theta_n, \Theta_f, \mathbb{T}) = \sum_{k=1}^{K}\sum_{i=1}^{N_k} \ln \sum_{j=1}^{M} [\pi_j \mathcal{S}(\mathbf{x}_{ki}|\mathbf{T}_k(\mathbf{m}_j^p), \sigma_p^2, \nu_j) \mathcal{W}(\mathbf{n}_{ki}|\Theta_{n_j}) \mathcal{N}(f_{ki}|\Theta_{f_j})] \tag{5.7a}$$

$$Q(\Theta_p^{t+1}, \Theta_n^{t+1}, \Theta_f^{t+1}, \mathbb{T}^{t+1}|\Theta_p^t, \Theta_n^t, \Theta_f^t, \mathbb{T}^t) = -\frac{1}{2}\sum_{k=1}^{K}\sum_{i=1}^{N_k}\sum_{j=1}^{M} P_{kij}^{\star t} \|\mathbf{x}_{ki} - s_k\mathbf{R}_k\mathbf{m}_j^p - \mathbf{b}_k\|^2 \tag{5.7b}$$

5.2.7.2 Application 2: Modelling Surface Normals

As discussed in the previous section, group-wise rigid registration of hybrid point sets is achieved using the EM-based framework outlined in **chapter** 3. While the Watson-variant of the proposed HMM, used to model axial data, ignores the contribution of orientations to the estimation of rotations, this is not the case for its Fisher distribution-based counterpart. In the context of the **Application 2**, as the directional data (surface normal vectors) modelled is consistently oriented, and rotationally dependent, estimation of the desired rotations is driven by both spatial positions and their associated surface normal vectors. Consequently, the joint *PDF* of spatial positions $\mathbf{x}_{ki} = \mathbf{X}_k$ and their associated normals $\mathbf{n}_{ki} = \mathbf{N}_k$, across K shapes in a group (denoted, $\mathbf{X}_k = \mathbb{X}$ and $\mathbf{N}_k = \mathbb{N}$), is given by equation 5.8a. Correspondingly, the form of Q to be maximised, to estimate the desired similarity transformations $\mathbf{T}_k = \mathbb{T}$ and mixture component parameters Θ_p, Θ_n, is given by equation 5.8b. A similar approach to estimating rotations based on both positions and surface normals was presented in (Billings and Taylor, 2014) and (Billings and Taylor, 2015), although for pair-wise shape registration.

$$\ln p(\mathbb{X}, \mathbb{N}|\Theta_p, \Theta_n, \mathbb{T}) = \sum_{k=1}^{K}\sum_{i=1}^{N_k} \ln \sum_{j=1}^{M} \pi_j \mathcal{S}(\mathbf{x}_{ki}|\mathbf{T}_k(\mathbf{m}_j^p), \sigma_p^2, \nu_j)\mathcal{F}(\mathbf{n}_{ki}|\mathbf{R}_k(\mathbf{m}_j^d, \kappa_j)) \tag{5.8a}$$

$$\begin{aligned} &Q(\Theta_p^{t+1}, \Theta_n^{t+1}, \mathbb{T}^{t+1}|\Theta_p^t, \Theta_n^t, \mathbb{T}^t) = \\ &-\frac{1}{2}\sum_{k=1}^{K}\sum_{i}^{N_k}\sum_{j=1}^{M} P_{kij}^{\star t}\|\mathbf{x}_{ki} - s_k\mathbf{R}_k\mathbf{m}_j^p - \mathbf{b}_k\|^2 + \sum_{k=1}^{K}\sum_{i=1}^{N_k}\sum_{j=1}^{M}\kappa_j(\mathbf{R}_k\mathbf{m}_j^d)^T\mathbf{n}_{ki} \end{aligned} \tag{5.8b}$$

$$\texttt{Rotation} : \mathbf{R}_k^{(t+1)} = \mathbf{U}\mathbf{S}\mathbf{V}^T \tag{5.8c}$$

$$\mathbf{C}_k^{(t+1)} = \sum_{i=1}^{N_k}\sum_{j=1}^{M} P_{kij}^{\star(t)}[(\mathbf{x}_{ki} - \mathbf{d}_k^{(t+1)})(\mathbf{m}_j^p - \mathbf{m}_k^{(t+1)})^T + (\mathbf{n}_{ki}\mathbf{m}_j^{dT})] \tag{5.8d}$$

As unit vectors are invariant to translation $\mathbf{b}_k$ and scaling s_k, these transformation parameters are estimated identically as in **chapter** 3. Rotations meanwhile, are computed by maximising Q (equation 5.8b) with respect to $\mathbf{R}_k$, and expressed as shown in equation 5.8c. In equation 5.8c $\mathbf{U}$,$\mathbf{V}$ are unitary matrices estimated by singular value decomposition of matrix $\mathbf{C}_k$, described by equation 5.8d, and $\mathbf{S}$ is

a diagonal matrix given by, $\mathbf{S} = diag(1, 1, det(\mathbf{UV}^T))$ enforcing strictly orthogonal rotations, as discussed in **chapter** 3. Additionally, $\mathbf{d}_k$ and $\mathbf{m}_k$ represent weighted centroids/barycenters evaluated as described previously in equations 3.18 - 3.19.

5.2.8 Non-rigid Registration

The mean shape/template estimated during the initial group-wise rigid registration step (discussed in section 5.2.7), is non-rigidly registered to each patient group (AD, MCI and HC) independently (in the context of **Application 1**). As discussed previously in **chapter** 3, the desired non-rigid transformations are defined with respect to the template M as: $\mathbf{M}+v^k(\mathbf{M})$ (considering spatial positions $\mathbf{m}_j^p$ alone), where v is a displacement function mapping the template to the k^{th} sample in the group. To register the template to the k^{th} sample in each group, the objective function to be maximised with respect to the basis function weights $w_{kj} = \mathbf{W}_k$, is expressed as shown in equation 5.9, where $\mathbf{G}$ represents the Gaussian kernel/Gram matrix. The basis function weights to register the mean template to each sample in a patient group, are estimated similarly to (Myronenko and Song, 2010).

$$\begin{aligned} &Q(\Theta_p^{t+1}, \Theta_n^{t+1}, \Theta_f^{t+1}, \mathbf{W}_k^{t+1} | \Theta_p^t, \Theta_n^t, \Theta_f^t, \mathbf{W}_k^t) = \\ &-\frac{1}{2\sigma_p^2} \sum_i^{N_k} \sum_j^M P_{kij}^{\star t} \|\mathbf{x}_{ki} - (\mathbf{m}_j^p + v^k(\mathbf{m}_j^p))\|^2 + \frac{\lambda}{2} \mathbf{W}_k^T \mathbf{G} \mathbf{W}_k \end{aligned} \tag{5.9}$$

During the non-rigid registration step, the spatial positions of the template remain fixed and are not updated in the M-step of the algorithm. As a result the mean tract shape (representative of the entire population), estimated in the group-wise rigid registration step of the algorithm, is retained. This is particularly useful for performing subsequent inter-group comparisons (similar to the role of a mean FA skeleton in TBSS), to identify corresponding spatial positions, which exhibit significant changes in FA. However, the remaining parameters of the mixture model, are revised at each M-step of the algorithm. Consequently, following convergence of the non-rigid registration, a group-specific estimate for the mean fibre orientation and mean FA value at each point representing the template is obtained. Although point set registration techniques are typically employed to register 3D point sets (comprising only spatial positions) representing the surface/boundary of an object, this study incorporates additional image-based features (such as fibre orientations and FA values), that enable registration of dense

point sets, defined by voxel centroids located at the boundary of, and within a region of interest.

Non-rigid transformations are estimated in a similar manner for the Fisher-variant of the HMM, employed in **Application 2**, to register hybrid point sets defining surface boundaries (comprising spatial positions and associated surface normals). However, the spatial positions of the mean template are revised at each EM-iteration in this case, conversely to its Watson distribution-based counterpart, used in **Application 1**.

5.3 Application 1: Results and Discussion

5.3.1 Rigid Registration Accuracy

Rigid registration accuracy of the proposed framework and the robustness of Student's t-distributions to outliers is assessed using synthetic data comprising point sets containing positions, associated fibre orientations and FA values. The synthetic data set was generated by rigidly transforming a corpus callosum hybrid point set by varying amounts. Four distinct synthetic samples (Samples 1-4) were generated in this manner from the original ground truth point set (referred to as Sample 0), as illustrated by Fig. 5.3.

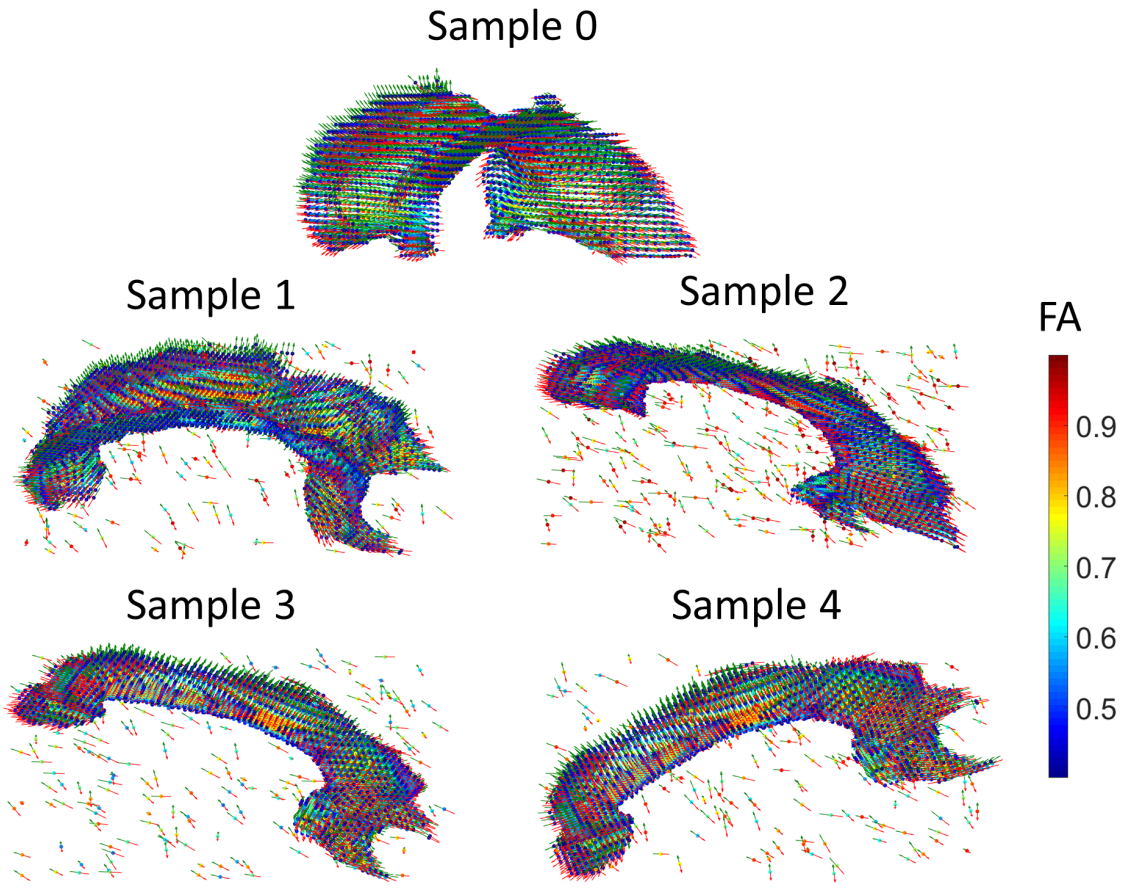

FIGURE 5.3: Synthetic corpus callosum data set comprising: Sample (0), the ground truth hybrid point set; and Samples (1-4), which are rotated and modified versions of Sample 0.

The rigidly transformed point sets were also modified by the addition of varying proportions of random outliers (comprising positions, orientations and FA values). Fibre orientations associated with the outliers were generated by normalizing uniformly sampled 3D points and similarly, FA values were also uniformly sampled within the range $[0.2 - 0.8]$. The FA values associated with the voxels of each modified hybrid point set were also varied by ± 0.1, relative to the ground truth point set. This was necessary in order to emulate real data as FA values typically vary at corresponding anatomical locations, between subjects. This process was repeated 10 times, to generate 10 unique synthetic data sets (each comprising one ground truth and 4 modified, unique samples), which were subsequently rigidly aligned using the proposed Watson-distribution based HMM algorithm. Random rotations and proportions of outliers were generated for each experiment, within the range of -30° to 30° and 2% to 5%, respectively. Table 5.1 summarises the translations, and the axes about which rotations were

applied to generate each sample in each experiment. The average rigid registration errors following alignment of the synthetic data sets (with $M = 2000$ mixture components) using the proposed framework are also reported in Table 5.1.

Rigid registration accuracy was evaluated by — (a) computing the intrinsic distance between the estimated and ground truth rotations (Huynh, 2009), as discussed previously in **chapter** 3 (refer to equation 3.22b); and (b) computing the mean Euclidean distance (ED) between (transformed) samples 1-4 and sample 0 (averaged across all points); Table 5.1 summarises average rotation and Euclidean distance errors (computed across all 10 experiments). Point-wise Euclidean distances are first evaluated between each modified sample (samples 1-4) and sample 0, and subsequently averaged across all points. The resulting mean Euclidean distance is then averaged once again across all 10 experiments and is reported in Table 5.1.

TABLE 5.1: Summary of rigid registration errors across 10 experiments using synthetic corpus callosum data set.

Sample #	**Rotated Around**	**Translations (mm.)**	**Rotation Error (degrees)**	**Euclidean Dist. (mm.)**
1	x,y	x=0.5 y=-0.4 z=0.6	0.06 ± 0.03	0.34 ± 0.15
2	y,z	x=0.4 y=0.3 z=0.5	0.05 ± 0.03	0.30 ± 0.16
3	z,x	x=0.6 y=0.2 z=-0.5	0.04 ± 0.03	0.23 ± 0.13
4	x,y,z	x=-0.2 y=-0.7 z=0.4	0.04 ± 0.03	0.25 ± 0.17

The average Euclidean distance errors reported in Table 5.1 indicate that the proposed Watson-based HMM framework achieved very low errors (despite the presence of random outliers) as all values are substantially lower than the voxel size of the original eigenvector and FA image (refer to section 5.2.1), from which the ground truth corpus callosum hybrid point set (sample 0) was generated. Robustness to outliers may be attributed to the constituent t-distributions in the HMM, modelling spatial positions. Similarly the proposed approach was also able to accurately recover the applied ground truth rotations, resulting in very

low rotation errors for all samples (as shown in Table 5.1), relative to the magnitude of the rotations applied to generate the synthetic data set. The proposed approach therefore, is inferred to successfully approximate the joint density of position, fibre orientation and FA, for the synthetic corpus callosum data set.

5.3.2 Model Quality

The quality of the Watson-based HMM to model DTI-derived quantities was assessed using clinical data, acquired from the VPH-DARE@IT prospective cohort, described in section 5.2.1. Specifically, model quality was quantified by evaluating the similarity between the estimated correspondences (resulting from non-rigidly registering the template to each sample in the group) and the nearest neighbour voxels in the corresponding subject's ground truth FA and eigenvector images. FA accuracy is quantified as the root mean-squared error (RMSE) between the model-predicted and ground truth FA values, across all correspondences, for each subject. However, these measures represent registration residuals which describe the quality of correspondences established by the proposed HMM (i.e. how well the HMM can model the observed DTI-derived data), and only indirectly reflect 'registration' accuracy. In order to provide a more general view of 'registration' accuracy, MSD measures (described in **chapter** 3) quantifying spatial position errors were also evaluated between the registered mean templates and their corresponding ground truth hybrid point sets (Note: here MSD values were evaluated between dense volumetric point sets). As discussed previously in section 5.1, correspondences established using the proposed approach are probabilistic in nature and consequently, reflect the DTI-derived quantities of voxels located in their local spatial neighbourhood. The group-wise average (for each subject group) of FA RMSE was subsequently computed. The minimum arc length (measured in radians) between two unit vectors is used to measure the accuracy of local fibre orientation in a similar manner. As discussed in section 5.2.4, the proposed framework models axial data rather than directional data. When computing fibre orientation errors, corresponding unit vectors between the model-predicted and ground truth eigenvectors are first identified. This is achieved by evaluating their scalar product and ensuring it is positive i.e. if the dot product is negative, the antipodal counterpart of the model-predicted vector is used instead. The resulting measure thus quantifies the angular error in fibre orientation between the model-predicted correspondences and the ground truth data, for each subject.

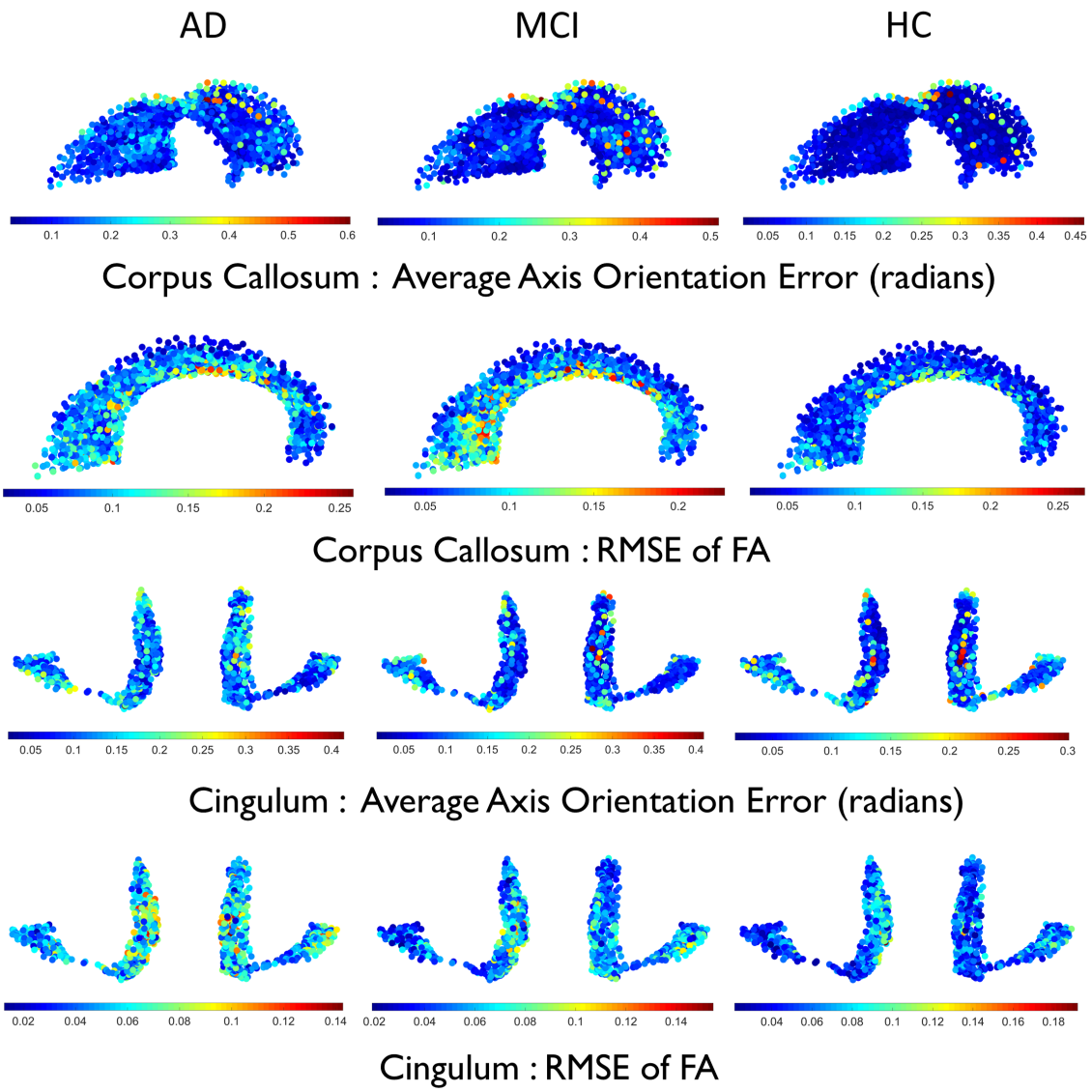

FIGURE 5.4: Model quality evaluated independently for AD, MCI and HC groups, using $M = 2000$ and $M = 1500$ mixture components, for the corpus callosum and cingulum respectively. Rows one and two: Angular errors for fibre orientations (in radians) and RMSE of FA for the corpus callosum; Rows three and four: Angular errors for fibre orientations (in radians) and RMSE of FA for the cingulum.

Results summarizing the ability of the proposed framework to model DTI-derived quantities across all 60 subjects, are presented in Fig. 5.4 and Fig. 5.7 and Tables 5.2 - 5.7. Fig. 5.4 helps to visualise the spatial distribution of mean registration errors across subjects within each patient group. Here, the RMSE values of FA were computed by averaging across subjects in each group, at each corresponding position (defined by the mean template). The depicted mean angular errors were also averaged across subjects, quantifying the fibre orientation

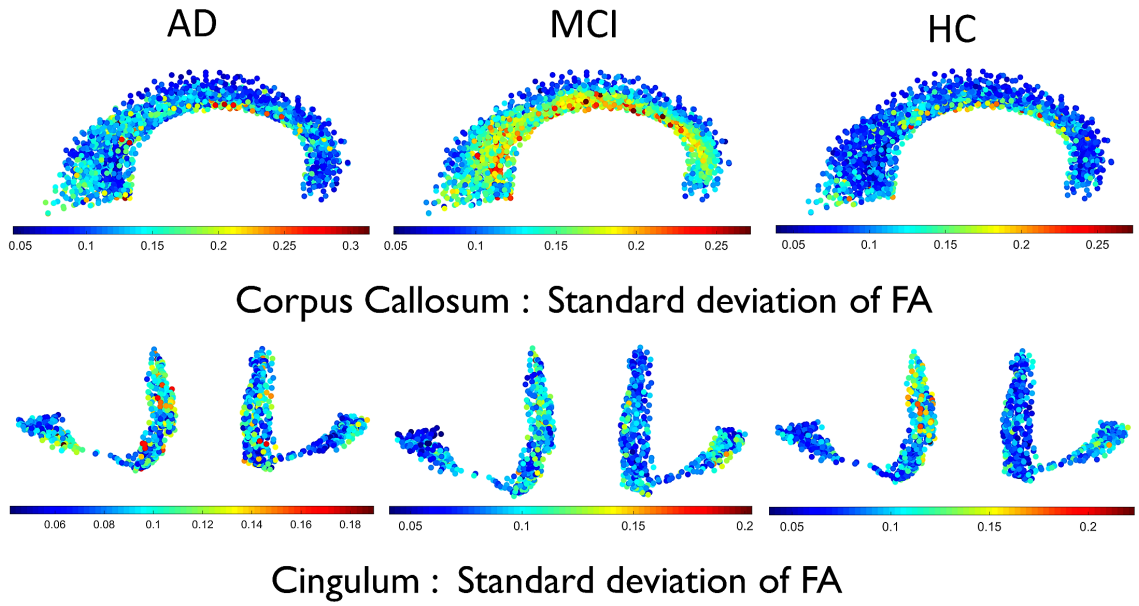

FIGURE 5.5: Standard deviation of FA computed across subjects in the AD, MCI and HC groups, mapped on to the mean templates estimated, using $M = 2000$ and $M = 1500$ mixture components for the corpus callosum and cingulum, respectively.

accuracy at each corresponding position. In order to interpret these results and provide a frame of reference, the standard deviation in FA across subjects for each patient group, is also presented in Fig. 5.5, for both WM regions. The spatial distribution of the variation in FA across subjects within each patient group, was evaluated as follows — (a) the nearest neighbour voxel in the original hybrid point sets were first identified based on the spatial positions estimated for each established correspondence point (for the corresponding sample); (b) the FA values associated with the voxels identified for each subject, were in turn used to compute the standard deviation about the mean FA, across subjects, within each patient group; and (c) these values were subsequently mapped on to the mean template estimated for the corpus callosum and cingulum, for easy comparison with the registration errors plotted in a similar manner, as shown in Fig. 5.4. Similarly, the standard deviations in fibre orientations about the mean, were also evaluated across subjects, within each patient group, for both WM regions. These are presented in Fig. 5.6. Here, the difference between the mean fibre orientation estimated at each correspondence point and its nearest neighbour voxel in the original hybrid point sets was evaluated as the minimum arc length (in radians) between each other. This in turn was employed to compute the standard deviation in fibre orientations and visualize their spatial distribution across both WM

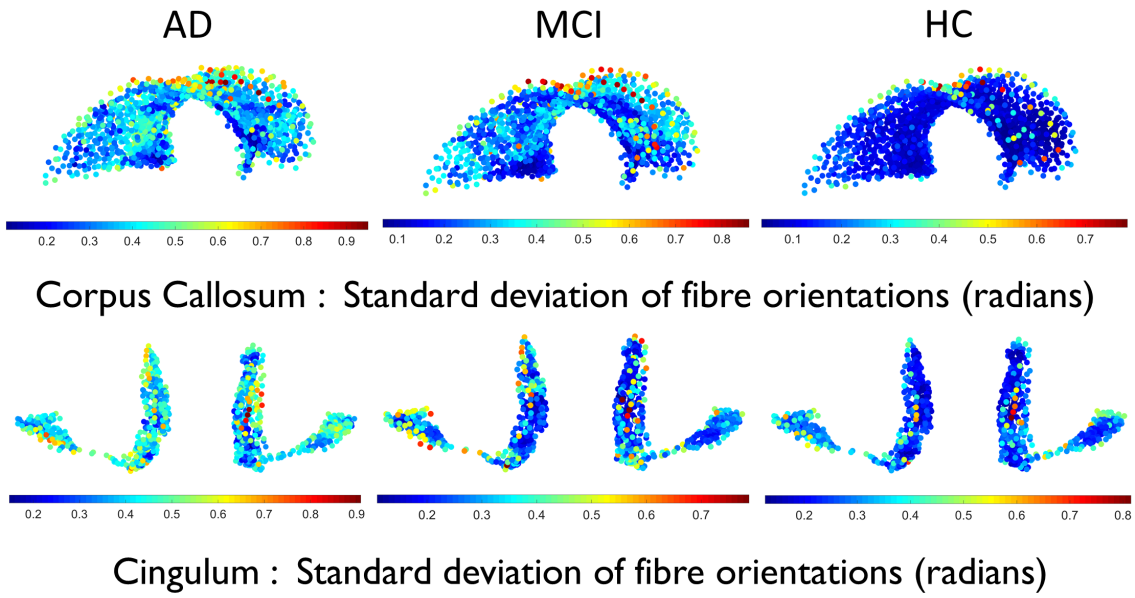

FIGURE 5.6: Standard deviation of fibre orientations computed across subjects in the AD, MCI and HC groups, mapped on to the mean templates estimated, using $M = 2000$ and $M = 1500$ mixture components for the corpus callosum and cingulum, respectively.

regions.

Based on these results, the proposed HMM is inferred to establish valid correspondences across patients, as the estimated fibre orientation and FA errors are low across the majority of correspondences. Fibre orientation errors were consistently < 0.2 radians across most correspondences for both WM ROIs (refer to first and third row in Fig. 5.4). FA errors meanwhile, were < 0.15 and < 0.1 for the corpus callosum and cingulum, respectively (refer to second and fourth row in Fig. 5.4), across all patient groups. For the former WM region, FA errors below 0.15 were evaluated for, $\geq 90\%$ of all established correspondences. While for the latter, $\geq 93\%$ of correspondences, had errors below 0.1. Fibre orientation errors were < 0.2, across $\geq 90\%$ of correspondences estimated for both WM ROIs, in all patient groups. Errors of this magnitude are considered reasonable as the model-predicted FA values and fibre orientations evaluated at correspondences, are based on the soft-assignment approach, using the estimated posterior probabilities. Consequently, they reflect weighted averages of FA and fibre orientations, of neighbouring voxels (rather than specific ones, as is the case with approaches based on exact-correspondences). As FA variations of ≈ 0.1 may occur due to partial volume effects at WM-GM and WM-CSF interfaces (Smith et al., 2006), particularly when WM tracts/ROIs are very thin compared to the voxel

size (often the case following dementia-related atrophy of brain tissue), this could be an another contributing factor to the observed errors. Additionally, significant variations in DTI-data, in a select few cases within individual patient groups, may be another source of the high average errors evaluated, in a small proportion of correspondences. These results are further supported by the standard deviations of FA and fibre orientations depicted in Fig. 5.5 and 5.6, respectively, which highlight the high degree of variation in FA and fibre orientations (across subjects), respectively, relative to the corresponding errors evaluated, across both WM regions.

These results are further verified by the histograms of errors in fibre orientation and FA, presented in Fig. 5.7 and 5.8, respectively, summarising the correspondence-wise errors evaluated for each subject in the population. In this case, fibre orientation errors were computed as in preceding experiments, while FA errors were evaluated as the root-squared-error (RSE) between the model-predicted correspondences and closest ground truth voxels. In general, high errors occur at only a few correspondences, across both the cingulum and corpus callosum. Registration errors for the AD and MCI groups were higher than the HC group, for both ROIs. This is attributed to the presence of varying degrees of pathology-induced changes in a few subjects in these groups, verified by Figs. 5.7 and 5.8, and by computing region-wise mean and standard deviations of FA and fibre orientation errors, presented in Tables 5.3 - 5.7.

Tables 5.2 - 5.7 report the average spatial position, fibre orientation and FA errors evaluated across correspondences and subjects. Statistical significance of the mean spatial position errors presented in Tables 5.2 and 5.5, was assessed across experiments conducted using differing model complexities (i.e. different number of mixture components), considering a significance level of 5%. Statistically significant results are highlighted in bold. In Tables 5.4 , 5.7 the reported mean FA errors were estimated by first computing the RMSE, this time averaging across correspondences, and subsequently computing the mean RMSE across subjects. Tables 5.3 and 5.6 summarise the mean angular error values, first averaged across correspondences and subsequently across subjects. These alternate error measures are presented to assess model quality of the Watson-HMM across regions, and complement the correspondence-wise errors presented in Fig. 5.4. From Tables 5.2 - 5.7, the the number of mixture components required to adequately characterise the entire population, was identified as $M = 1500$ and $M = 2000$, for the cingulum and corpus callosum, respectively. The fibre orientation and FA errors depicted in Fig. 5.4 were evaluated using these values. All subsequent

experiments employed these model complexities identified, for each WM region.

TABLE 5.2: Model quality of Watson-HMM for the cingulum, assessed in terms of the mean spatial position error evaluated across correspondences and subjects, using the MSD metric, for each patient group.

# Mixture Components	Spatial Position Error: MSD (mm.)		
	AD	MCI	HC
500	0.87 ± 0.09	0.88 ± 0.08	0.90 ± 0.10
1000	0.76 ± 0.07	0.76 ± 0.06	0.79 ± 0.10
1500	$\mathbf{0.71 \pm 0.06}$	$\mathbf{0.72 \pm 0.06}$	$\mathbf{0.73 \pm 0.08}$
2000	$\mathbf{0.69 \pm 0.06}$	$\mathbf{0.70 \pm 0.05}$	$\mathbf{0.71 \pm 0.08}$

TABLE 5.3: Model quality of Watson-HMM for the cingulum, assessed as the mean fibre orientation error evaluated across correspondences and subjects, for each patient group.

# Mixture Components	Mean Fibre Orientation Error (radians)		
	AD	MCI	HC
300	0.12 ± 0.11	0.09 ± 0.02	0.08 ± 0.01
600	0.11 ± 0.09	0.08 ± 0.02	0.07 ± 0.01
1200	0.10 ± 0.09	0.08 ± 0.02	0.06 ± 0.01
1500	0.10 ± 0.09	0.07 ± 0.02	0.06 ± 0.01

TABLE 5.4: Model quality of Watson-HMM for the cingulum, assessed as the average RMSE of FA evaluated over correspondences and averaged across subjects, for each patient group.

# Mixture Components	Mean RMSE of FA		
	AD	MCI	HC
300	0.07 ± 0.01	0.07 ± 0.01	0.07 ± 0.01
600	0.07 ± 0.01	0.06 ± 0.01	0.07 ± 0.01
1200	0.06 ± 0.01	0.06 ± 0.01	0.06 ± 0.01
1500	0.06 ± 0.01	0.06 ± 0.01	0.06 ± 0.01

TABLE 5.5: Model quality of Watson-HMM for the corpus callosum, assessed in terms of the mean spatial position error evaluated across correspondences and subjects, using the MSD metric, for each patient group.

# Mixture Components	Spatial Position Error: MSD (mm.)		
	AD	MCI	HC
500	1.11 ± 0.13	1.12 ± 0.10	1.08 ± 0.11
1000	0.97 ± 0.10	0.97 ± 0.08	0.94 ± 0.09
1500	$\mathbf{0.90 \pm 0.09}$	0.90 ± 0.07	$\mathbf{0.87 \pm 0.08}$
2000	$\mathbf{0.85 \pm 0.08}$	$\mathbf{0.86 \pm 0.06}$	$\mathbf{0.82 \pm 0.08}$

TABLE 5.6: Model quality of Watson-HMM for the corpus callosum, assessed as the mean fibre orientation error evaluated across correspondences and subjects, for each patient group.

# Mixture Components	Mean Fibre Orientation Error (radians)		
	AD	MCI	HC
500	0.15 ± 0.20	0.11 ± 0.15	0.06 ± 0.01
1000	0.15 ± 0.20	0.11 ± 0.16	0.06 ± 0.01
1500	0.14 ± 0.19	0.10 ± 0.15	0.05 ± 0.01
2000	0.14 ± 0.19	0.10 ± 0.15	0.05 ± 0.01

TABLE 5.7: Model quality of Watson-HMM for the corpus callosum, assessed as the average RMSE of FA evaluated over correspondences and averaged across subjects, for each patient group.

# Mixture Components	Mean RMSE of FA		
	AD	MCI	HC
500	0.12 ± 0.03	0.12 ± 0.02	0.10 ± 0.01
1000	0.11 ± 0.03	0.11 ± 0.03	0.09 ± 0.01
1500	0.10 ± 0.03	0.10 ± 0.03	0.08 ± 0.01
2000	0.10 ± 0.02	0.09 ± 0.03	0.08 ± 0.01

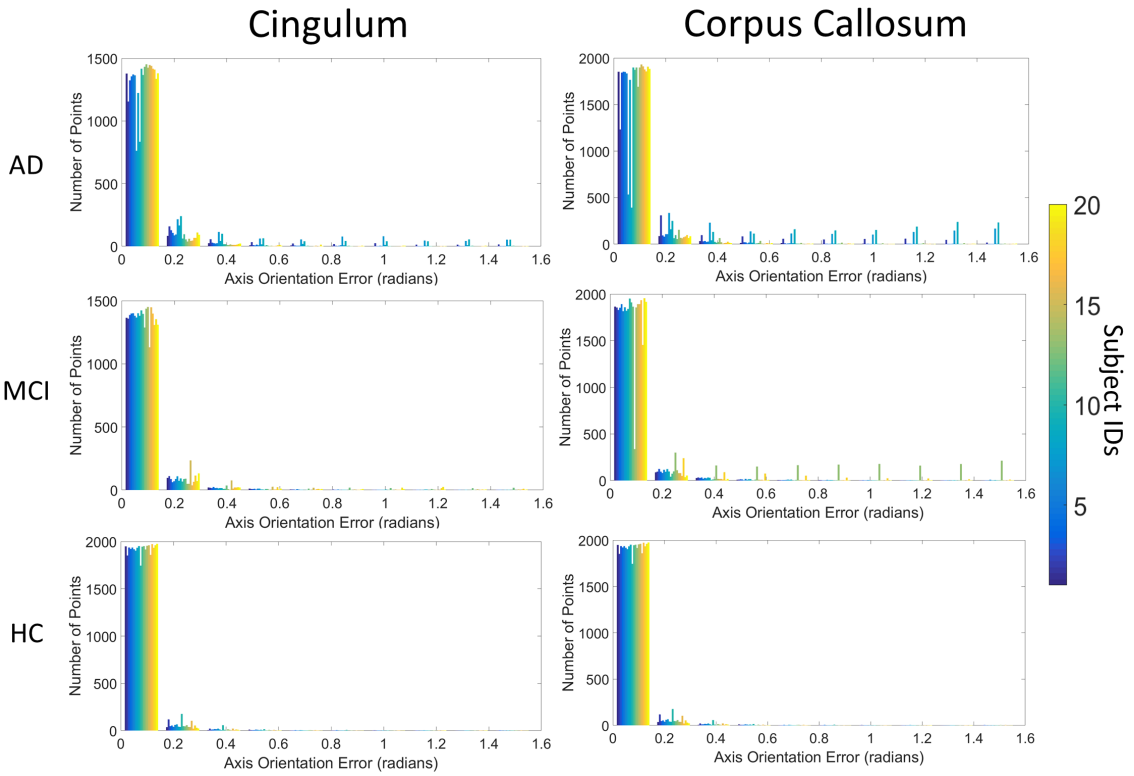

FIGURE 5.7: Histograms of fibre orientation errors for each subject in AD, MCI and HC groups, evaluated between established correspondences and ground truth voxels.

Results in Fig. 5.7, 5.8 indicate that the proposed framework achieves low fibre orientation and FA errors at each estimated correspondence, for all subjects in the HC group (for both WM ROIs). The estimated correspondences were less accurate for two cases in the AD group (for both cingulum and corpus callosum) and for one case in the MCI group (only corpus callosum), which is attributed to significant variation in fibre orientations and FA values in these cases and ROIs, relative to the remaining samples in their corresponding patient groups. As discussed previously, this may be a result of varying degrees of pathology-induced changes, in these cases, relative to the rest of their group. Consequently, the accuracy of the HMM when fitting to these few cases, is reduced. The proposed framework however, established accurate correspondences for the remaining samples in the AD and MCI groups, across both WM ROIs. The high deviations from the mean fibre orientation errors estimated for these groups, in the corpus callosum (Table 5.6), are thus attributed to the outlier subjects identified from the corresponding histograms (Fig. 5.7). Similarly, for the cingulum, the high standard deviations observed for the AD group, are attributable to the two subjects mentioned above. However, no apparent outliers were identified in the MCI group,

based on the registration errors and by extension, the mean FA and fibre orientation errors reported in Tables 5.4, 5.3, are low and consistent with their corresponding histogram plots (Fig. 5.8 and Fig. 5.7).

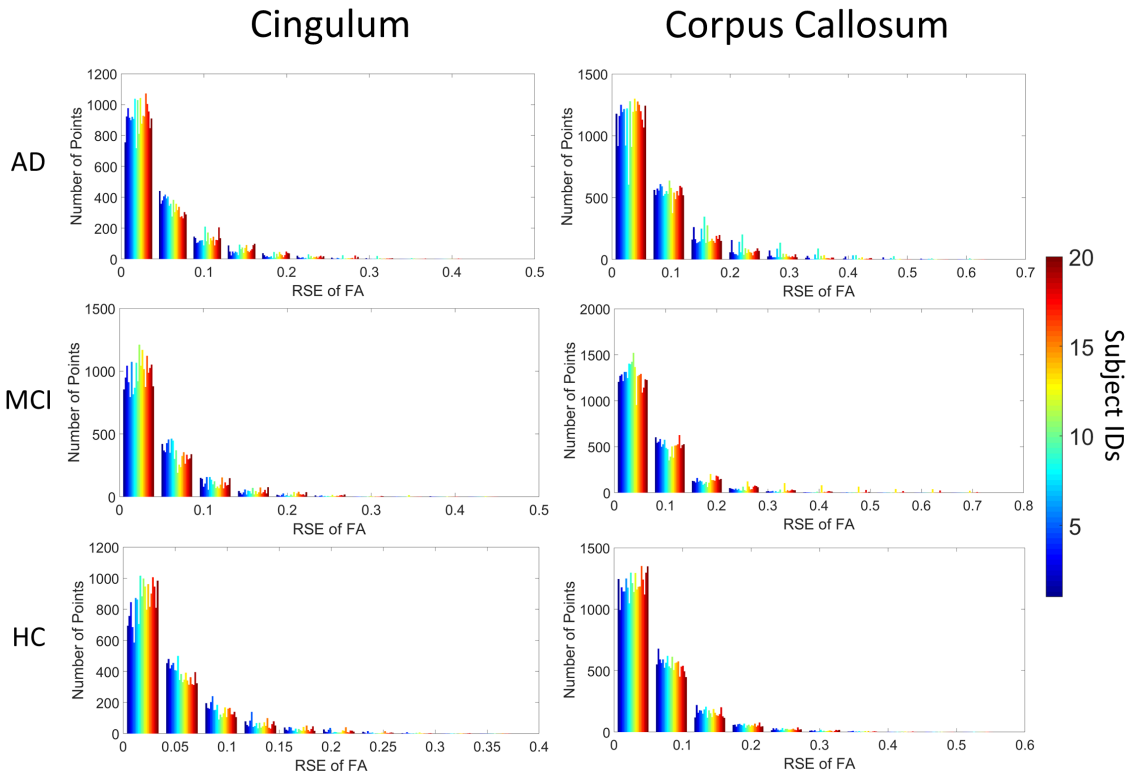

FIGURE 5.8: Histograms of root-squared-error (RSE) of FA for each subject in AD, MCI and HC groups, evaluated between established correspondences and ground truth voxels.

The foregoing results suggest the proposed framework established valid correspondences for both WM ROIs, across all subjects in the HC group and for the majority of cases in the AD and MCI groups. This is indicative of the ability of the proposed HMM to approximate the joint *PDF* of positions, fibre orientations and FA values, across multiple subjects.

5.3.3 Group Comparisons

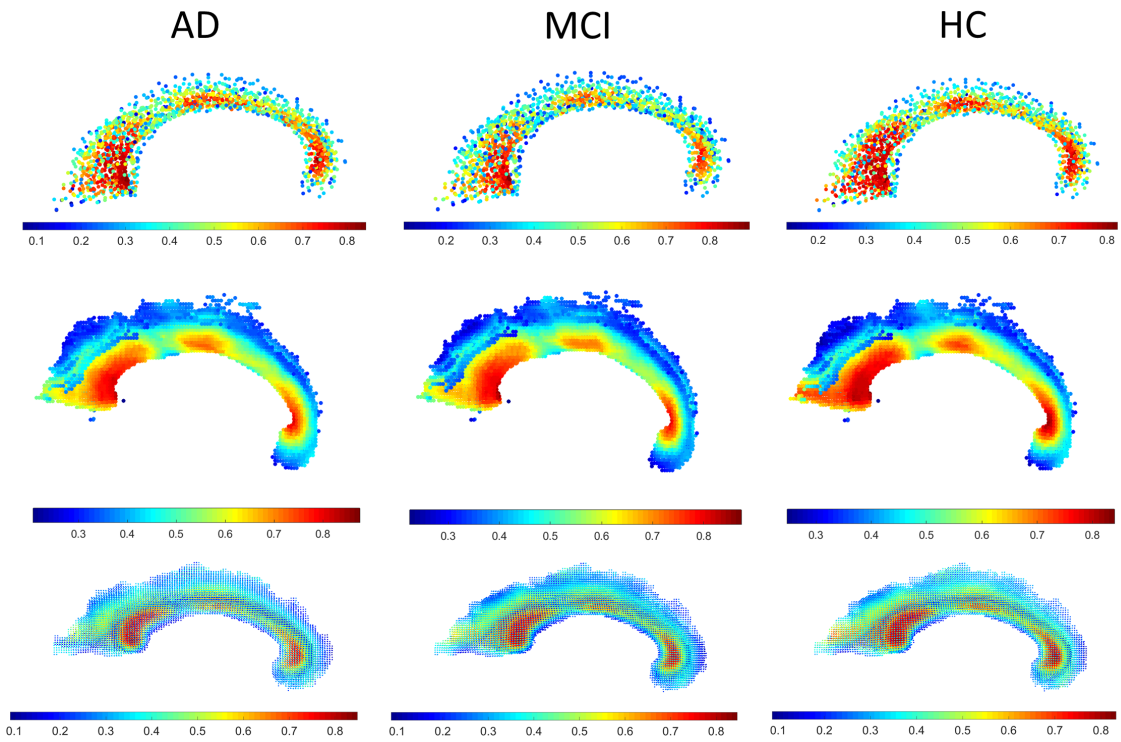

FIGURE 5.9: Comparison of corpus callosum mean FA distributions (indicated by colour bars) in AD, MCI, and HC groups, estimated using TBSS, VBM, and the proposed HMM approach. Top row: Mixture centroids of the mean template estimated using HMM; Middle row: Mean FA skeleton computed with TBSS; Bottom row: Mean FA voxels computed with VBM.

The ability of the proposed framework to identify significant differences between patient groups was assessed by comparing each pair of patient sub-groups, in terms of the variation in FA. These results were compared with those obtained from the widely used TBSS approach. Un-paired two-sample T-tests, assuming unequal variances, were performed to compare FA values at corresponding spatial positions, between subject groups. The procedure proposed in (Benjamini and Yekutieli, 2001) was used to correct for multiple comparisons, by controlling the false discovery rate (FDR) for the set of hypothesis tests. The desired false discovery rate was fixed at 1% for all experiments. The mean corpus callosum templates estimated for each patient group using the proposed approach are presented in Fig. 5.9 (top row), which depict mean positions colour mapped with their corresponding mean FA values. Fig. 5.9 (middle row) depicts the mean FA

skeleton for the corpus callosum, estimated using TBSS, while mean FA voxels estimated using VBM are presented in the bottom row.

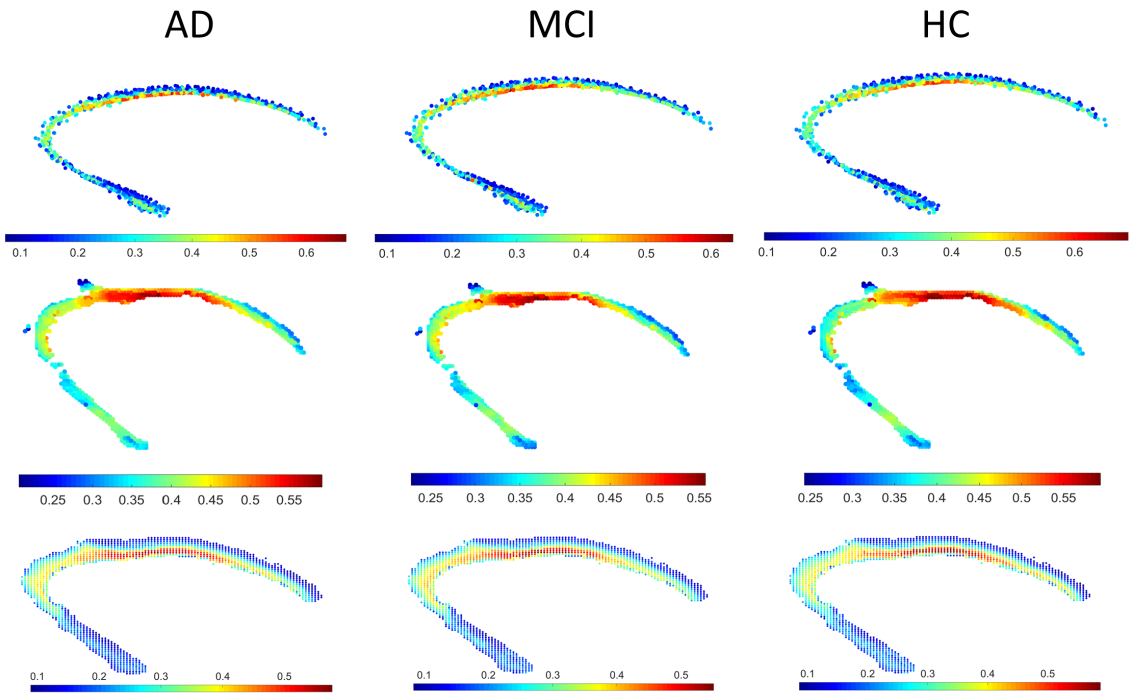

FIGURE 5.10: Comparison of cingulum mean FA distributions (indicated by colour bars) in AD, MCI, and HC groups, estimated using TBSS, VBM, and the proposed HMM approach. Top row: Mixture centroids of the mean template estimated using HMM; Middle row: Mean FA skeleton computed with TBSS; Bottom row: Mean FA voxels computed with VBM.

TBSS estimates a mean FA image (by registering each subjects' image to a template), prior to generating the skeleton. The JHU-ICBM-DTI-81 atlas was registered to this mean FA image to segment the ROIs, and perform voxel-wise analysis (referred to as VBM). The FA skeleton voxels corresponding to the cingulum and corpus callosum were extracted using the label propagation approach employed to generate the training data set of hybrid point sets (refer to section 5.2.1). The difference in orientation observed in Fig. 5.9, between the mean corpus callosum templates estimated by the proposed approach and TBSS, arises because the latter registers each subject's image to the MNI-152 atlas. Additionally, as the MNI-atlas is of a higher resolution (voxel spacing of $1 \times 1 \times 1$ mm) than the raw FA and eigenvector images of each subject (refer to section 5.2.1), the resulting template depicted in Fig. 5.9 (bottom row) is significantly denser than the template estimated using the proposed approach. The mean templates and mean FA

values estimated for the cingulum, using the proposed approach and TBSS are presented in Fig. 5.10, top and middle row, respectively. Mean FA voxels for the cingulum estimated using VBM are depicted in the bottom row. As the mean FA skeleton estimated using TBSS is generated using a thinning and skeletonisation process (Smith et al., 2006), the resulting template represents a structure analogous to the centreline of the WM tracts, rather than the entire region of interest (as with the proposed approach). Consequently, direct quantitative comparison between the mean templates estimated using each method is difficult. The mean FA distributions across templates are thus assessed visually, showing good overlap in the range and spatial distribution, for both the cingulum (Fig. 5.10) and corpus callosum (Fig. 5.9). High mean FA values $(\approx 0.5 - 0.6)$ are concentrated in the body of the cingulum, in the HMM-, VBM- and TBSS-predicted templates. For the corpus callosum, high mean FA values $(\approx 0.7 - 0.8)$ are evaluated at the genu, central body and splenium, using all three approaches (Fig. 5.9).

Interquartile ranges (IQRs) for the mean FA values estimated using each approach were also evaluated, to provide a quantitative means of comparing the range of estimated FA values for both WM ROIs. This measure is adopted as it provides a robust means of assessing dispersion in data. IQRs are summarised in Table 5.8 for both WM ROIs, from which we infer that all three methods do indeed show similarities in the range of mean FA values estimated, for the corpus callosum. Conversely for the cingulum, while VBM and the proposed approach show similar IQRs, the ranges estimated for TBSS are lower. This is because TBSS models the central skeleton of the ROI, and there is substantial variation in FA between the center and peripheral regions of cingulum region. Consequently, the variation in mean FA values in the skeleton voxels is lower in comparison to the entire ROI (as modelled by VBM and HMM). This is further supported by the colorbars depicted in Fig. 5.10, which show the minimum mean FA values estimated using TBSS is 0.25, while for VBM and HMM it is 0.1, concentrated along the boundaries.

TABLE 5.8: Interquartile ranges for mean FA values estimated using each approach for both WM ROIs.

Method	Corpus Callosum: IQR of mean FA			Cingulum: IQR of mean FA		
	AD	MCI	HC	AD	MCI	HC
HMM	0.27	0.27	0.26	0.19	0.19	0.18
TBSS	0.20	0.21	0.21	0.08	0.08	0.09
VBM	0.21	0.21	0.21	0.14	0.13	0.14

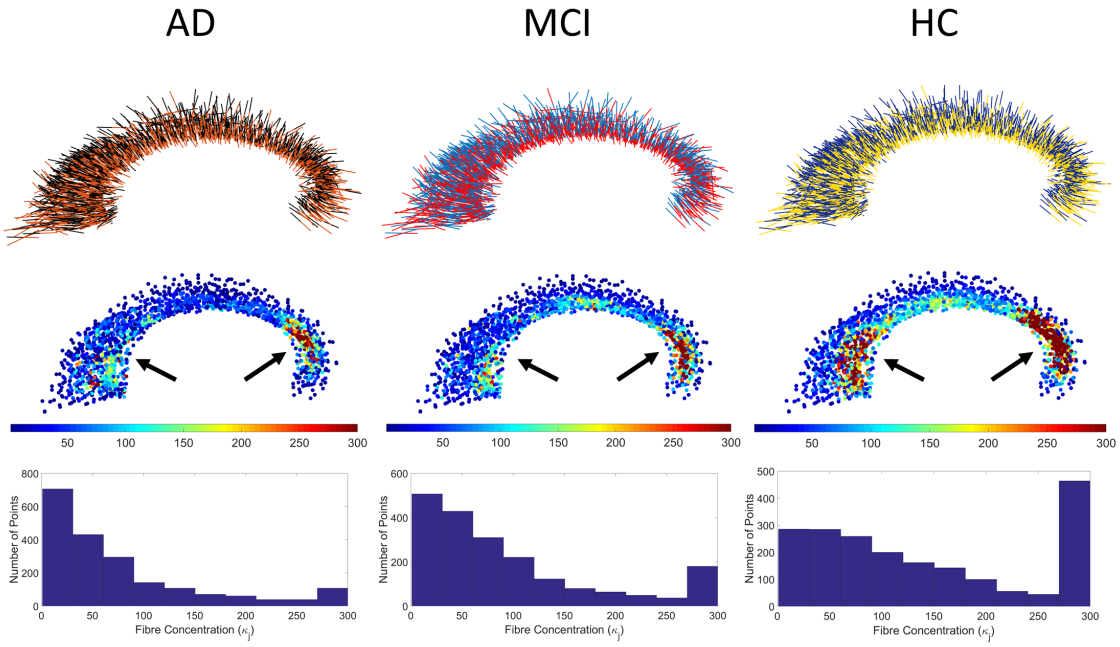

FIGURE 5.11: Top row: Mean fibre orientations estimated for AD, MCI and HC groups across the corpus callosum; Middle row: Mean corpus callosum templates for each patient group, overlaid with the concentration parameters κ_j estimated for each mixture component. Arrows indicate regions showing increased fibre dispersion in AD and MCI groups relative to HC; Bottom row: Histograms describing the distribution of κ_j values estimated for each patient group.

In addition to estimating the mean FA value at each correspondence, the proposed framework provides point-wise estimates of the mean fibre orientation and degree of concentration (defined by κ_j, estimated for each mixture centroid - see section 5.2.4) across subjects, as depicted in Fig. 5.11 and Fig. 5.12. As discussed previously, the primary advantage of the proposed Watson-HMM framework is its ability to model fibre orientations and facilitate their comparison across multiple subjects, not offered by conventional approaches such as TBSS and VBM.

Furthermore, the proposed method does not require extraction of fibre trajectories using tractography in order to model fibre orientations as it operates directly the raw DTI-derived eigenvectors, unlike state-of-the-art approaches such as those proposed in (O'Donnell and Westin, 2007) and (Zvitia et al., 2010). Visual inspection of these fibre concentration maps and their corresponding histograms indicate increased dispersion in the genu and splenium of the corpus callosum (specified by the arrows shown in Fig. 5.11), in the AD and MCI groups relative to HC. Group differences in fibre concentration are visually less apparent, for the cingulum, although some reduction in fibre concentration in the central body is visible for the AD group relative to MCI and HC (as indicated by the arrows in Fig. 5.12). The histograms in Fig. 5.12, however, verify that there is indeed increased fibre dispersion for the AD group, relative MCI and HC, across the cingulum.

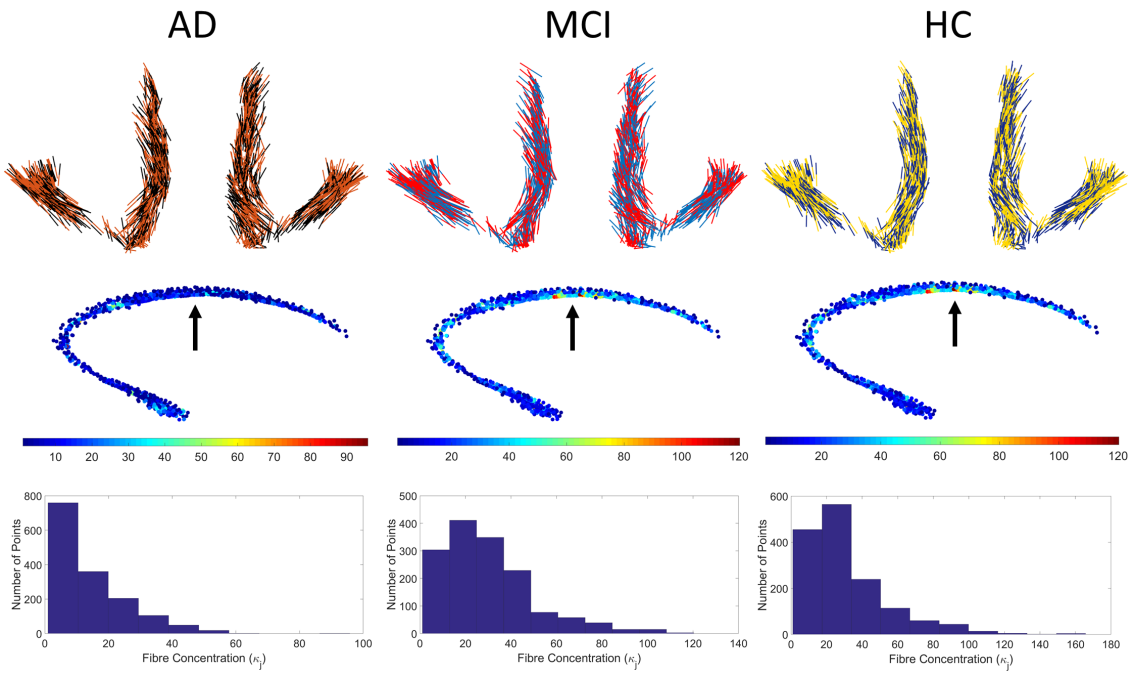

FIGURE 5.12: Top row: Mean fibre orientations estimated for AD, MCI and HC groups across the cingulum; Middle row: Mean cingulum templates for each patient group, overlaid with the concentration parameters κ_j estimated for each mixture component. Arrows indicate regions of reduced fibre concentration in AD group compared to MCI and HC.; Bottom row: Histograms describing the distribution of κ_j values estimated for each patient group.

In order to quantitatively assess the distribution of mean FA values and mean fibre concentrations κ_j estimated using HMM, across the corpus callosum and

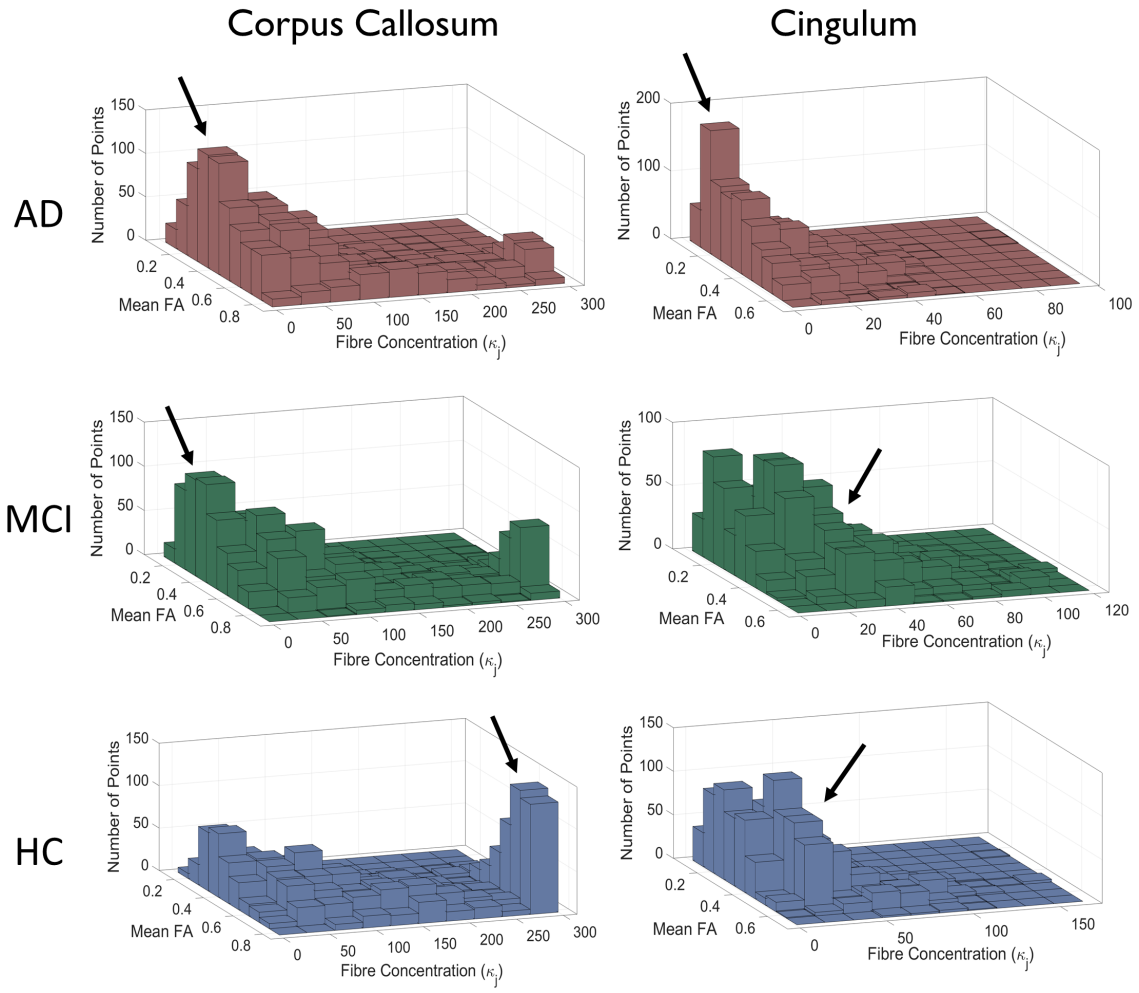

FIGURE 5.13: 3D histograms describing the combined distribution of mean FA values and mean fibre concentrations κ_j, estimated across correspondences established using HMM, for the corpus callosum (left column) and cingulum (right column) regions. Arrows indicate differences identified between patient groups.

cingulum templates for each patient group, 3D histograms were computed, presented in Fig. 5.13. These plots show low FA values and low fibre concentrations were estimated at a substantially higher number of correspondences, for the AD group, relative to HC (as indicated by the arrows), for both WM ROIs. For the corpus callosum, differences between MCI and HC are also visually apparent, although to a modest degree, with the former showing a higher a number of points with low FA values and low fibre concentrations, relative to the latter. Differences between the MCI and HC groups are however, less apparent in Fig. 5.13 for the cingulum. Based on these plots, there are no visually apparent differences in FA and fibre concentration, between the AD and MCI groups, for both WM ROIs.

These differences in mean FA values between patient groups are corroborated by the hypothesis tests conducted, to identify significant group-wise differences in FA.

Significant reduction in FA was observed (considering a significance level of 1%) across the corpus callosum (refer to Fig. 5.14) and cingulum (refer to Fig. 5.15), in the AD group relative to HC, and in the MCI group relative to the latter, albeit to a lesser degree. Conversely, there was negligible reduction in FA in the AD group relative to MCI, as expected, for both WM ROIs. TBSS on the other hand, following multiple comparisons correction using FDR, showed no significant reduction in FA, between any of the three groups. The differing results from each method may be expected, given their different approaches to modelling the ROI spatial domains: in TBSS, a mean FA skeleton representing the centre of the tracts/ROIs is produced and used to compute voxel-wise statistics; in the proposed HMM approach, the entire ROI is considered and, consequently, a higher proportion of spatial positions (exhibiting significant reduction in FA between groups) is identified.

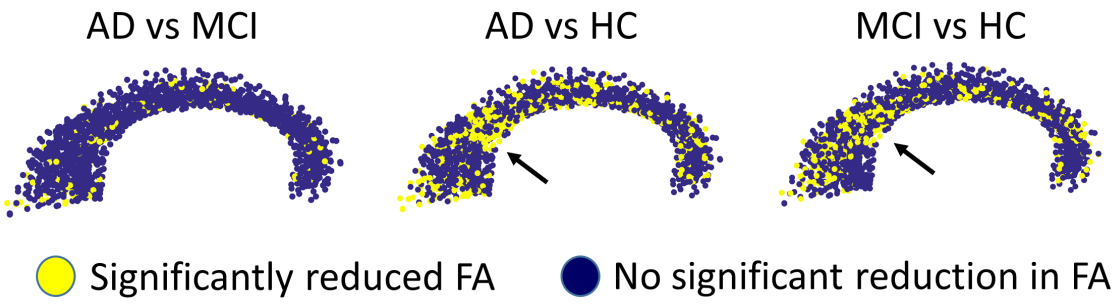

FIGURE 5.14: Statistically significant reduction in FA (based on FDR-corrected p-values), at corresponding spatial positions across the corpus callosum, for: AD vs MCI, AD vs HC and MCI vs HC patient groups, estimated using the proposed framework. Arrows indicate regions showing substantial reduction in FA.

The proposed HMM, for the joint registration and clustering of data comprising positions, orientations and scalar-valued features (such as FA), thus shows promise for statistical analysis of diffusion derived measures, across multiple subjects and patient populations. The flexibility of the approach, enables analysis of various scalar-valued diffusion measures (although just FA was considered in this study), similar to existing approaches such as TBSS and VBM. But, it also permits analysis of local fibre orientation (defined by primary diffusion axes), a capability not afforded by existing techniques. Although approaches based on

clustering of fibre tracjectories enable such analyses, they require diffusion tractography derived fibres, in order to do so. The present work ameliorates this need and acts directly on the raw eigenvector images.

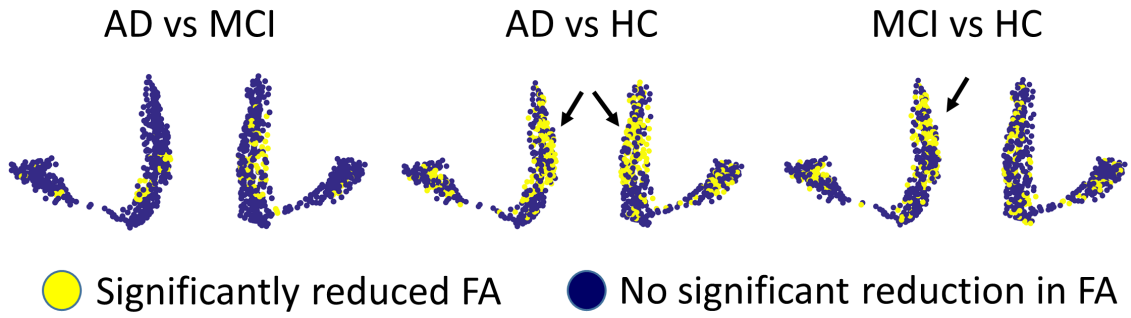

FIGURE 5.15: Statistically significant reduction in FA (based on FDR-corrected p-values), at corresponding spatial positions across the cingulum, for: AD vs MCI, AD vs HC and MCI vs HC patient groups, estimated using the proposed framework. Arrows indicate regions showing substantial reduction in FA.

The sensitivity and discriminative capacity of the proposed framework, in comparison to existing approaches requires further investigation and validation, which future work will look to achieve. Natural extensions to the proposed framework include, whole WM volume analysis across multiple subjects, WM parcellation and automatic region-of-interest analysis, to name a few. As discussed previously, the proposed approach can be employed to analyse the entire WM volume across subjects, i.e. *a priori* definition of ROIs is not required, though the computational burden at present is substantial. Such an approach, naturally leads to the unsupervised parcellation of the WM into distinct clusters defined by the centroids of the HMM, across multiple subjects. This in turn provides a mechanism for automatic ROI-type analyses, as the generated clusters for each subject, will correspond to similar WM regions in terms of spatial position, fibre orientation and FA (or some other scalar measure of interest). Furthermore, by employing a suitable prior/atlas containing pre-defined labels for WM tracts of interest, the proposed approach could be employed for automatic tractography segmentation (similar to (O'Donnell and Westin, 2007)). A preliminary study is presented in the next section demonstrating the ability of the proposed HMM to parcellate WM into 100 similar anatomical regions. The proposed approach can also be employed to identify and track localised changes in WM over time, for a single subject, resulting from the progression of neuro-degenerative disorders such as dementia, for example. Although WM changes in the brain were

considered in this study, the generic nature of the proposed framework, permits its application to other organs exhibiting tissue anisotropy, such as cardiac diffusion data, and modelling bone micro-architecture. The proposed approach thus provides various avenues for future research, towards identifying morphological changes between patient populations.

5.3.4 WM Parcellation

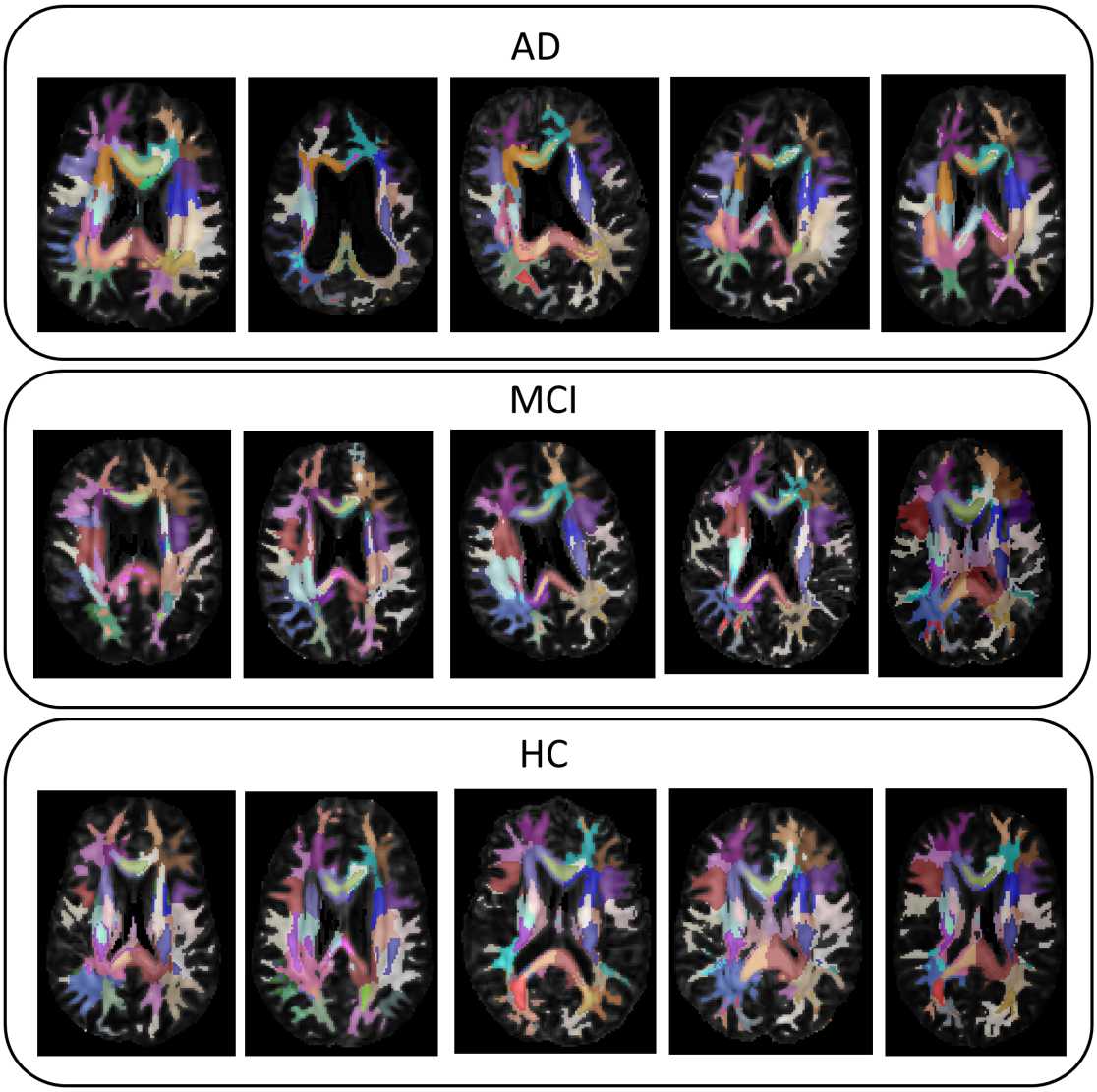

FIGURE 5.16: Axial view of WM volumes parcellated into 100 distinct regions (using Watson-distribution based HMM) and overlaid on corresponding FA images, for AD, MCI and HC subjects.

A limitation of ROI-type analyses as discussed previously, is the difficulty in ensuring consistency and reproducibility, when delineating ROIs in multiple subjects' images. However, this may be addressed by jointly registering and clustering the entire WM volume into distinct clusters, that represent equivalent anatomical regions in all subjects. Such a framework is realised, using the proposed Watson distribution-based HMM, by utilizing information from multi-dimensional features comprising, positions, fibre orientations and FA values. WM masks were generated from FA images of 5 AD, 5 MCI and 5 HC subjects (from the same data set), by thresholding the images at 0.2 in order to exclude GM and CSF voxels and reduce the effects of partial voluming (Smith et al., 2006). The resulting voxels were considered to represent WM volumes. Subsequently, hybrid point sets were constructed for each subject, as done previously by concatenating voxel spatial positions, their associated DTI-derived eigenvectors and FA values (refer to section 5.2.2), and jointly registered and clustered using 100 mixture components. The estimated posterior probabilities were in turn used to parcellate the WM volumes from all 15 subjects into 100 distinct patches (depicted in Fig. 5.16).

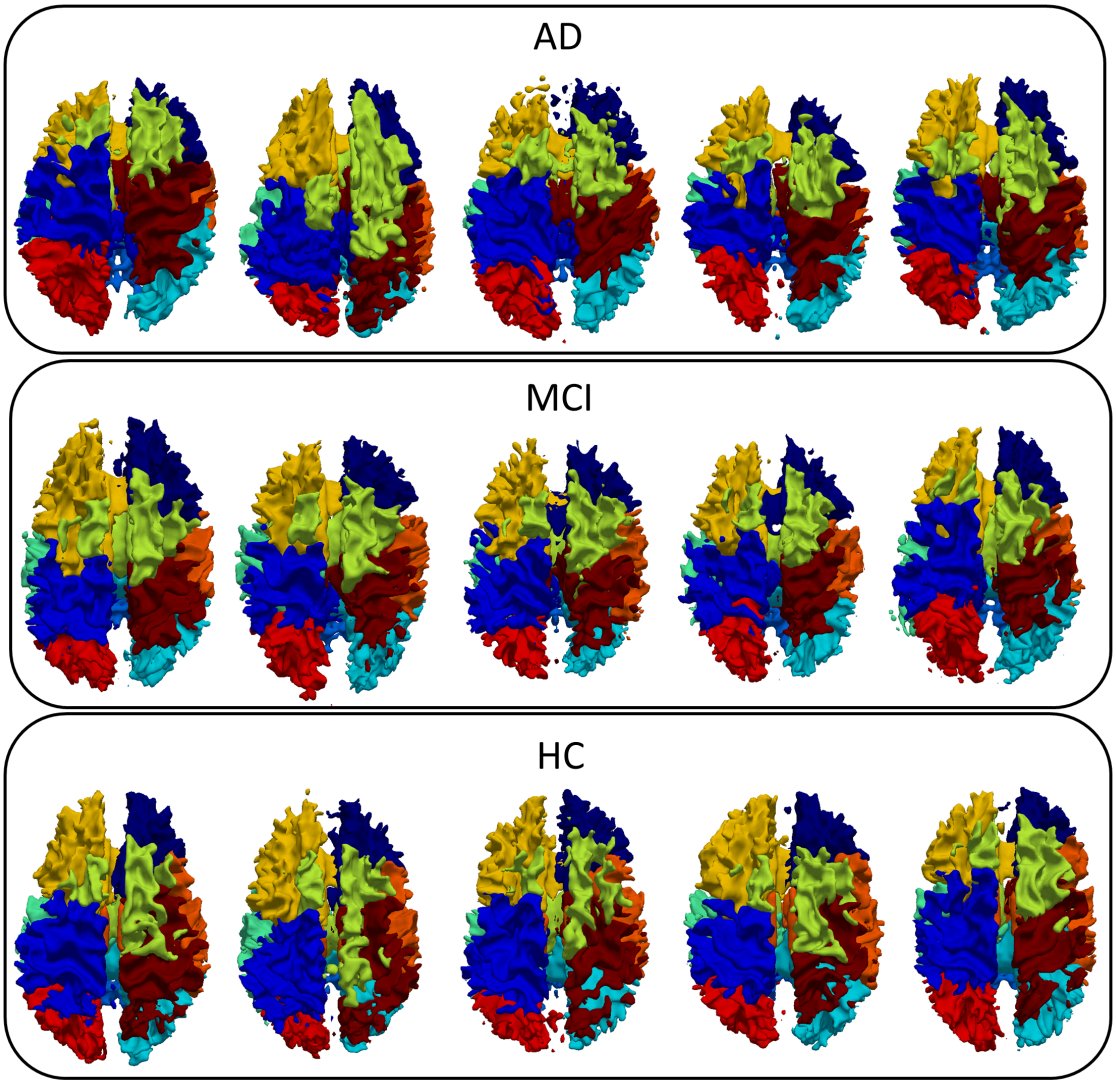

FIGURE 5.17: Axial view of WM volumes parcellated and clustered into 10 'parent' regions depicted as surfaces, for 5 AD (top row), 5 MCI (middle row) and 5 HC (bottom row) subjects.

Similarity between the parcellated WM regions across all subjects was assessed visually as follows: (1) labels for all 100 regions were grouped into 10 parent clusters, by clustering (using the conventional k-means clustering algorithm) the estimated mean templates (for each patient group) based on spatial positions alone. This approach is adopted to group the identified children clusters, based on spatial proximity, into larger regions for easier visual assessment; and (2) labels assigned to each parent cluster were in turn fused to generate larger patches. Surfaces were rendered for each 'parent' region, for better visualisation, which showed anatomical similarities across all subjects (as illustrated by Fig. 5.17-5.19). The labels estimated initially (as in Fig. 5.16), may be constrained to

known ROIs by choosing a suitable atlas with pre-defined labels, to initialise the mean of the HMM, and subsequently, jointly registering and clustering the WM volumes. These preliminary results suggest that the proposed framework shows promise towards automatically delineating ROIs across multiple subjects' images, useful for conducting subsequent statistical analyses of DTI-derived data. However, further quantitative evaluation of anatomical similarity between the identified regions is required, for thorough validation of the proposed approach, which subsequent work could look to achieve.

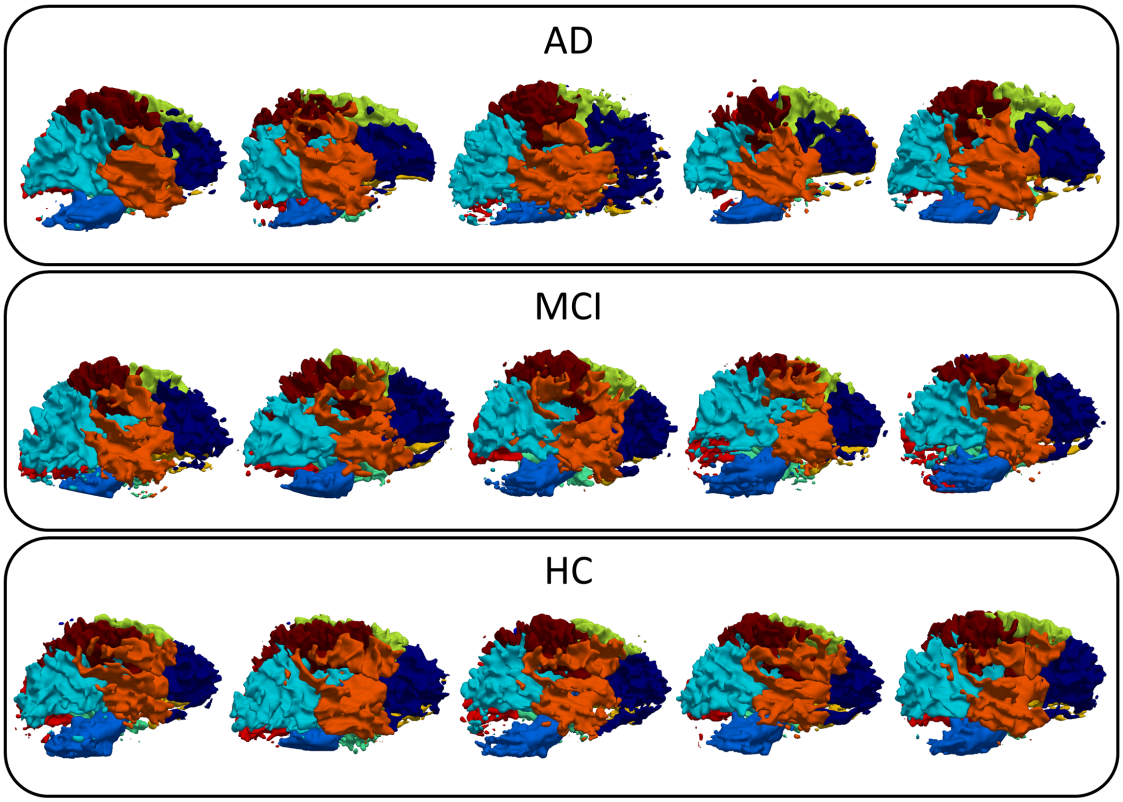

FIGURE 5.18: Sagittal view of WM volumes parcellated and clustered into 10 'parent' regions depicted as surfaces, for 5 AD (top row), 5 MCI (middle row) and 5 HC (bottom row) subjects.

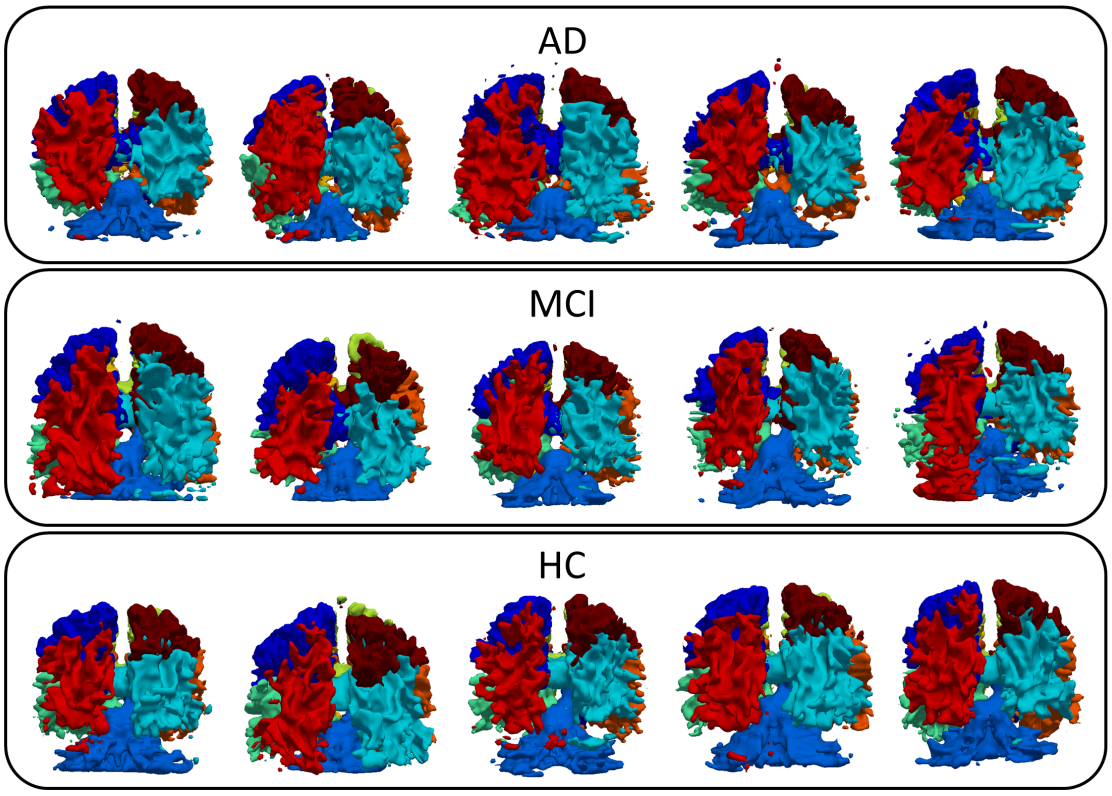

FIGURE 5.19: Coronal view of WM volumes parcellated and clustered into 10 'parent' regions depicted as surfaces, for 5 AD (top row), 5 MCI (middle row) and 5 HC (bottom row) subjects.

5.4 Application 2: Results and Discussion

5.4.1 Registration Accuracy

The data set of brain ventricles employed in **chapter** 3 was used to assess the registration accuracy of the Fisher-distribution based HMM framework. Point sets along with their surface normals were generated from segmentations using a marching cubes-based algorithm (ventricles were segmented as described previously in **chapter** 3) and registered using the HMM. The estimated surface normals for each sample in the data set, were consistently oriented outwards (with respect to the object surface), prior to registration. Registration accuracy was quantitatively assessed using the HD and MSD measures and statistical significance of the results was evaluated using the paired-sample t-test (as done previously). These results are summarised in Table 5.9, with significant improvements in accuracy highlighted in bold. Comparison of the registration errors evaluated for HMM, with point-based registration approaches, namely, TMM-NR and gCPD (refer to

Table 3.10), indicates that the former achieved significantly lower MSD errors, consistently, for $M = 500, 800$ and 1200 mixture components. Conversely, the latter resulted in significantly lower HD errors. As discussed previously in **chapter** 3), this difference in HD and MSD errors are due to the presence of posterior temporal horns in a limited number of samples in the data set. Consequently, while gCPD and TMM-NR (albeit to a lesser degree than gCPD) attempt to establish correspondence in these regions, HMM does not. This is attributed to the higher discriminative capacity of point sets with associated surface normals, and correspondingly of the HMM, enabling estimation of anatomically valid correspondences. As the latter attempts to match both points and their associated normals, registration and correspondence estimation is constrained to a greater degree than point-based approaches. This is reflected by the relatively high HD error evaluated for HMM, relative to gCPD and TMM-NR and conversely the low MSD error of the former, relative to the latter. The advantage of HMM over point-based registration approaches in this regard, is verified by visual inspection of the correspondences estimated using each method (shown in Fig. 5.20).

TABLE 5.9: Non-rigid registration accuracy using HMM for brain ventricles data set.

Method	**Ventricles** $(K = 27)$					
	$M = 500$		$M = 800$		$M = 1200$	
	HD (mm)	**MSD (mm)**	**HD (mm)**	**MSD (mm)**	**HD (mm)**	**MSD (mm)**
HMM	7.77 ± 2.83	$\mathbf{1.92 \pm 0.13}$	7.25 ± 3.00	$\mathbf{1.58 \pm 0.16}$	11.22 ± 5.98	$\mathbf{0.60 \pm 0.22}$

Correspondences estimated using HMM, overlaid on the original ventricle point sets, are presented in Fig. 5.20 (a,c). Fig. 5.20 (e,g) and (i,k) depict the corresponding samples registered using TMM-NR and gCPD, respectively. Black arrows in these images indicate regions of the posterior temporal horns of the ventricles (missing in the majority of samples in the data set), where, the latter establish non-homologous correspondences. HMM on the other hand (Fig. 5.20 (a,c)) is robust in this regard and consequently, ensures greater anatomical validity in the estimated correspondences. The green arrows shown in Fig. 5.20 (g,k) highlight another region in the temporal horns, for a sample in the data set,

where, HMM (refer to Fig. 5.20 (c)) affords significant improvement in the quality of correspondences established, over TMM-NR and gCPD. The images presented in Fig. 5.20 (b,d), (f,h), (j,l) depict the correspondences estimated for each sample (discussed in the preceding set of images), using HMM, TMM-NR and gCPD respectively. Arrows shown in these images highlight the ability of HMM to preserve the separation between the left and right lateral ventricles, thereby preserving the topology of the shapes, not afforded by TMM-NR and gCPD. This limitation of point set registration approaches based on spatial positions alone, was discussed previously in **chapter** 3 (section 3.3.3.2). This represents another significant advantage of the former, over the latter, with respect to establishing anatomically valid correspondences. Consequently, the HMM-based registration approach incorporating surface normals as additional features, is inferred to improve registration accuracy relative to the state-of-the-art point-based methods (TMM-NR and gCPD).

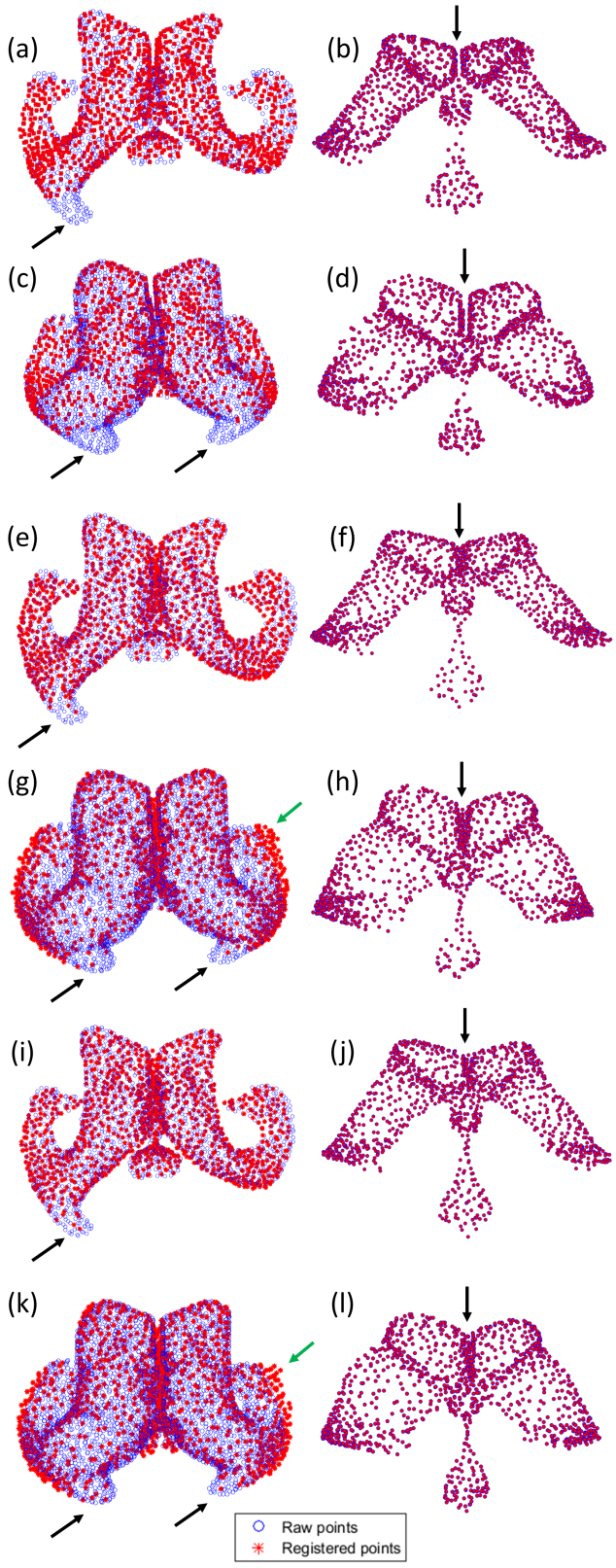

FIGURE 5.20: Two registered samples from ventricles data set: (a,b), (c,d) using Fisher-HMM; (e,f), (g,h) using TMM-NR; and (i,j), (k,l) using gCPD (non-rigid). Registered shapes (red) overlaid on their corresponding raw samples (black) are shown in (a,c,e,g,i,k). (b,d,f,h,j,l) depict correspondences estimated for both samples using each method.

5.4.2 SSM Quality

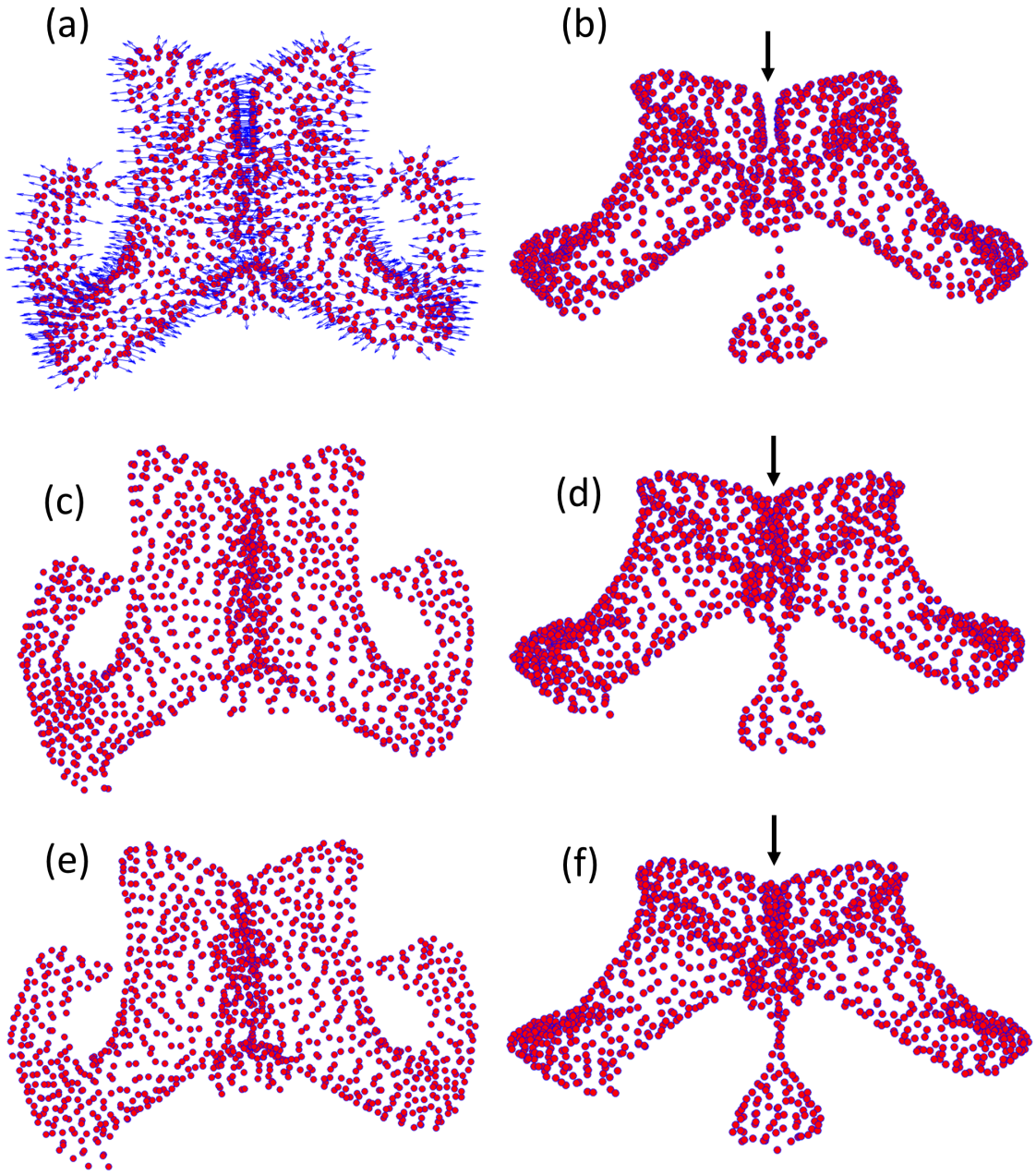

FIGURE 5.21: Mean ventricle shapes estimated with $M = 1200$ mixture components using HMM (a,b), TMM-NR (c,d) and gCPD-nonrigid (e,f). Blue arrows in (a) represent mean surface normals, black arrows in (b,d,f) highlight separation between lateral ventricles preserved by HMM but not afforded by TMM-NR and gCPD.

The ability of the HMM to preserve fine structural details, such as the separation between the left and right lateral ventricles, not afforded by its point-based counterparts, namely, TMM-NR and gCPD, was also assessed by visual inspection of, the estimated mean ventricle shapes (Fig. 5.21), and correspondences established, for a few samples in the data set (Fig. 5.20). The images presented in Fig. 5.21 clearly demonstrate the superiority of the HMM-based approach in this context. Additionally, the mean surface normal directions estimated using this approach are consistently oriented outwards, as expected, since the data set of ventricles were pre-processed to ensure the same (as illustrated by Fig. 5.21 (a)).

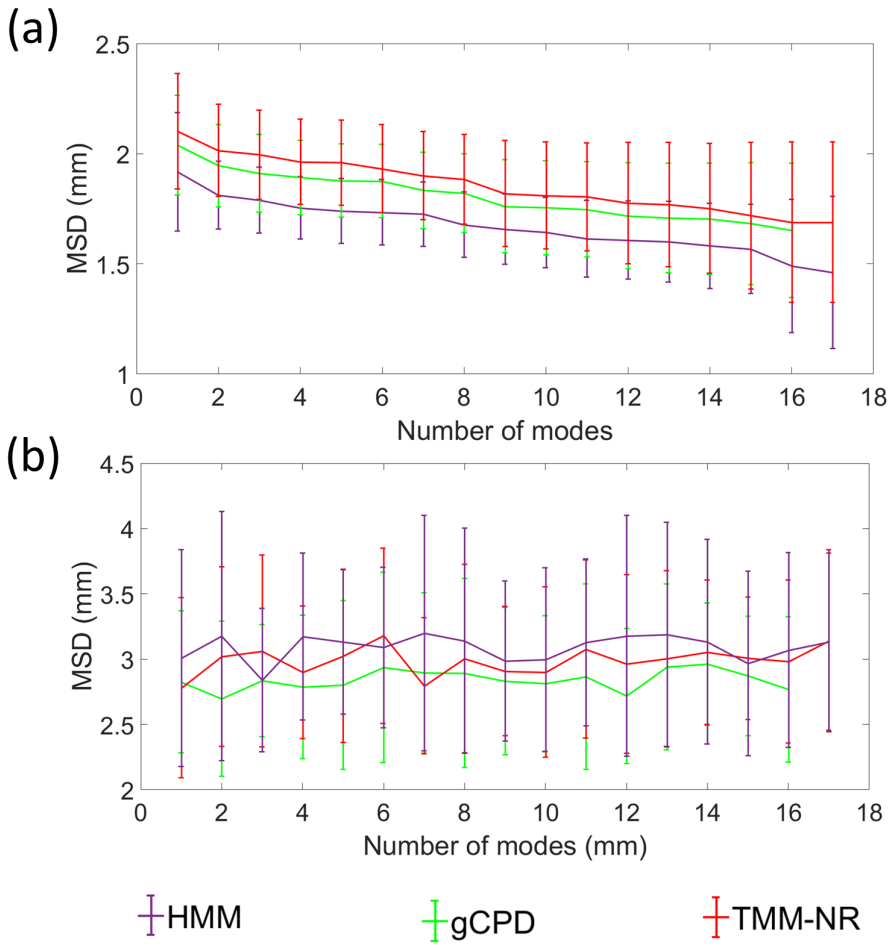

FIGURE 5.22: SSM quality evaluated in terms of generalisation (a) and specificity (b) errors computed with respect to the number of modes of variation.

The quality of ventricle SSMs generated (by PCA), following group-wise registration using: HMM, TMM-NR and gCPD, was also evaluated to verify the advantage afforded by the former, over point-based approaches (TMM-NR and

gCPD). SSM quality was quantified in terms of generalisation (refer to Fig. 5.22 (a)) and specificity (refer to Fig. 5.22 (b)), by conducting leave-one-out full-fold cross-validation experiments. Errors were evaluated with respect to the number of modes of variation, as done previously in **chapter** 4, using $M = 1200$ mixture components (for each method). HMM achieved lower generalisation errors than TMM-NR and gCPD, as depicted in Fig. 5.22 (a). Consequently, SSMs trained using HMM are inferred to generalise to unseen shapes more accurately than those generated using point-based registration approaches. Specificity errors meanwhile, were comparable across all three methods (refer to Fig. 5.22 (b)). However, visual inspection of the modes of variation (refer to Figs. 5.23-5.25) showed greater anatomical validity for those estimated following registration using HMM, relative to TMM-NR and gCPD, consistent with the registration results discussed in the previous section.

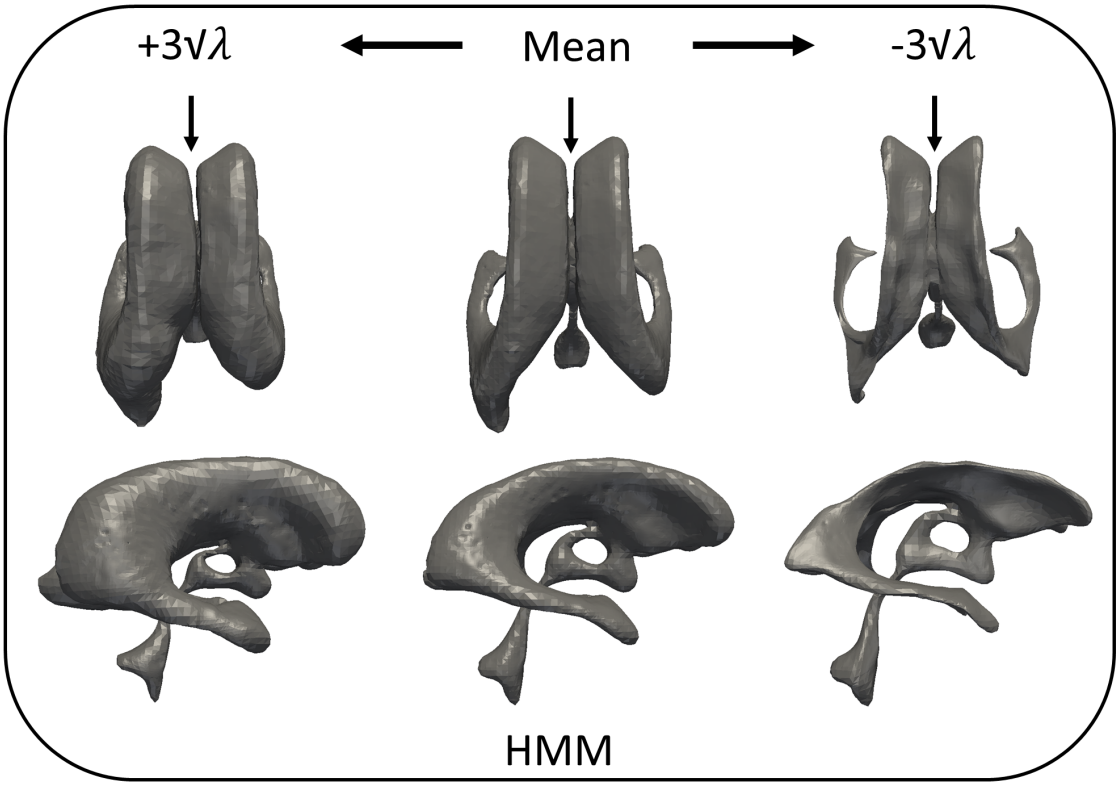

FIGURE 5.23: First mode of variation for ventricle SSM trained following registration using Fisher-HMM. λ represents the primary eigenvalue, used to constrain the SSM.

The ventricular surfaces depicted in Fig. 5.23, which represent the first mode of variation of the SSM trained following registration using HMM, were generated using Poisson surface reconstruction (Kazhdan and Hoppe, 2013). This

approach could be adopted as, the mean template estimated by the Fisher-HMM contained consistently oriented surface normal vectors, and positions, a fundamental requirement of the algorithm (available at: http://www.cs.jhu.edu/~misha/Code/PoissonRecon/Version9.01/), to reconstruct the surface of the mean shape. Surfaces were reconstructed for improved visualisation alone. For reference, the original point sets from which the surfaces were reconstructed, are presented in Appendix C (Fig. C.1). All quantitative measures of SSM quality were evaluated using the unstructured point sets sampled from the SSMs trained, following registration using each method. Surfaces describing the first mode of variation of SSMs, generated using samples registered by TMM-NR and gCPD (depicted in Figs. 5.24-5.25), were reconstructed by estimating signed distance maps (implicit surface representations) from the unstructured point sets. This was achieved using a geodesic active contour-based level set propagation approach (similar to (Zhao, Osher, and Fedkiw, 2001)), which considers the desired object boundary to represent the zero level iso-contour of the signed distance function. This approach to surface reconstruction was necessary due to the lack of orientation information distinguishing between the object's interior and exterior, required by the Poisson surface reconstruction algorithm. Although different approaches to surface reconstruction were used (resulting in the different degrees of surface smoothness visible in Figs. 5.24-5.25), the advantages identified for the HMM-based approach over TMM-NR and gCPD, with respect to preserving detailed anatomical features, were also reflected by the original unstructured point sets (as seen in Fig. 5.21, for example). Both reconstruction techniques resulted in accurate surface approximations to the raw point set data, and consequently, gain in performance in this regard, is attributed primarily to the registration approach employed.

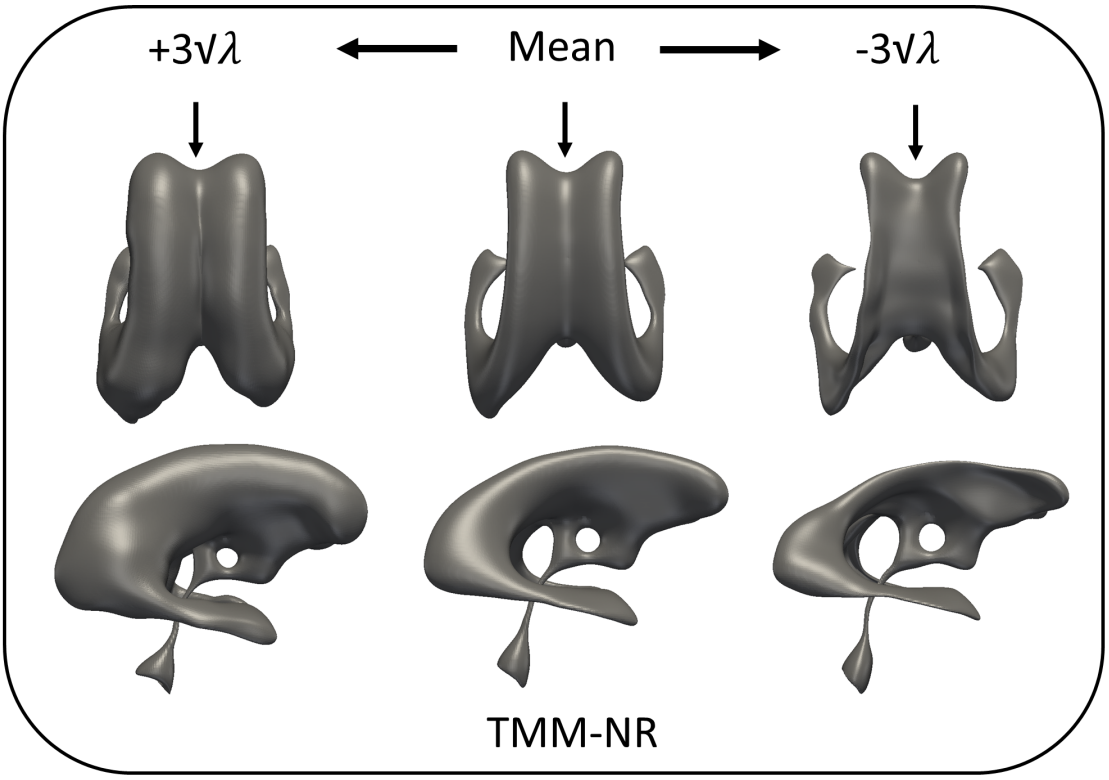

FIGURE 5.24: First mode of variation for ventricle SSM trained following registration using TMM-NR. λ represents the primary eigenvalue, used to constrain the SSM.

The first mode of variation estimated following group-wise registration of the ventricle samples using: HMM, TMM-NR and gCPD, is presented in Fig. 5.23, 5.24, 5.25, respectively. Arrows depicted in these images indicate the ability of the former to preserve the separation between the left and right lateral ventricles as expected, while TMM-NR and gCPD fail to so. The incorporation of surface normals as additional features to guide registration, using such an HMM, is consequently, advantageous in circumstances where position alone is insufficient as a descriptor. HMM-based registration using shapes represented as unstructured point sets with associated surface normal vectors, is thus inferred to establish correspondences with greater anatomical validity (particularly for shapes with complex topologies) than state-of-the-art point based approaches, especially advantageous in the context of generating statistical shape models (SSMs). The gain in registration performance afforded by the Fisher-HMM, shows promise for applications which involve anatomical structures with subtle and intricate variations in geometry, as encountered with vasculature in surgical navigation for example.

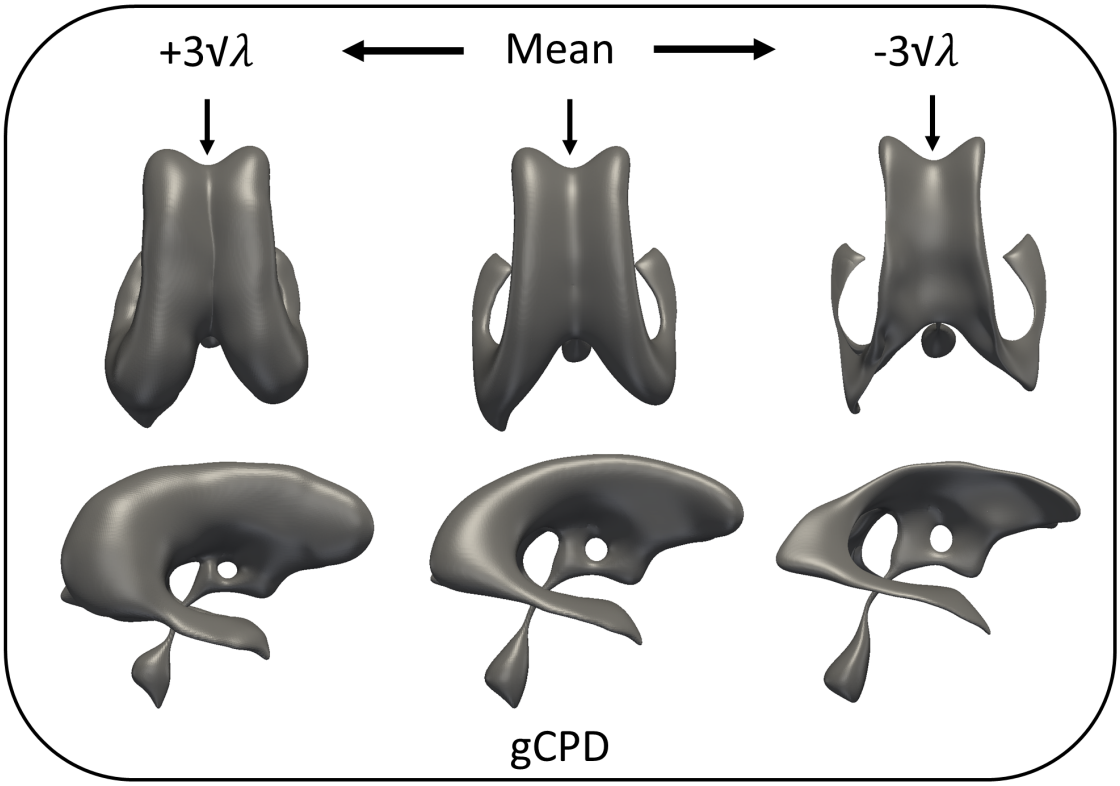

FIGURE 5.25: First mode of variation for ventricle SSM trained following registration using gCPD. λ represents the primary eigenvalue, used to constrain the SSM.

5.5 Conclusions

Two variants of a hybrid mixture model (HMM) for jointly registering and clustering generalised point sets comprising multi-dimensional features were presented in this chapter. The Watson-distribution based HMM was used to register hybrid point sets comprising spatial positions, fibre orientations, and FA values, derived from DTIs of multiple subjects. This approach was shown to model the observed fibre orientations and FA values accurately for all subjects within the HC group, for both WM ROIs, namely, the cingulum and corpus callosum. The ability of the proposed framework to model DTI-derived quantities for the AD and MCI groups was successful for the majority of cases, with two in the former and one in the latter, resulting in high errors. The mean group-specific templates estimated for the cingulum and corpus callosum, show comparable magnitudes and spatial distributions of mean FA values, relative to the state-of-the-art TBSS and VBM approaches. Group comparisons of FA values in the WM ROIs, using the proposed approach, highlighted significant reduction in FA for the AD and

MCI groups, relative to HC. The proposed method has potential for use in a variety of applications involving statistical analysis of diffusion data. Its generic and flexible nature also make it well suited to a variety of other computer vision and medical image analysis tasks, such as: point set registration with the integration of surface normals, joint registration and clustering of geometries with associated vector fields (estimated from bio-physical simulations for example); and texture mapping. This flexibility was demonstrated using the Fisher-distribution variant of the HMM, to register unstructured point sets (representing shapes) with associated surface normal vectors. Significant improvement in registration accuracy was achieved for the data set of ventricles (comprising samples from AD, MCI and HC subjects), relative to point-based state-of-art registration approaches. Furthermore, the Fisher-HMM preserved fine structural details and established correspondences with greater anatomical validity, relative to its point-based counterparts, namely, TMM-NR and gCPD (non-rigid). This was verified by quantitative and qualitative evaluation of SSM quality, highlighting the advantages afforded by the former, relative to the latter. These advantages and the fidelity and extensibility of the proposed framework is thus compelling, as a general tool for multi-dimensional medical image analysis.

Chapter 6

Conclusions

6.1 Summary of Main Outcomes

The focus of this thesis is on the formulation of a unified framework for automatic and robust registration of generalised point sets, enabling statistical analysis of shapes and other medical-image derived features of interest. Two specific objectives were outlined in this context: (1) developing a, group-wise, shape registration framework, able to accommodate: significant levels of noise and outliers, missing data, large non-linear variations in geometry without any topological constraints, and no prior information of homologous correspondences between shapes; and (2) generalising the first contribution to handle multi-dimensional unstructured point sets comprising disparate data features such as position, orientation and scalar-valued quantities. These were accomplished through formulation of a Student's t-mixture model-based group-wise registration framework and two variants of a hybrid mixture modelling framework combining: (1) Student's and Von-Mises-Fisher distributions; and (2) Student's t, Watson and Gaussian distributions; respectively, leading to the following outcomes:

- Group-wise registration using Student's t-distribution (TMM) offers significant improvement in registration accuracy in the presence of substantial proportions of outliers, relative to its Gaussian-based counterparts (**chapter** 3).

- Multi-resolution group-wise registration using Student's t-distributions (mrTMM) offers some improvement in registration accuracy, relative to TMM, and substantial improvement in computational efficiency (**chapter** 3).

- TMM and mrTMM require fewer user-specified parameters (when the shapes being registered contain significant proportions of outliers) for robust registration, than the state-of-the-art and, correspondingly, promote automatic analysis (**chapter** 3).
- TMM and mrTMM produce statistical shape models of higher or comparable quality to the state-of-the-art (**chapter** 4).
- The Watson distribution-based hybrid mixture model (HMM) was able to cluster DTI-derived data acquired from multiple subjects, enabling their statistical analysis across multiple subjects, and facilitating comparisons between patient groups (**chapter** 5).
- The Fisher distribution-based HMM employed to register hybrid point sets comprising positions with consistently oriented surface normals, improves registration accuracy, relative to conventional point-based approaches. It helps preserve shape topology and detailed anatomical features in complex geometries, while the latter are less successful in this regard.(**chapter** 5).

6.2 Limitations and Future Directions

The registration approaches proposed in this thesis, adopt a frequentist approach (maximum likelihood estimation) wherein, the mixture model variables are regarded as a discrete set of parameters that maximize the likelihood of the data being sampled from the model i.e. here uncertainties are expressed for the observed data in terms of posterior probabilities. A limitation of such an approach is the need for subsequent cross-validation experiments, to identify optimal model complexity for each data set (i.e. the optimal number of mixture components). Conversely, by adopting a Bayesian approach, model variables are regarded as probability distributions that generate the observed data (i.e. uncertainties are expressed over the variables), and optimal model complexity may be inferred directly from the data (Bishop, 2006). This provides an elegant alternative to conducting exhaustive cross validation studies to strike a balance between complexity and accuracy. Additionally, maximum likelihood estimation is locally optimum and consequently requires good initial estimates for the model parameters, while Bayesian approaches, through choice of suitable prior distributions for model variables, are less sensitive in this regard.

As highlighted in **chapter** 3, the non-rigid transformation (based on coherent point drift (CPD), (Myronenko and Song, 2010)) parametrized by Gaussian radial basis functions, employed in the proposed registration approaches, is insufficient to capture large localized deformations and articulations. Various methods to address this limitation include: non-parametric graph-matching based on Gaussian processes (Serradell et al., 2012); locally-affine deformation models, which permit up to 12 degrees of freedom at each point in the object being registered, (Feldmar and Ayache, 1996), (Amberg, Romdhani, and Vetter, 2007), (Cagniart, Boyer, and Ilic, 2010); and large deformation models that use shapes represented as currents in combination with diffeomorphic transformations (Durrleman et al., 2007), (Glaunes and Joshi, 2006), which ensure global consistency in the estimated deformation field. Among the proposed approaches, the Fisher-variant of the HMM (discussed in **chapter** 5) in particular, could benefit from incorporating locally affine transformations defined over both point positions and associated surface normal vectors. Locally defined transformations of this nature would consequently, attempt to match both positions and surface normal orientations in a local sense, facilitating large localized deformations. With such an approach however, it is essential to regularise the local transformations estimated, in order to preserve the global topology of the object.

Principal component analysis (PCA) is optimal in a least squares sense and consequently, sensitive to outliers. Its fundamental assumption of Gaussian-distributed data limits its applicability to groups of shapes that satisfy the same, which is often not the case for anatomical structures. Non-linearities resulting from significant variations in shapes and their representations, correspondingly, require statistical techniques that can model such variations. Suitable approaches include: Kernel-PCA (Twining and Taylor, 2001), where the orthogonal transformation of basis is performed on data mapped to a feature space (through choice of a suitable non-linear mapping, such as, a Gaussian kernel function for example), principal geodesic analysis (Fletcher et al., 2004), which describes shape variations on manifolds and is a generalization of PCA, mixtures of probabilistic PCA models (Gooya et al., 2015), among others. The latter in particular, is a viable extension to the proposed probabilistic registration framework, which would address the limitations of standard-PCA based SSMs.

The Watson-variant of the hybrid mixture model (HMM) proposed in **chapter** 5, could be imbued with greater flexibility using, 5-parameter Bingham distributions or general 8-parameter Fisher-Bingham distributions in place of Watsons, to model multi–fibre regions by fitting to orientation distribution functions (ODFs),

obtained from high angular diffusion images. Extensions to the Von-Mises-Fisher mixture model to accommodate antipodal symmetry, using a convex combinations of Fisher distributions, have previously been used to model diffusion ODFs (McGraw et al., 2006), (Kumar et al., 2008). The proposed approach could also be extended to model the full diffusion tensor within a probabilistic setting, facilitating the construction of statistical models and enabling group-wise analyses, of diffusion tensors (Fletcher and Joshi, 2007). Furthermore, the Watson-HMM could be improved by reformulating it within a multi-resolution framework, similarly to the approach described for shape registration (mrTMM) in **chapter** 3. This would aid in the localized refinement of clusters, particularly useful when considering large ROIs (such as the full WM volume), while retaining valuable information regarding the membership of newly formed clusters, to parent clusters, generated in the preceding resolution level. Such a framework is akin to hierarchical clustering and could improve clustering accuracy and sensitivity, beneficial to applications such as WM parcellation and automatic ROI-analyses of DTI-derived data.

Appendix A

Derivations for TMM-based group-wise rigid registration

M-step update equations for t-mixture model parameters, presented in **chapter** 3, section 3.2.3, equations (3.10-3.16), are derived by maximizing the complete data log-likelihood Q with respect to each model parameter as follows:

- Estimation of TMM centroids $\boldsymbol{\mu}_j$ at the $(t+1)^{\text{th}}$ EM-iteration:

$$Q(\Psi^{t+1}|\Psi^t) = -\frac{1}{2}\sum_{k,i,j} P_{kij}^{\star t}\Delta_{kij} + O.T. \tag{A.1a}$$

$$\Delta_{kij} = \frac{(\mathbf{x}_{ki} - s_k\mathbf{R}_k\boldsymbol{\mu}_j - \mathbf{t}_k)^T(\mathbf{x}_{ki} - s_k\mathbf{R}_k\boldsymbol{\mu}_j - \mathbf{t}_k)}{\sigma^2} \tag{A.1b}$$

$O.T.$ summarizes terms in Q independent of $\boldsymbol{\mu}_j$.

$$< \partial Q, \partial\boldsymbol{\mu}_j >= [-\frac{1}{2}\sum_{k,i} P_{kij}^{\star}\Delta_{kij}^{\boldsymbol{\mu}_j+\partial\boldsymbol{\mu}_j}] - [-\frac{1}{2}\sum_{k,i} P_{kij}^{\star}\Delta_{kij}^{\boldsymbol{\mu}_j}] \tag{A.2a}$$

$$< \partial Q, \partial\boldsymbol{\mu}_j >= \sum_{k,i} P_{kij}^{\star}[(\mathbf{x}_{ki} - s_k\mathbf{R}_k\boldsymbol{\mu}_j - \mathbf{t}_k)^T s_k\mathbf{R}_k]\partial\boldsymbol{\mu}_j \tag{A.2b}$$

$$< \partial Q, \partial\boldsymbol{\mu}_j >= 0 \implies \sum_{k,i} P_{kij}^{\star}[(\mathbf{x}_{ki} - s_k\mathbf{R}_k\boldsymbol{\mu}_j - \mathbf{t}_k)^T s_k\mathbf{R}_k] = 0 \tag{A.2c}$$

$$\sum_{k,i} P_{kij}^{\star} s_k\mathbf{R}_k^T(\mathbf{x}_{ki} - \mathbf{t}_k) = \sum_{k,i} P_{kij}^{\star} s_k\mathbf{R}_k^T\mathbf{R}_k s_k\boldsymbol{\mu}_j \tag{A.2d}$$

$$\boldsymbol{\mu}_j = \frac{\sum_{k,i} P_{kij}^{\star} s_k^{-1}\mathbf{R}^T(\mathbf{x}_{ki} - \mathbf{t}_k)}{\sum_{k,i} P_{kij}^{\star}} \tag{A.2e}$$

- Estimation of model variance σ^2:

$$\frac{\partial Q}{\partial \sigma^2} = \frac{\partial \sum_{k,i,j}[-\frac{P_{kij}}{2}[\log(\sigma^6)] - \frac{P^{\star}_{kij}}{2}[\Delta_{kij}]]}{\partial \sigma^2} = 0 \tag{A.3a}$$

$$\implies \sum_{k,i,j} -P_{kij}\frac{3}{\sigma} + P^{\star}_{kij}\frac{(\mathbf{x}_{ki} - s_k\mathbf{R}_k\boldsymbol{\mu}_j - \mathbf{t}_k)^T(\mathbf{x}_{ki} - s_k\mathbf{R}_k\boldsymbol{\mu}_j - \mathbf{t}_k)}{\sigma^3} = 0 \tag{A.3b}$$

$$\sigma^2 = \frac{\sum_{k,i,j} P^{\star}_{kij}(\mathbf{x}_{ki} - s_k\mathbf{R}_k\boldsymbol{\mu}_j - \mathbf{t}_k)^T(\mathbf{x}_{ki} - s_k\mathbf{R}_k\boldsymbol{\mu}_j - \mathbf{t}_k)}{3\sum_{kij} P_{kij}} \tag{A.3c}$$

- Estimation of translation $\mathbf{t}_k$:

$$< \partial Q, \partial \mathbf{t}_k >= [-\frac{1}{2}\sum_{i,j} P^{\star}_{kij}\Delta^{\mathbf{t}_k+\partial\mathbf{t}_k}_{kij}] - [-\frac{1}{2}\sum_{i,j} P^{\star}_{kij}\Delta^{\mathbf{t}_k}_{kij}] \tag{A.4a}$$

$$< \partial Q, \partial \mathbf{t}_k >= \sum_{i,j} P^{\star}_{kij}[(\mathbf{x}_{ki} - s_k\mathbf{R}_k\boldsymbol{\mu}_j - \mathbf{t}_k)^T]\partial\mathbf{t}_k \tag{A.4b}$$

$$< \partial Q, \partial \mathbf{t}_k >= 0 \implies \sum_{i,j} P^{\star}_{kij}(\mathbf{x}_{ki} - s_k\mathbf{R}_k\boldsymbol{\mu}_j)^T = \sum_{i,j} P^{\star}_{kij}\mathbf{t}_k^T \tag{A.4c}$$

$$\mathbf{t}_k = \frac{\sum_{i,j} P^{\star}_{kij}\mathbf{x}_{ki}}{\sum_{i,j} P^{\star}_{kij}} - s_k\mathbf{R}_k\frac{\sum_{i,j} P^{\star}_{kij}\boldsymbol{\mu}_j}{\sum_{i,j} P^{\star}_{kij}} \tag{A.4d}$$

Setting the first term as $\mathbf{d}_k$ and the second term as $\mathbf{m}_k$ (refer to equations 3.18 - 3.19) we get:

$$\mathbf{t}_k = \mathbf{d}_k - s_k\mathbf{R}_k\mathbf{m}_k \tag{A.4e}$$

- Estimation of strictly orthogonal rotation $\mathbf{R}_k$: Using the lemma outlined in (Myronenko and Song, 2010), the optimal rotation matrix maximises $\mathrm{tr}(\mathbf{C}_k^T\mathbf{R}_k)$ where $\mathbf{C}_k$ represents a real covariance matrix (refer to equation A.5d).

$$\tilde{\mathbf{x}}_{ki} = \mathbf{x}_{ki} - \mathbf{d}_k, \tilde{\mathbf{m}}_{kj} = \boldsymbol{\mu}_j - \mathbf{m}_k \tag{A.5a}$$

Using equations (A.4e) and (A.5a) we get:

$$Q(\Psi^{t+1}|\Psi^t) \propto \sum_{i,j} P^{\star t}_{kij}(\tilde{\mathbf{x}}_{ki}^T\mathbf{R}_k\tilde{\mathbf{m}}_{kj}) \tag{A.5b}$$

$$Q(\Psi^{t+1}|\Psi^t) \propto \sum_{i,j} P^{\star t}_{kij} \operatorname{tr}[\tilde{\mathbf{m}}_{kj}\tilde{\mathbf{x}}^T_{ki}\mathbf{R}_k] \tag{A.5c}$$

As equation (A.5c) must be maximised with respect to $\mathbf{R}_k$,

$$\mathbf{C}_k = \sum_{i,j} P^{\star}_{kij}\tilde{\mathbf{x}}_{ki}\tilde{\mathbf{m}}^T_{kj} \tag{A.5d}$$

$\mathbf{R}_k = \mathbf{USV}^T$, where $\mathbf{U}, \mathbf{V}$ are unitary matrices computed by singular value decomposition of $\mathbf{C}_k$ and $\mathbf{S} = diag(1, 1, det(\mathbf{UV}^T))$ is a diagonal matrix that prevents reflections.

- Estimation of scaling s_k:

$$\frac{\partial Q}{\partial s_k} = -\frac{1}{2}\frac{\partial \sum_{i,j} P^{\star}_{kij}\Delta_{kij}}{\partial s_k} = 0 \tag{A.6a}$$

$$\sum_{i,j} P^{\star}_{kij}\frac{(\tilde{\mathbf{x}}_{ki} - s_k\mathbf{R}_k\tilde{\mathbf{m}}_{kj})^T(\mathbf{R}_k\tilde{\mathbf{m}}_{kj})}{\sigma^2} = 0 \tag{A.6b}$$

$$\sum_{i,j} P^{\star}_{kij}[(\tilde{\mathbf{x}}_{ki})^T(\mathbf{R}_k\tilde{\mathbf{m}}_{kj})] = s_k\sum_{i,j} P^{\star}_{kij}[\tilde{\mathbf{m}}^T_{kj}\mathbf{R}^T_k\mathbf{R}_k\tilde{\mathbf{m}}_{kj}] \tag{A.6c}$$

$$s_k = \frac{\operatorname{tr}[\tilde{\mathbf{m}}_{kj}\tilde{\mathbf{x}}^T_{ki}]\mathbf{R}_k}{\operatorname{tr}[\tilde{\mathbf{m}}_{kj}\tilde{\mathbf{m}}^T_{kj}]} = \frac{\operatorname{tr}[\mathbf{C}^T_k\mathbf{R}_k]}{\operatorname{tr}[\tilde{\mathbf{m}}_{kj}\tilde{\mathbf{m}}^T_{kj}]} \tag{A.6d}$$

- Estimation of degrees of freedom ν_j:

$$\begin{aligned} Q(\Psi^{t+1}|\Psi^t) = \sum_{k,i,j} P^t_{kij}[-\log\Gamma(\frac{\nu_j}{2}) + \frac{1}{2}\nu_j\log(\frac{\nu_j}{2}) + \\ \frac{\nu_j}{2}[\log(U^t_{kij}) - U^t_{kij} + \Psi(\frac{\nu_j + D}{2}) - \log(\frac{\nu^t_j + D}{2})]] + O.T. \end{aligned} \tag{A.7a}$$

$O.T.$ summarizes terms in Q independent of ν_j.

$$\begin{aligned} \frac{\partial Q}{\partial \nu_j} = -\Psi(\frac{\nu_j}{2}) + \log(\frac{\nu_j}{2}) + 1 + \frac{1}{\sum_{k,i} P^t_{kij}}\sum_{k,i} P^t_{kij}(\log(U^t_{kij}) - U^t_{kij}) + \\ \Psi(\frac{\nu^t_j + D}{2}) - \log(\frac{\nu^t_j + D}{2}) = 0 \end{aligned} \tag{A.7b}$$

Equation A.7(b) is solved using Newton's method to estimate the degrees of freedom ν_j.

Appendix B

Derivations for HMM-based group-wise registration of generalised point sets

- Derivations for the M-step updates (refer to equations equations (5.3c - 5.3e)) of the mean fibre orientation $\mathbf{m}_j^d$ and fibre concentration κ_j parameters associated with Watson distributions in the HMM, presented in section 5.2.4 of **chapter** 5, are derived by maximizing the complete data log-likelihood Q (refer to equation B.1a), with respect to each model parameter as follows: (Here $M(\kappa_j)$ denotes the Kummer function).

$$Q(\Theta_n^{t+1}|\Theta_n^t) = \sum_{k=1}^{K}\sum_{i=1}^{N_k}\sum_{j=1}^{M} P_{kij}\log p(\pm\mathbf{n}_{ki}|\mathbf{m}_j^d,\kappa_j) + \lambda_j(1-\mathbf{m}_j^{dT}\mathbf{m}_j^d) \quad \text{(B.1a)}$$

$$< \partial Q, \partial\mathbf{m}_j^d >= 0 \implies \lambda_j\mathbf{m}_j^d = \kappa_j\sum_{k=1}^{K}\sum_{i=1}^{N_k} P_{kij}(\mathbf{n}_{ki}^T\mathbf{m}_j^d)\mathbf{n}_{ki} \quad \text{(B.1b)}$$

$$< \partial Q, \partial\kappa_j >= 0 \implies \frac{M'(\kappa_j)}{M(\kappa_j)}\sum_{k=1}^{K}\sum_{i=1}^{N_k} P_{kij} = \sum_{k=1}^{K}\sum_{i=1}^{N_k} P_{kij}(\mathbf{n}_{ki}^T\mathbf{m}_j^d)^2 \quad \text{(B.1c)}$$

$$\mathbf{m}_j^{dT}\mathbf{m}_j^d = 1 \implies \lambda_j = \kappa_j||\sum_{k=1}^{K}\sum_{i=1}^{N_k} P_{kij}(\mathbf{n}_{ki}^T\mathbf{m}_j^d)\mathbf{n}_{ki}|| \quad \text{(B.1d)}$$

Substituting equation (B.1d) in (B.1b) results in a non-linear equation (B.2), which is solved numerically by fixed-point iteration.

$$\mathbf{m}_j^d = \frac{\sum_{k=1}^{K}\sum_{i=1}^{N_k} P_{kij}(\mathbf{n}_{ki}^T\mathbf{m}_j^d)\mathbf{n}_{ki}}{||\sum_{k=1}^{K}\sum_{i=1}^{N_k} P_{kij}(\mathbf{n}_{ki}^T\mathbf{m}_j^d)\mathbf{n}_{ki}||} \tag{B.2}$$

Based on equation (B.1c), the ratio of the derivative of the Kummer function to the function itself, is expressed as shown in equation (B.3a). As noted in **chapter** 5, this ratio may be expressed as a continued fraction, as shown in equation (B.3b). Consequently, using equations (B.3a) and (B.3b), the concentration parameters κ_j can be approximated as shown in equation (B.3d), by solving the linear equation (B.3c) (similarly to (Bijral, Breitenbach, and Grudic, 2007)).

$$\frac{M'(\kappa_j)}{M(\kappa_j)} = \frac{\sum_{k=1}^{K}\sum_{i=1}^{N_k} P_{kij}(\mathbf{n}_{ki}^T\mathbf{m}_j^d)^2}{\sum_{k=1}^{K}\sum_{i=1}^{N_k} P_{kij}} \tag{B.3a}$$

$$\frac{\kappa_j M'(\kappa_j)}{M(\kappa_j)} = \frac{\kappa_j/2}{(D/2) - \kappa_j + \frac{(3/2)\kappa_j}{(\frac{D}{2}+1)-\kappa_j+....}} \tag{B.3b}$$

$$\frac{\kappa_j M'(\kappa_j)}{M(\kappa_j)} \approx \frac{\kappa_j/2}{(D/2) - \kappa_j + \frac{\kappa_j M'(\kappa_j)}{M(\kappa_j)}} \tag{B.3c}$$

$$\kappa_j \approx \frac{1}{2}\Big[\frac{1 - \frac{M'(\kappa_j)}{M(\kappa_j)}D}{(\frac{M'(\kappa_j)}{M(\kappa_j)})^2 - \frac{M'(\kappa_j)}{M(\kappa_j)}}\Big] \tag{B.3d}$$

- Derivations for the M-step updates (refer to equations equations (5.5b - 5.5c)) of the mean direction $\mathbf{m}_j^d$ and concentration parameters κ_j, associated with the Fisher distributions in the HMM, presented in **chapter** 5, section 5.2.5, are derived by maximizing the complete data log-likelihood Q (refer to equation B.4a), with respect to each model parameter as follows:

$$Q(\Theta_n^{t+1}|\Theta_n^t) = \sum_{k=1}^{K}\sum_{i=1}^{N_k}\sum_{j=1}^{M} P_{kij}\log p(\mathbf{n}_{ki}|\mathbf{m}_j^d, \kappa_j) \tag{B.4a}$$
$$+ \lambda_j(1 - \mathbf{m}_j^{dT}\mathbf{m}_j^d)$$

$$< \partial Q, \partial \mathbf{m}_j^d >= 0 \implies 2\lambda_j \mathbf{m}_j^d = \kappa_j \sum_{k=1}^{K} \sum_{i=1}^{N_k} P_{kij} \mathbf{n}_{ki} \tag{B.4b}$$

$$\mathbf{m}_j^{dT} \mathbf{m}_j^d = 1 \implies \lambda_j = \frac{\kappa_j}{2} || \sum_{k=1}^{K} \sum_{i=1}^{N_k} P_{kij} \mathbf{n}_{ki} || \tag{B.4c}$$

$$\mathbf{m}_j^d = \frac{\sum_{k=1}^{K} \sum_{i=1}^{N_k} P_{kij} \mathbf{n}_{ki}}{|| \sum_{k=1}^{K} \sum_{i=1}^{N_k} P_{kij} \mathbf{n}_{ki} ||} \tag{B.4d}$$

Differentiating Q with respect to κ_j and equating to zero (as shown in equation B.4e) and using the result presented in equation (B.4f), results in the non-linear equation (B.4g). Subsequently, κ_j are estimated numerically from equation (B.4g), by fixed-point iteration.

$$\frac{\partial}{\partial \kappa_j} \Big[\sum_{k=1}^{K} \sum_{i=1}^{N_k} P_{kij} [\kappa_j \mathbf{m}_j^{dT} \mathbf{n}_{ki} - \log \frac{4\pi \sinh(\kappa_j)}{\kappa_j}] \Big] = 0 \tag{B.4e}$$

$$\frac{\partial}{\partial \kappa_j} \log \frac{4\pi \sinh(\kappa_j)}{\kappa_j} = \coth(\kappa_j) - \frac{1}{\kappa_j} \tag{B.4f}$$

$$\frac{1}{\kappa_j} = \coth(\kappa_j) - \frac{\mathbf{m}_j^{dT} \sum_{k=1}^{K} \sum_{i=1}^{N_k} P_{kij} \mathbf{n}_{ki}}{\sum_{k=1}^{K} \sum_{i=1}^{N_k} P_{kij}} \tag{B.4g}$$

Appendix C

Supplementary Material

TABLE C.1: Sensitivity of registration accuracy of gCPD to varying uniform distribution weights w for the femur data set.

Femur ($K = 1000, M = 320$)							
$w = 0.1$		$w = 0.3$		$w = 0.5$		$w = 0.7$	
HD (mm.)	MSD (mm.)	HD (mm.)	MSD (mm.)	HD (mm.)	MSD (mm.)	HD (mm.)	MSD (mm.)
13.27 $\pm$ 3.56	2.56 $\pm$ 1.09	13.13$\pm$ 3.49	2.54 $\pm$ 1.08	**12.84** $\pm$ **3.42**	2.53 $\pm$ 1.08	**12.76** $\pm$ **3.50**	2.51 $\pm$ 1.09

The results presented in Table C.1 indicate that weight values of $w = 0.5, 0.7$ for the constituent uniform distribution component in gCPD, achieved significantly lower registration errors than $w = 0.5, 0.7$, for the femur data set. These are highlighted in bold. For reference, using $M = 320$ mixture components, the proposed TMM approach achieved significantly lower errors of: HD = 9.90 ± 5.26 and MSD = 2.17 ± 0.91, for the same data set.

TABLE C.2: Summary of generalisation and specificity experiments used to evaluate SSM quality.

Experiment	**Evaluation Method**
SSM quality w.r.t number of mixture components	10-fold cross validation experiments conducted. MSD metric was evaluated between ground truth test shapes and SSM-predicted shapes. Unseen test shapes were chosen either from different cohorts (hippocampi); or from the same cohort (heart and femur). The chosen test samples for all data sets were 'unseen' shapes as they were not included in the training set, during the initial registration step.
SSM quality w.r.t number of modes of variation	Full-fold cross-validation experiments conducted. MSD metric was evaluated between ground truth test shapes and SSM-predicted shapes for the hippocampi and heart data sets. MSD errors were evaluated between the correspondences estimated for each test shape and the SSM-predicted shape for femur data set. Correspondences were estimated for all test shapes together with the training set, during the initial registration step.

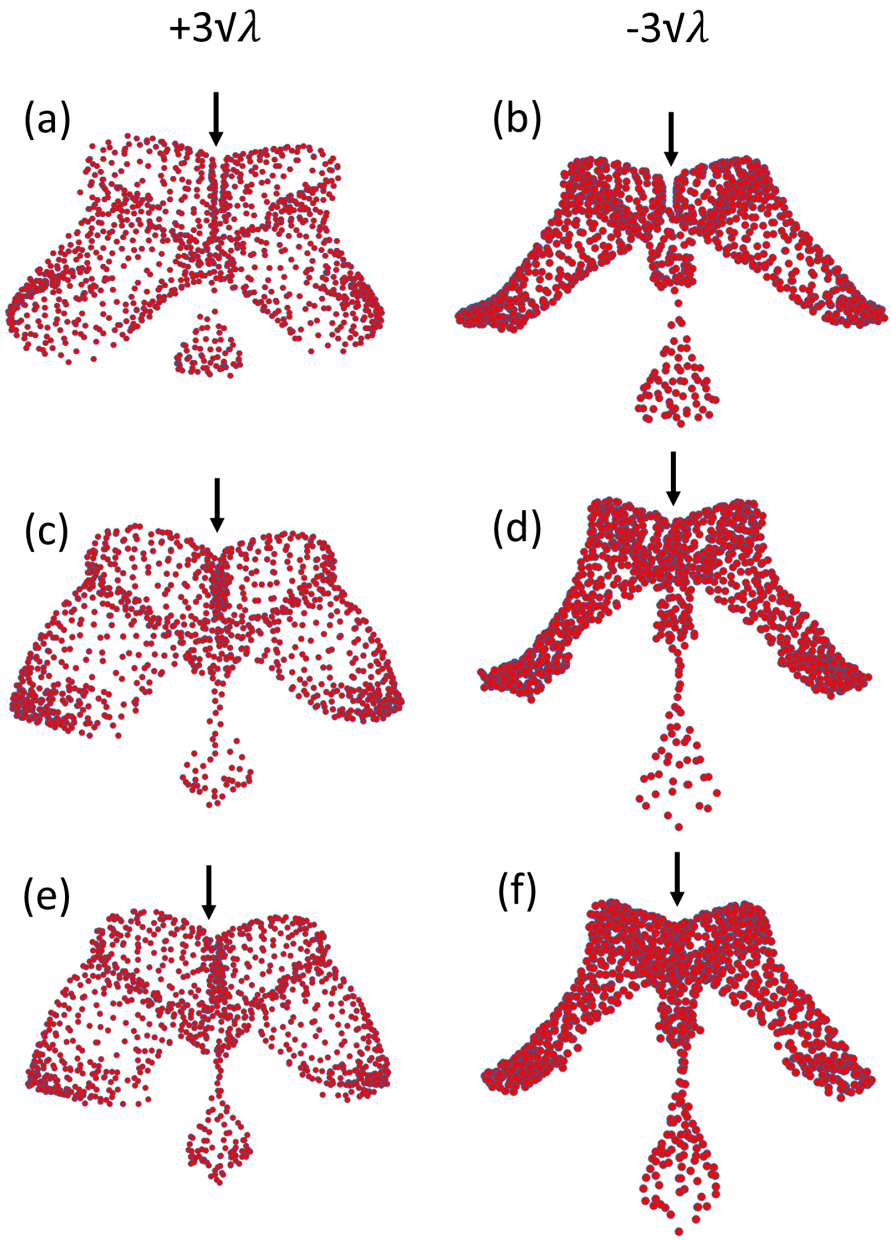

FIGURE C.1: First mode of variation for ventricle SSM trained following registration using: (a,b) Fisher-HMM; (c,d) TMM-NR; and (e,f) gCPD. λ represents the primary eigenvalue, used to constrain the SSM. Separation between the left and right ventricular bodies is clearly visible in (a,b) illustrating the advantage offered by the Fisher-HMM registration framework over TMM-NR and gCPD.

Bibliography

Albà, Xènia et al. (2014). "Reusability of statistical shape models for the segmentation of severely abnormal hearts". In: *International Workshop on Statistical Atlases and Computational Models of the Heart*. Springer, pp. 257–264.

Alzheimer's Association et al. (2016). "2016 Alzheimer's disease facts and figures". In: *Alzheimer's & Dementia* 12.4, pp. 459–509.

Amberg, Brian, Sami Romdhani, and Thomas Vetter (2007). "Optimal step nonrigid icp algorithms for surface registration". In: *2007 IEEE Conference on Computer Vision and Pattern Recognition*. IEEE, pp. 1–8.

Ashburner, John and Karl J Friston (2000). "Voxel-based morphometry — the methods". In: *Neuroimage* 11.6, pp. 805–821.

Banerjee, Arindam et al. (2005). "Clustering on the unit hypersphere using von Mises-Fisher distributions". In: *Journal of Machine Learning Research* 6.Sep, pp. 1345–1382.

Barnes, Josephine et al. (2004). "Differentiating AD from aging using semiautomated measurement of hippocampal atrophy rates". In: *Neuroimage* 23.2, pp. 574–581.

Basser, Peter J, James Mattiello, and Denis LeBihan (1994). "Estimation of the effective self-diffusion tensor from the NMR spin echo". In: *Journal of Magnetic Resonance, Series B* 103.3, pp. 247–254.

Belongie, Serge, Jitendra Malik, and Jan Puzicha (2002). "Shape matching and object recognition using shape contexts". In: *IEEE transactions on pattern analysis and machine intelligence* 24.4, pp. 509–522.

Benjamini, Yoav and Daniel Yekutieli (2001). "The control of the false discovery rate in multiple testing under dependency". In: *Annals of statistics*, pp. 1165–1188.

Besl, Paul J and Neil D McKay (1992). "A Method for Registration of 3-D Shapes". In: *IEEE Transactions on Pattern Analysis and Machine Intelligence* 14.2, pp. 239–256.

Bijral, Avleen Singh, Markus Breitenbach, and Gregory Z Grudic (2007). "Mixture of Watson Distributions: A Generative Model for Hyperspherical Embeddings." In: *AISTATS*, pp. 35–42.

Billings, Seth and Russell Taylor (2014). "Iterative most likely oriented point registration". In: *International Conference on Medical Image Computing and Computer-Assisted Intervention*. Springer, pp. 178–185.

— (2015). "Generalized iterative most likely oriented-point (G-IMLOP) registration". In: *International journal of computer assisted radiology and surgery* 10.8, pp. 1213–1226.

Bishop, Christopher M (2006). "Pattern recognition". In: *Machine Learning* 128.

Brechbühler, Ch, Guido Gerig, and Olaf Kübler (1995). "Parametrization of closed surfaces for 3-D shape description". In: *Computer vision and image understanding* 61.2, pp. 154–170.

Cagniart, Cedric, Edmond Boyer, and Slobodan Ilic (2010). "Probabilistic deformable surface tracking from multiple videos". In: *European conference on computer vision*. Springer, pp. 326–339.

Cardoso, M Jorge et al. (2015). "Geodesic information flows: spatially-variant graphs and their application to segmentation and fusion". In: *IEEE transactions on medical imaging* 34.9, pp. 1976–1988.

Castro-Mateos, Isaac et al. (2015). "Statistical interspace models (SIMs): application to robust 3D spine segmentation". In: *IEEE transactions on medical imaging* 34.8, pp. 1663–1675.

Cates, Joshua et al. (2007). "Shape modeling and analysis with entropy-based particle systems". In: *Biennial International Conference on Information Processing in Medical Imaging*. Springer, pp. 333–345.

Cercignani, Mara et al. (2001). "Mean diffusivity and fractional anisotropy histograms of patients with multiple sclerosis". In: *American Journal of Neuroradiology* 22.5, pp. 952–958.

Chang, Lin-Ching, Lindsay Walker, and Carlo Pierpaoli (2012). "Informed RESTORE: a method for robust estimation of diffusion tensor from low redundancy datasets in the presence of physiological noise artifacts". In: *Magnetic resonance in medicine* 68.5, pp. 1654–1663.

Chen, Ting et al. (2010). "Group-wise point-set registration using a novel CDF-based Havrda-Charvát divergence". In: *International journal of computer vision* 86.1, pp. 111–124.

Chui, Haili and Anand Rangarajan (2003). "A new point matching algorithm for non-rigid registration". In: *Computer Vision and Image Understanding* 89.2, pp. 114–141.

Clements, Logan W et al. (2008). "Robust surface registration using salient anatomical features for image-guided liver surgery: algorithm and validation". In: *Medical physics* 35.6, pp. 2528–2540.

Cootes, Timothy F et al. (1995). "Active shape models-their training and application". In: *Computer vision and image understanding* 61.1, pp. 38–59.

Davies, Rhodri H et al. (2002). "A minimum description length approach to statistical shape modeling". In: *IEEE Transactions on Medical Imaging* 21.5, pp. 525–537.

Davies, Rhodri H et al. (2010). "Building 3-d statistical shape models by direct optimization". In: *IEEE Transactions on Medical Imaging* 29.4, pp. 961–981.

Dempster, Arthur P, Nan M Laird, and Donald B Rubin (1977). "Maximum likelihood from incomplete data via the EM algorithm". In: *Journal of the royal statistical society. Series B (methodological)*, pp. 1–38.

Durrleman, Stanley et al. (2007). "Measuring brain variability via sulcal lines registration: a diffeomorphic approach". In: *International Conference on Medical Image Computing and Computer-Assisted Intervention*. Springer, pp. 675–682.

— (2009). "Statistical models of sets of curves and surfaces based on currents". In: *Medical image analysis* 13.5, pp. 793–808.

Durrleman, Stanley et al. (2011). "Registration, atlas estimation and variability analysis of white matter fiber bundles modeled as currents". In: *NeuroImage* 55.3, pp. 1073–1090.

Evangelidis, Georgios D et al. (2014). "A generative model for the joint registration of multiple point sets". In: *European Conference on Computer Vision*. Springer, pp. 109–122.

Evans, Alan C et al. (2012). "Brain templates and atlases". In: *Neuroimage* 62.2, pp. 911–922.

Feldmar, Jacques and Nicholas Ayache (1996). "Rigid, affine and locally affine registration of free-form surfaces". In: *International journal of computer vision* 18.2, pp. 99–119.

Ferrarini, Luca et al. (2006). "Shape differences of the brain ventricles in Alzheimer's disease". In: *NeuroImage* 32.3, pp. 1060–1069.

Fischl, Bruce, Martin I Sereno, and Anders M Dale (1999). "Cortical surface-based analysis: II: inflation, flattening, and a surface-based coordinate system". In: *Neuroimage* 9.2, pp. 195–207.

Fisher, Nicholas I, Toby Lewis, and Brian JJ Embleton (1987). *Statistical analysis of spherical data*. Cambridge university press.

Fletcher, P Thomas and Sarang Joshi (2007). "Riemannian geometry for the statistical analysis of diffusion tensor data". In: *Signal Processing* 87.2, pp. 250–262.

Fletcher, P Thomas et al. (2004). "Principal geodesic analysis for the study of nonlinear statistics of shape". In: *IEEE transactions on medical imaging* 23.8, pp. 995–1005.

Frangi, Alejandro F et al. (2002). "Automatic construction of multiple-object three-dimensional statistical shape models: Application to cardiac modeling". In: *IEEE transactions on medical imaging* 21.9, pp. 1151–1166.

Frisoni, GB et al. (2002). "Detection of grey matter loss in mild Alzheimer's disease with voxel based morphometry". In: *Journal of Neurology, Neurosurgery & Psychiatry* 73.6, pp. 657–664.

Gelfand, Natasha et al. (2005). "Robust global registration". In: *Symposium on geometry processing*. Vol. 2. 3, p. 5.

Gerig, Guido et al. (2001a). "Shape analysis of brain ventricles using spharm". In: *Mathematical Methods in Biomedical Image Analysis, 2001. MMBIA 2001. IEEE Workshop on*. IEEE, pp. 171–178.

Gerig, Guido et al. (2001b). "Shape versus size: Improved understanding of the morphology of brain structures". In: *International Conference on Medical Image Computing and Computer-Assisted Intervention*. Springer, pp. 24–32.

Gerogiannis, Demetrios, Christophoros Nikou, and Aristidis Likas (2009). "The mixtures of Student's t-distributions as a robust framework for rigid registration". In: *Image and Vision Computing* 27.9, pp. 1285–1294.

Glaunes, Joan Alexis and Sarang Joshi (2006). "Template estimation form unlabeled point set data and surfaces for computational anatomy". In: *1st MICCAI Workshop on Mathematical Foundations of Computational Anatomy: Geometrical, Statistical and Registration Methods for Modeling Biological Shape Variability*.

Gooya, Ali, Christos Davatzikos, and Alejandro F Frangi (2015). "A Bayesian approach to sparse model selection in statistical shape models". In: *SIAM Journal on Imaging Sciences* 8.2, pp. 858–887.

Gooya, Ali et al. (2015). "Joint clustering and component analysis of correspondenceless point sets: application to cardiac statistical modeling". In: *International Conference on Information Processing in Medical Imaging*. Springer, pp. 98–109.

Gower, John C (1975). "Generalized procrustes analysis". In: *Psychometrika* 40.1, pp. 33–51.

Granger, Sébastien and Xavier Pennec (2002). "Multi-scale EM-ICP: A fast and robust approach for surface registration". In: *European Conference on Computer Vision*. Springer, pp. 418–432.

Hammers, Alexander et al. (2003). "Three-dimensional maximum probability atlas of the human brain, with particular reference to the temporal lobe". In: *Human brain mapping* 19.4, pp. 224–247.

Hammers, Alexander et al. (2007). "Statistical neuroanatomy of the human inferior frontal gyrus and probabilistic atlas in a standard stereotaxic space". In: *Human brain mapping* 28.1, pp. 34–48.

Hayashi, Yuichiro et al. (2016). "Progressive internal landmark registration for surgical navigation in laparoscopic gastrectomy for gastric cancer". In: *International journal of computer assisted radiology and surgery* 11.5, pp. 837–845.

Heimann, Tobias and Hans-Peter Meinzer (2009). "Statistical shape models for 3D medical image segmentation: a review". In: *Medical image analysis* 13.4, pp. 543–563.

Hermans, Jeroen et al. (2011). "Robust point set registration using EM-ICP with information-theoretically optimal outlier handling". In: *Computer Vision and Pattern Recognition (CVPR), 2011 IEEE Conference on*. IEEE, pp. 2465–2472.

Horaud, Radu et al. (2011). "Rigid and articulated point registration with expectation conditional maximization". In: *IEEE Transactions on Pattern Analysis and Machine Intelligence* 33.3, pp. 587–602.

Hua, Kegang et al. (2008). "Tract probability maps in stereotaxic spaces: analyses of white matter anatomy and tract-specific quantification". In: *Neuroimage* 39.1, pp. 336–347.

Hufnagel, Heike et al. (2007). "Point-based statistical shape models with probabilistic correspondences and affine EM-ICP". In: *Bildverarbeitung für die Medizin 2007*. Springer, pp. 434–438.

Hufnagel, Heike et al. (2008). "Generation of a statistical shape model with probabilistic point correspondences and the expectation maximization-iterative closest point algorithm". In: *International Journal of Computer Assisted Radiology and Surgery* 2.5, pp. 265–273.

Hufnagel, Heike et al. (2009). "Computation of a probabilistic statistical shape model in a maximum-a-posteriori framework". In: *Methods Inf Med* 48.4, pp. 314–9.

Huynh, Du Q (2009). "Metrics for 3D rotations: Comparison and analysis". In: *Journal of Mathematical Imaging and Vision* 35.2, pp. 155–164.

Jian, Bing and Baba C Vemuri (2005). "A robust algorithm for point set registration using mixture of Gaussians". In: *Tenth IEEE International Conference on Computer Vision (ICCV'05) Volume 1*. Vol. 2. IEEE, pp. 1246–1251.

— (2011). "Robust point set registration using gaussian mixture models". In: *IEEE Transactions on Pattern Analysis and Machine Intelligence* 33.8, pp. 1633–1645.

Jolliffe, Ian T (2002). *Introduction*. Springer.

Jupp, PE and KV Mardia (1989). "A unified view of the theory of directional statistics, 1975-1988". In: *International Statistical Review/Revue Internationale de Statistique*, pp. 261–294.

Kazhdan, Michael and Hugues Hoppe (2013). "Screened poisson surface reconstruction". In: *ACM Transactions on Graphics (TOG)* 32.3, p. 29.

Kendall, David G (1989). "A survey of the statistical theory of shape". In: *Statistical Science*, pp. 87–99.

Koikkalainen, Juha et al. (2008). "Methods of artificial enlargement of the training set for statistical shape models". In: *IEEE Transactions on Medical Imaging* 27.11, pp. 1643–1654.

Kumar, Ritwik et al. (2008). "Multi-fiber reconstruction from DW-MRI using a continuous mixture of von Mises-Fisher distributions". In: *Computer Vision and Pattern Recognition Workshops, 2008. CVPRW'08. IEEE Computer Society Conference on*. IEEE, pp. 1–8.

Lange, Thomas et al. (2009). "3D ultrasound-CT registration of the liver using combined landmark-intensity information". In: *International journal of computer assisted radiology and surgery* 4.1, pp. 79–88.

Lekadir, Karim et al. (2014). "Statistical personalization of ventricular fiber orientation using shape predictors". In: *IEEE transactions on medical imaging* 33.4, pp. 882–890.

Leung, Kelvin K et al. (2010). "Automated cross-sectional and longitudinal hippocampal volume measurement in mild cognitive impairment and Alzheimer's disease". In: *Neuroimage* 51.4, pp. 1345–1359.

Leventon, Michael E, W Eric L Grimson, and Olivier Faugeras (2000). "Statistical shape influence in geodesic active contours". In: *Computer Vision and Pattern Recognition, 2000. Proceedings. IEEE Conference on*. Vol. 1. IEEE, pp. 316–323.

Liu, Yawu et al. (2011). "Diffusion tensor imaging and tract-based spatial statistics in Alzheimer's disease and mild cognitive impairment". In: *Neurobiology of aging* 32.9, pp. 1558–1571.

Lorenz, Cristian and Nils Krahnstöver (2000). "Generation of point-based 3D statistical shape models for anatomical objects". In: *Computer vision and image understanding* 77.2, pp. 175–191.

Lyttelton, Oliver et al. (2007). "An unbiased iterative group registration template for cortical surface analysis". In: *Neuroimage* 34.4, pp. 1535–1544.

Maddah, Mahnaz et al. (2008). "A unified framework for clustering and quantitative analysis of white matter fiber tracts". In: *Medical image analysis* 12.2, pp. 191–202.

Mazziotta, John et al. (2001). "A probabilistic atlas and reference system for the human brain: International Consortium for Brain Mapping (ICBM)". In: *Philosophical Transactions of the Royal Society of London B: Biological Sciences* 356.1412, pp. 1293–1322.

McCloskey, Eugene V et al. (2007). "Clodronate reduces the incidence of fractures in community-dwelling elderly women unselected for osteoporosis: results of a double-blind, placebo-controlled randomized study". In: *Journal of Bone and Mineral Research* 22.1, pp. 135–141.

McGraw, Tim et al. (2006). "Von Mises-Fisher mixture model of the diffusion ODF". In: *3rd IEEE International Symposium on Biomedical Imaging: Nano to Macro, 2006.* IEEE, pp. 65–68.

Medina, David et al. (2006). "White matter changes in mild cognitive impairment and AD: a diffusion tensor imaging study". In: *Neurobiology of aging* 27.5, pp. 663–672.

Miga, Michael I et al. (2003). "Cortical surface registration for image-guided neurosurgery using laser-range scanning". In: *IEEE Transactions on medical Imaging* 22.8, pp. 973–985.

Mittelstadt, Brent D (2002). *Method for determining the location and orientation of a bone for computer-assisted orthopedic procedures using intraoperatively attached markers*. US Patent 6,430,434.

Modat, Marc et al. (2010). "Fast free-form deformation using graphics processing units". In: *Computer methods and programs in biomedicine* 98.3, pp. 278–284.

Mori, Susumu et al. (2008). "Stereotaxic white matter atlas based on diffusion tensor imaging in an ICBM template". In: *Neuroimage* 40.2, pp. 570–582.

Morra, Jonathan H et al. (2009). "Automated mapping of hippocampal atrophy in 1-year repeat MRI data from 490 subjects with Alzheimer's disease, mild cognitive impairment, and elderly controls". In: *Neuroimage* 45.1, S3–S15.

Myronenko, Andriy and Xubo Song (2010). "Point set registration: Coherent point drift". In: *IEEE transactions on pattern analysis and machine intelligence* 32.12, pp. 2262–2275.

Nolte, John (2002). "The human brain: an introduction to its functional anatomy". In:

O'Donnell, Lauren J and Carl-Fredrik Westin (2007). "Automatic tractography segmentation using a high-dimensional white matter atlas". In: *IEEE transactions on medical imaging* 26.11, pp. 1562–1575.

Ourselin, Sébastien et al. (2001). "Reconstructing a 3D structure from serial histological sections". In: *Image and vision computing* 19.1, pp. 25–31.

Patenaude, Brian et al. (2011). "A Bayesian model of shape and appearance for subcortical brain segmentation". In: *Neuroimage* 56.3, pp. 907–922.

Peel, David and Geoffrey J McLachlan (2000). "Robust mixture modelling using the t distribution". In: *Statistics and computing* 10.4, pp. 339–348.

Pereañez, Marco et al. (2014). "A framework for the merging of pre-existing and correspondenceless 3D statistical shape models". In: *Medical image analysis* 18.7, pp. 1044–1058.

Pierpaoli, C et al. (2010). "TORTOISE: an integrated software package for processing of diffusion MRI data". In: *Book TORTOISE: an Integrated Software Package for Processing of Diffusion MRI Data (Editor edˆ eds)* 18, p. 1597.

Pierpaoli, Carlo and Peter J Basser (1996). "Toward a quantitative assessment of diffusion anisotropy". In: *Magnetic resonance in Medicine* 36.6, pp. 893–906.

Pizer, Stephen M et al. (2003). "Deformable m-reps for 3d medical image segmentation". In: *International Journal of Computer Vision* 55.2-3, pp. 85–106.

Prados Carrasco, F et al. (2016). "NiftyWeb: web based platform for image processing on the cloud". In: International Society for Magnetic Resonance in Medicine (ISMRM).

Raabe, Andreas et al. (2002). "Laser surface scanning for patient registration in intracranial image-guided surgery". In: *Neurosurgery* 50.4, pp. 797–803.

Rangarajan, Anand et al. (1997). "A robust point-matching algorithm for autoradiograph alignment". In: *Medical Image Analysis* 1.4, pp. 379–398.

Rasoulian, Abtin, Robert Rohling, and Purang Abolmaesumi (2012). "Group-wise registration of point sets for statistical shape models". In: *IEEE transactions on medical imaging* 31.11, pp. 2025–2034.

Rausch, Johannes et al. (2016). "Kinect-Based Correction of Overexposure Artifacts in Knee Imaging with C-Arm CT Systems". In: *Journal of Biomedical Imaging* 2016, p. 1.

Ravikumar, Nishant et al. (2015). "3D active shape models of human brain structures: application to patient-specific mesh generation". In: *SPIE Medical Imaging*. International Society for Optics and Photonics, pp. 94142D–94142D.

Ravikumar, Nishant et al. (2016a). "A multi-resolution t-mixture model approach to robust group-wise alignment of shapes". In: *International Conference on Medical Image Computing and Computer-Assisted Intervention*. Springer, pp. 142–149.

Ravikumar, Nishant et al. (2016b). "Robust group-wise rigid registration of point sets using t-mixture model". In: *SPIE Medical Imaging*. International Society for Optics and Photonics, 97840S–97840S.

— (2017). "Generalised coherent point drift for group-wise registration of multi-dimensional point sets". In: *International Conference on Medical Image Computing and Computer-Assisted Intervention*. Springer, In press.

Ravikumar, Nishant et al. (2017 Under review[a]). "Generalised coherent point drift for group-wise multi-dimensional analysis of diffusion brain MRI data". In: *Medical image analysis*.

Ravikumar, Nishant et al. (2017 Under review[b]). "Group-wise similarity registration of point sets using Student's t-mixture model for statistical shape models". In: *Medical image analysis*.

Rueckert, Daniel et al. (1999). "Nonrigid registration using free-form deformations: application to breast MR images". In: *IEEE transactions on medical imaging* 18.8, pp. 712–721.

Salat, DH et al. (2005). "Age-related alterations in white matter microstructure measured by diffusion tensor imaging". In: *Neurobiology of aging* 26.8, pp. 1215–1227.

Schwartzman, Armin, Robert F Dougherty, and Jonathan E Taylor (2005). "Cross-subject comparison of principal diffusion direction maps". In: *Magnetic Resonance in Medicine* 53.6, pp. 1423–1431.

Selle, Dirk et al. (2002). "Analysis of vasculature for liver surgical planning". In: *IEEE transactions on medical imaging* 21.11, pp. 1344–1357.

Serradell, Eduard et al. (2012). "Robust non-rigid registration of 2D and 3D graphs". In: *Computer Vision and Pattern Recognition (CVPR), 2012 IEEE Conference on*. IEEE, pp. 996–1003.

Shen, Kai-kai et al. (2012). "Detecting global and local hippocampal shape changes in Alzheimer's disease using statistical shape models". In: *Neuroimage* 59.3, pp. 2155–2166.

Smith, Stephen M et al. (2006). "Tract-based spatial statistics: voxelwise analysis of multi-subject diffusion data". In: *Neuroimage* 31.4, pp. 1487–1505.

Sra, Suvrit and Dmitrii Karp (2013). "The multivariate Watson distribution: Maximum-likelihood estimation and other aspects". In: *Journal of Multivariate Analysis* 114, pp. 256–269.

Staib, Lawrence H and James S Duncan (1996). "Model-based deformable surface finding for medical images". In: *IEEE transactions on medical imaging* 15.5, pp. 720–731.

Stricker, Nikki H et al. (2009). "Decreased white matter integrity in late-myelinating fiber pathways in Alzheimer's disease supports retrogenesis". In: *Neuroimage* 45.1, pp. 10–16.

Styner, Martin et al. (2003). "Automatic and robust computation of 3D medial models incorporating object variability". In: *International Journal of Computer Vision* 55.2-3, pp. 107–122.

Styner, Martin et al. (2004). "Boundary and medial shape analysis of the hippocampus in schizophrenia". In: *Medical image analysis* 8.3, pp. 197–203.

Svensén, Markus and Christopher M Bishop (2005). "Robust Bayesian mixture modelling". In: *Neurocomputing* 64, pp. 235–252.

Thompson, Paul M et al. (2001). "Cortical change in Alzheimer's disease detected with a disease-specific population-based brain atlas". In: *Cerebral Cortex* 11.1, pp. 1–16.

Twining, Carole J and Christopher J Taylor (2001). "Kernel principal component analysis and the construction of non-linear active shape models." In: *BMVC*. Vol. 1, pp. 23–32.

Vaillant, Marc and Joan Glaunès (2005). "Surface matching via currents". In: *Biennial International Conference on Information Processing in Medical Imaging*. Springer, pp. 381–392.

Wang, Fei, Baba C Vemuri, and Anand Rangarajan (2006). "Groupwise point pattern registration using a novel CDF-based Jensen-Shannon Divergence". In: *2006 IEEE Computer Society Conference on Computer Vision and Pattern Recognition (CVPR'06)*. Vol. 1. IEEE, pp. 1283–1288.

Wang, Yongmei, Bradley S Peterson, and Lawrence H Staib (2003). "3D brain surface matching based on geodesics and local geometry". In: *Computer Vision and Image Understanding* 89.2, pp. 252–271.

Zagorchev, Lyubomir et al. (2016). "Differences in regional brain volumes two months and one year after mild traumatic brain injury". In: *Journal of neurotrauma* 33.1, pp. 29–34.

Zhang, Y et al. (2007). "Diffusion tensor imaging of cingulum fibers in mild cognitive impairment and Alzheimer disease". In: *Neurology* 68.1, pp. 13–19.

Zhao, Hong-Kai, Stanley Osher, and Ronald Fedkiw (2001). "Fast surface reconstruction using the level set method". In: *Variational and Level Set Methods in Computer Vision, 2001. Proceedings. IEEE Workshop on*. IEEE, pp. 194–201.

Zheng, Yefeng and David Doermann (2006). "Robust point matching for nonrigid shapes by preserving local neighborhood structures". In: *IEEE transactions on pattern analysis and machine intelligence* 28.4, pp. 643–649.

Zhou, Luping et al. (2009). "Hippocampal shape analysis for Alzheimer's disease using an efficient hypothesis test and regularized discriminative deformation". In: *Hippocampus* 19.6, pp. 533–540.

Zhou, Zhiyong et al. (2014). "Robust non-rigid point set registration using student's-t mixture model". In: *PloS one* 9.3, e91381.

Zvitia, Orly et al. (2010). "Co-registration of white matter tractographies by adaptive-mean-shift and Gaussian mixture modeling". In: *IEEE transactions on medical imaging* 29.1, pp. 132–145.